

Analytical Load-Deflection Equations for Beam and 2-D Panel with a Bilinear Moment-
Curvature Model

by

Xinmeng Wang

A Thesis Presented in Partial Fulfillment
of the Requirements for the Degree
Master of Science

Approved July 2015 by the
Graduate Supervisory Committee:

Barzin Mobasher, Chair
Subramaniam Rajan
Narayanan Neithalath

ARIZONA STATE UNIVERSITY

August 2015

ABSTRACT

A simplified bilinear moment-curvature model are derived based on the moment-curvature response generated from a parameterized stress-strain response of strain softening and or strain-hardening material by Dr. Barzin Mobasher and Dr. Chote Soranakom. Closed form solutions are developed for deflection calculations of determinate beams subjected to usual loading patterns at any load stage. The solutions are based on a bilinear moment curvature response characterized by the flexural crack initiation and ultimate capacity based on a deflection hardening behavior. Closed form equations for deflection calculation are presented for simply supported beams under three point bending, four point bending, uniform load, concentrated moment at the middle, pure bending, and for cantilever beam under a point load at the end, a point load with an arbitrary distance from the fixed end, and uniform load. These expressions are derived for pre-cracked and post cracked regions. A parametric study is conducted to examine the effects of moment and curvature at the ultimate stage to moment and curvature at the first crack ratios on the deflection. The effectiveness of the simplified closed form solution is demonstrated by comparing the analytical load deflection response and the experimental results for three point and four point bending. The simplified bilinear moment-curvature model is modified by imposing the deflection softening behavior so that it can be widely implemented in the analysis of 2-D panels. The derivations of elastic solutions and yield line approach of 2-D panels are presented. Effectiveness of the proposed moment-curvature model with various types of panels is verified by comparing the simulated data with the experimental data of panel test.

ACKNOWLEDGEMENTS

I would like to specially thank my advisor Dr. Barzin Mobasher, who provides me the opportunity to work in the field of research that I could go through variety of excited topics and experimental programs. Let alone all the attention, invaluable intellectual insights he gave me. I also want to extend my appreciation to Dr. Subramaniam D. Rajan and Dr. Narayanan Neithalath who served as my committee members, helping and supervising my progress in Master's degree program.

I would also like to thank Vikram Dey and Yiming Yao, who actually taught me many skills including preparing and conducting experiment, data analysis and all of his supports and ideas throughout my research work. I would like to acknowledge outstanding work done by my peer Dr. Chote Soranakom and Karan Aswani, for establishing the basis and a straight forward path that I could follow up and extended my work to further areas.

I greatly appreciate the assistance provided by Mr. Peter Goguen and Mr. Kenny Witczak for all of their great works in the laboratory, especially the trouble-shooting and maintenance on testing devices. Without their help, I could definitely not finish my experiments.

Absolutely, I would express my gratitude to my dear colleagues and friend, Robert Kachala and Jacob Bauchmoyer for their help and more importantly, the great time we spent together.

TABLE OF CONTENTS

| | Page |
|---|------|
| LIST OF TABLES | vi |
| LIST OF FIGURES | viii |
| CHAPTER | |
| 1 - INTRODUCTION | 1 |
| 1.1 Cement Based Composites | 1 |
| 1.1.1 Fiber Reinforced Concrete | 1 |
| 1.1.2 Textile Reinforced Concrete | 3 |
| 1.2 Strain Hardening Fiber Reinforced Cement Composite | 4 |
| 1.3 Derivation of Moment-Curvature Relationship | 5 |
| 1.3.1 Simplified Strain-Hardening Fiber Reinforced Concrete Model | 5 |
| 1.3.2 Moment-Curvature Relationship | 6 |
| 1.4 Thesis Motivation and Objectives | 10 |
| 2 - DERIVATION OF CLOSED-FORM DEFLECTION EQUATIONS FOR BEAMS WITH SIMPLIFIED MOMENT-CURVATURE MODELS | 13 |
| 2.1 Bilinear Moment-Curvature Relationship | 14 |
| 2.2 Moment-Curvature Distributions | 16 |
| 2.3 Derivation of Load-Deflection Equations for a Beam in Flexure | 19 |
| 2.3.1 Case 1 – Load-Deflection with Simply Supported Beam | 22 |
| 2.3.2 Case 2 – Load-Deflection with Cantilever Beam | 39 |
| 2.4 Parametric Study and 2-D Contour | 49 |

| CHAPTER | Page |
|---|------|
| 2.4.1 Normalized Curvature Distribution | 49 |
| 2.4.2 Deflection Coefficient Distribution | 55 |
| 2.4.3 2-D Contour | 60 |
| 2.5 Experimental Verification | 64 |
| 2.5.1 Algorithm to Predict Load Deflection Response | 64 |
| 2.5.2 Data Set 1 | 65 |
| 2.5.3 Data Set 2 | 70 |
| 2.5.4 Data Set 3 | 74 |
| 2.5.5 Data Set 4 | 78 |
| 2.5.6 Data Set 5 | 85 |
| 3 - ELASTIC SOLUTIONS AND YIELD LINE THEORY FOR STRAIN HARDENING STRUCTURAL PANNELS..... | 94 |
| 3.1 Elastic Solution of Plates | 94 |
| 3.1.1 Governing Equation for Deflection of Plates..... | 94 |
| 3.1.2 Boundary Conditions | 95 |
| 3.2 Elastic Solutions of Various Types of Panels | 96 |
| 3.2.1 Case 1 – Round Panel | 96 |
| 3.2.2 Case 2 – Rectangular Panel..... | 99 |
| 3.2.3 Case 3- Square panel..... | 105 |
| 3.3 Yield Line Analysis Approach..... | 107 |
| 3.4 Moment-Load Relationship of Panels..... | 108 |

| CHAPTER | Page |
|--|------|
| 3.4.1 Case Study 1 – Applied Load vs. Yield Line Moment Relationship for Round Panels | 108 |
| 3.4.2 Case Study 2 – Applied Load vs. Yield Line Moment Relationship for Rectangular Panels..... | 110 |
| 3.4.3 Case Study 3 – Applied Load vs. Yield Line Moment Relationship for Square Panels | 112 |
| 3.5 Curvature-Deflection Relationship of Panels | 116 |
| 3.5.1 Case Study 1 – Curvature – Deflection Relationship for a Round Panel..... | 117 |
| 3.5.2 Case Study 2 – Curvature – Deflection Relationship for a Rectangular Panel..... | 119 |
| 3.5.3 Case Study 2 – Curvature – Deflection Relationship for a Rectangular Panel..... | 123 |
| 3.6 Bilinear Moment-Curvature Relationship for Panel | 126 |
| 3.7 Experimental Verification..... | 128 |
| 3.7.1 Algorithm to Predict Load-Deflection Response..... | 128 |
| 3.7.2 Data Set 1 | 129 |
| 3.7.3 Data Set 2..... | 132 |
| 3.7.4 Data Set 3..... | 135 |
| 3.7.5 Data Set 4..... | 138 |
| 4. REFERENCES..... | 142 |

LIST OF TABLES

| Table | Page |
|---|------|
| 1.3.1 - Neutral Axis k , Normalized Moment and Normalized Curvature for Each Stage of Normalized Tensile Strain at Bottom Fiber | 10 |
| 2.3.1 - Curvature and Deflection of Elastic Region for Simply Supported Beam..... | 35 |
| 2.3.2 - Curvature and Deflection of Post- cracked Region 1 for Simply Supported Beam | 36 |
| 2.3.3 - Curvature and Deflection of Post- cracked Region 2 for Simply Supported Beam | 37 |
| 2.3.4 - Notations of the Deflection Equations for Simply Supported Beam..... | 38 |
| 2.3.5 - Curvature and Deflection of Elastic Region for Cantilever Beam | 47 |
| 2.3.6 - Curvature and Deflection of Post- cracked Region 1 for Cantilever Beam | 47 |
| 2.3.7 - Curvature and Deflection of Post- cracked Region 2 for Cantilever Beam | 48 |
| 2.3.8 - Notations of the Deflection Equations for Cantilever Beam..... | 48 |
| 2.4.1 - Normalized Curvature Equations with Constant m' for 3PB Beam..... | 50 |
| 2.4.2 - Normalized Curvature Equations with Constant q' for 3PB Beam..... | 50 |
| 2.4.3 - Deflection Coefficient Equations with Constant m' for 3PB Beam..... | 56 |
| 2.4.4 - Deflection Coefficient Equations with Constant q' for 3PB Beam..... | 56 |
| 2.4.5- Parameters of 2-D Deflection Distribution..... | 61 |
| 2.5.1 - Properties of Yarns Made up the Fabrics for Data Set 1 | 66 |
| 2.5.2- Volume Fraction (V_f) of Reinforcement for Data Set 1..... | 66 |
| 2.5.3 (a) - Simulated Parameters of 100A..... | 66 |
| 2.5.3(b) - Simulated Parameters of 100P | 67 |

| Table | Page |
|---|------|
| 2.5.3(c) - Simulated Parameters of 25A75P | 67 |
| 2.5.4 - Geometry Characteristics of Specimens..... | 71 |
| 2.5.5 - Steel Fiber Reinforced Concrete Parameters for Current Model | 71 |
| 2.5.6 – Details of Test Beam for Data Set 3 | 75 |
| 2.5.7 - Simulated Parameters of Current Model for Data Set 3..... | 75 |
| 2.5.8 - Details of Reinforced Beam | 79 |
| 2.5.9 - Simulated Parameters of Current Model for Data Set 4..... | 80 |
| 2.5.10 - Parameters with Previous Model for Data Set 4..... | 83 |
| 2.5.11 - Details of Beam for Data Set 5..... | 86 |
| 2.5.12 - Simulated Parameters of Current Model for Data Set 5 | 87 |
| 2.5.13 - Parameters with Previous Model for Data Set 5..... | 90 |
| 3.2.1 - Numerical Factor for Maximum Deflection for Case 2.1 | 104 |
| 3.2.2 – Elastic Maximum Deflection Equations for Case 1 to Case 3..... | 106 |
| 3.5- Empirically Derived Hinge Lengths..... | 116 |
| 3.5.1 Summary of Relationship between Curvature and Deflection for Panels | 126 |
| 3.7.1 - Simulated Parameters of Current Model for Data Set 1 | 129 |
| 3.7.2- Details of Round Panel Specimens for Data Set 2 | 133 |
| 3.7.3- Simulated Parameters of Current Model for Data Set 3..... | 133 |
| 3.7.4- Shape Properties of Steel Fibers for Data Set 3..... | 136 |
| 3.7.5- Details of Round Panel Specimens for Data Set 3 | 136 |
| 3.7.7- Details of Round Panel Specimens for Data Set 4 | 139 |
| 3.7.8- Simulated Parameters of Current Model for Data Set 4..... | 139 |

LIST OF FIGURES

| Figure | Page |
|--|------|
| 2.1.1 - Bilinear Moment-Curvature Relationship | 15 |
| 2.1.2 - Normalized Moment-Curvature Relationship Represented as (q' , m')..... | 16 |
| 2.2.1 - Three-Point Bending ;(a) Moment and Curvature Distributions along the Beam;(b) Calculation of ξ ; | 18 |
| 2.3.1 - Flowchart for the Derivation of Load-Deflection Equation | 19 |
| 2.3.2 - Flexural Stiffness Regions for General Loading for Simply Supported Beam | 20 |
| 2.3.1.1 - Three-Point Bending; (a) Moment and Curvature Distributions along the Beam;(b) Calculation of ξ ; | 24 |
| 2.3.1.2 - Four-Point Bending; (a) Moment and Curvature Distributions along the Beam;(b) Calculation of ξ ; | 28 |
| 2.3.1.2 - Four-Point Bending (with arbitrary distance a) ;(a) Moment and Curvature Distributions along the Beam;(b) Calculation of ξ ; | 32 |
| 2.3.2.1 - Cantilever Beam Subjected with Point Load at Free End;(a) Moment and Curvature Distributions along the Beam;(b) Calculation of ξ ; | 41 |
| 2.3.2.2 - Cantilever Beam Subjected with Uniform Loading ;(a) Moment and Curvature Distributions along the Beam;(b) Calculation of ξ ; | 45 |
| 2.4.1 - Effects of m' and q' on Normalized Curvature Distribution for Simply Supported Beam; (a) 3PB; (b) 4PB; (c) Uniform Loading; (d) Moment at the Middle..... | 53 |
| 2.4.2 - Effects of m' and q' on Normalized Curvature Distribution for Cantilever Beam; (a) Uniform Loading; (b) Concentrated Load at Free End; (c) Concentrated Load with Distance S from Fixed End..... | 55 |

| Figure | Page |
|--|------|
| 2.4.3 - Effects of m' and q' on Deflection Distribution for Simply Supported Beam; (a) 3PB; (b) 4PB; (c) Uniform Loading; (d) Moment at the Middle..... | 58 |
| 2.4.4 - Effects of m' and q' on Deflection Distribution for Cantilever Beam; (a) Uniform Loading; (b) Concentrated Load at Free End; (c) Concentrated Load with Distance S from Fixed End..... | 60 |
| 2.4.5 - 2-D Deflection Distribution of Three-Point Bending..... | 62 |
| 2.4.6 - 2-D Deflection Distribution of Four-Point Bending..... | 62 |
| 2.4.7 - Deflection Distributions of Three- Point Bending; (a) Different Locations along the Beam; (b) Different Loading Levels. | 63 |
| 2.4.8 - Deflection Distributions of Four- Point Bending; (a) Different Locations along the Beam; (b) Different Loading Levels..... | 63 |
| 2.5.1 - Flow Chart of Prediction of Load-Deflection Response | 65 |
| 2.5.2 - Normalized Moment-Curvature Relationships; (a) 100A; (b) 100P; (c) 25A75P. | 69 |
| 2.5.3 - Load-Deflection Responses ; (a) 100A; (b) 100P; (c) 25A75P..... | 70 |
| 2.5.4 - Normalized Moment-Curvature Diagrams of Simulated Data; (a) H500; (b) H1000; (c) H1500 | 72 |
| 2.5.5 - Load Deflection Responses of FRC Beams at Two Levels of Fiber Contents (50 kg/m ³ and 75 kg/m ³)..... | 74 |
| 2.5.6 - Normalized Moment-Curvature Relationships;(a) B1,B2; (b) B3, B6; (c) B4, B8; (d)B5, B7..... | 77 |
| 2.6.7 - Load-Deflection Responses ;(a) B1,B2; (b) B3, B6; (c) B4, B8; (d)B5, B7 | 78 |
| 2.5.8 - Set up of four-point bending test (Unit: mm)..... | 78 |

| Figure | Page |
|--|------|
| 2.5.9 - (a) Load-Deflection Response of Beams V1, V2; (b) Simulated Normalized Moment-Curvature Relationship of Beams V1, V2 | 81 |
| 2.5.10 - (a) Load-Deflection Response of Beams V2, V3, V4, V6; (b) Simulated Normalized Moment-Curvature Relationship of Beams V2, V3, V4, V6 | 82 |
| 2.5.11 - (a) Load-deflection response of beams V2, V7, V8, V9; (b) Simulated Normalized Moment-Curvature Relationship of Beams V2, V7, V8, V9 | 82 |
| 2.5.12 - Comparison of Current Model with Previous Model for Beam V1 | 84 |
| 2.5.13 - Comparison of Current Model with Previous Model for Beam V3 | 84 |
| 2.5.14 - Comparison of Current Model with Previous Model for Beam V7 | 85 |
| 2.5.15 - Comparison of Current Model with Previous Model for Beam V9 | 85 |
| 2.5.16 - Normalized Moment-Curvature Relationship of HRC Beams; (a) B7, B8; (b) B9, B10; (c) B11, B12 | 88 |
| 2.5.17 - Load-Deflection Response of HRC Beams at Three Levels of Fiber Contents; (a) 25 kg/m ³ ; (b) 50 kg/ m ³ ; (60) kg/ m ³ | 89 |
| 2.5.19 - Comparison of Current Model with Previous Model; (a) B11; (b) B12 | 93 |
| 3.2.1 - Round Panel Subjected with Concentrated Load at Center and Simply Supported Edge..... | 97 |
| 3.2.2 - Clamped Edge Round Panel Subjected with Concentrated Load at center | 99 |
| 3.2.3 - Simply Supported Rectangular Panel Subjected with Uniform Load | 102 |
| 3.4.1 - Principle of Virtual Work of a Round Panel with Simply Supported in its Contour and Subjected to Center Point Load | 109 |
| 3.4.2 - Simply Supported Rectangular Slab..... | 111 |

| Figure | Page |
|--|------|
| 3.4.3 - Simply Supported Square Panel | 114 |
| 3.5.1 – Curvature-Deflection Relationship for Round Panel | 117 |
| 3.5.2 - Curvature-Deflection Relationship for Rectangular Panel | 119 |
| 3.5.3 - Planes KON and PLM | 120 |
| 3.5.4 - Planes KON and NOPM..... | 121 |
| 3.5.5 - Rectangular Slab Fixed from 3 Sides and Free from Fourth..... | 123 |
| 3.5.6 - Curvature-Deflection Relationship for Square Panel | 123 |
| 3.5.7 Planes AED and EBC | 124 |
| 3.6.1 - Bilinear Moment-Curvature Relationship for Panels | 127 |
| 3.6.2 - Normalized Moment-Curvature Curve Represented as (q' , m') | 128 |
| 3.7.1- Normalized Moment-Curvature Relationship | 130 |
| 3.7.2 - Load-Deflection Responses of the Round Panel Samples..... | 131 |
| 3.7.3 - Effect of Hinge Length on Simulated Results..... | 132 |
| 3.7.3 - Normalized Moment –Curvature Relationships of Round Panels; (a) SFRC;(b) Synthetic FRC | 134 |
| 3.7.4 - Load-Deflection Responses of Round Panels; (a) SFRC;(b) Synthetic FRC..... | 135 |
| 3.7.5 - Normalized Moment –Curvature Relationships of Square Panels; (a) Steel Fiber with Length of 25 mm;(b) Steel Fiber with Length of 35 mm..... | 137 |
| 3.7.6 - Load-Deflection Responses of Square Panels; (a) Steel Fiber with Length of 25 mm;(b) Steel Fiber with Length of 35 mm..... | 138 |

| Figure | Page |
|---|------|
| 3.7.7 - Normalized Moment –Curvature Relationships of Round Panels; (a) RC80/60 with Two Levels of Fiber Content; (b) RC65/35 with Two Levels of Fiber Content..... | 139 |
| 3.7.8 - Load-Deflection Response of Round Panels; (a) RC80/60 with Two Levels of Fiber Content;(b) RC65/35, $V_f=1.0\%$; (c) RC65/35, $V_f=1.25\%$ | 140 |

1. - INTRODUCTION

1.1 Cement Based Composites

Concrete is used extremely widely in building and civil engineering structures, due to its low cost, flexibility, durability, and high strength. However, Concrete being one of the most consumed building materials and the disadvantage of concrete is the weakness in tension; a lot of research is going on developing building systems with low cement and utilizing renewable energy resources. Cement based composites aid in improving tensile strength and stiffness along with introduction of ductility in the infrastructure systems and is consist of fiber reinforced composites in form of fabric meshes and a cementitious bonding agent, recently, emerged as a very effective strengthening solution for existing reinforced concrete structures [1]. Different solutions to design cement based strengthening systems for concrete structures are proposed; among these the Fiber Reinforced Concrete (FRC) and Textile Reinforced Concrete (TRC) became the research topics of interest. The effectiveness of cement based composite systems as flexural strengthening materials of reinforced concrete structures has been demonstrated by results of some experimental investigations [2 ,3 ,4].

1.1.1 Fiber Reinforced Concrete

Fiber reinforced concrete (FRC) is plain concrete containing fibrous material which increases its structural integrity. It contains short discrete fibers that are uniformly distributed and randomly oriented. Fibers include steel fibers, glass fibers, synthetic fibers and natural fibers. Fiber reinforced concrete is widely applied on the current infrastructure system and has been successfully used in slabs-on-grade, shotcrete, architectural concrete, precast products, offshore structures, structures in seismic regions,

thin and thick repairs, crash barriers, footings, hydraulic structures, and many other applications[5]. Figure 1.1.1 shows the various types of fiber and Figure 1.1.2 shows the applications of fiber reinforced concrete. Polypropylene fiber used in concrete enhances the shrinkage cracking resistance and toughness of plain concrete [6]. The compressive strength of high strength concrete improved with additions of steel fibers at various volume fractions [7]. The addition of 0.75% fiber content in the flexural members without shear stirrups is sufficient to achieve the ultimate resistance that is the same as the conventional RC flexural member with stirrups [8].



Figure 1.1.1 - Various Types of Fiber for Reinforced Concrete

In addition to the fiber reinforced concrete, fiber reinforced polymer (FRP) has also been identified as an attractive candidate material for civil infrastructure applications because of its high strength, light weight, and its non-corrosive and nonmagnetic characteristics [9]. One of the types of fiber reinforced polymer composite is FRP bars and they are intended for use as concrete reinforcing in areas where steel reinforcing has a limited life span due to the effect of corrosion. The FRP bars can be made from various types of fibers such as Glass (GFRP), Carbon (CFRP) and Aramid (AFRP).

(a)



(b)

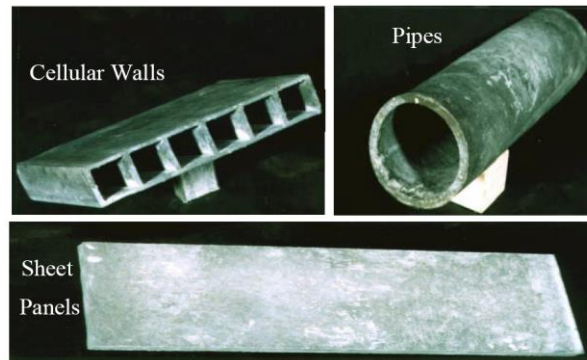


Figure 1.1.2 - Applications of Fiber Reinforced Concrete; (a) GFRC Project at Trillium Building Woodland Hills, California; (b) Structural Components.

1.1.2 Textile Reinforced Concrete

Textile-reinforced concrete (TRC) is a composite material consisting of a matrix with a maximum aggregate grain size between 1 and 2 mm and high-performance, continuous multifilament-yarns made of alkali-resistant (AR) glass, carbon, or polymer[10]. Textile reinforced concrete (TRC) has been in service in engineering applications for many years in low-profile, relatively low-cost applications. TRC can be utilized to build slender, lightweight, modular and freeform structures and eliminate the risk of corrosion. The major advantages of TRC are its high tensile strength and pseudo-ductile behavior, the latter characterized by large deformations due to its tolerance of multiple cracking. TRC affords a priori better temperature stability and it can be used with the shotcrete technique. Composite TRC has the potential to reduce the carbon dependence and thus minimize the ecological footprint in accordance with the concepts of sustainable development [11].

The bending and shear behavior of TRC were evaluated by various tests to indicate that both load carrying capacity and the shear loading capacity, can be increased with an additional textile reinforced layer. And the serviceability also will be improved [12]. For Textile Reinforced Concrete applications, bi- or multi-axial 2D and 3D textile meshes can be used as reinforcement. For a simple bi-axial case, the mesh comprises two groups of textile fiber yarns (threads), warp (0°) and weft (90°), interwoven perpendicularly to each other. Yarns are composed of multiple single fibers of continuous length, also designed as filaments.

1.2 Strain Hardening Fiber Reinforced Cement Composite

The tensile response of fiber reinforced cement composites can be generally classified in two distinct categories depending on their behavior after first cracking, namely, either strain-hardening or strain-softening. The strain-softening category can distinguish as deflection-hardening or deflection-softening [13]. As the strain-hardening FRC composites it is generally accepted that their use can significantly improve the seismic resistance of concrete structures subjected to reversed cyclic loading as well as their impact resistance. The design and implementation of these systems requires one to acknowledge and use the strain-hardening response that is attributed to multiple cracking. Propagation of initial crack in strain hardening composites is resisted by bridging mechanism. Since a substantial amount of energy is required to further extend existing cracks, secondary cracks form. Single crack localization is therefore shifted to multiple distributed cracking mechanisms, leading to macroscopic pseudo-strain hardening behaviors. The dominant toughening mechanisms in these systems are attributed to

matrix cracking, ply delamination, and crack deflection mechanisms as studied by means of fluorescent microscopy and scanning electron microscopy.

1.3 Derivation of Moment-Curvature Relationship

1.3.1 Simplified Strain-hardening Fiber Reinforced Concrete Model

A general strain hardening tensile, and an elastic perfectly plastic compression model as derived by Soranakom and Mobasher [14] [15] [16] and shown in Figure 1.3.1 Tensile response is defined by tensile stiffness, E , first crack tensile strain, ε_{cr} , Cracking tensile strength, $\sigma_{cr} = E\varepsilon_{cr}$, ultimate tensile capacity, ε_{peak} , and post crack modulus, E_{cr} . The softening range is shown as a constant stress level, $\mu E\varepsilon_{cr}$. The compression response is defined by the compressive strength, σ_{cy} defined as $\omega\gamma E\varepsilon_{cr}$. The moment-curvature relationship is generated based on the tension and compression models discussed later here. Material parameters required for the strain softening and hardening (SSCC and SHCC) are summarized as follows.

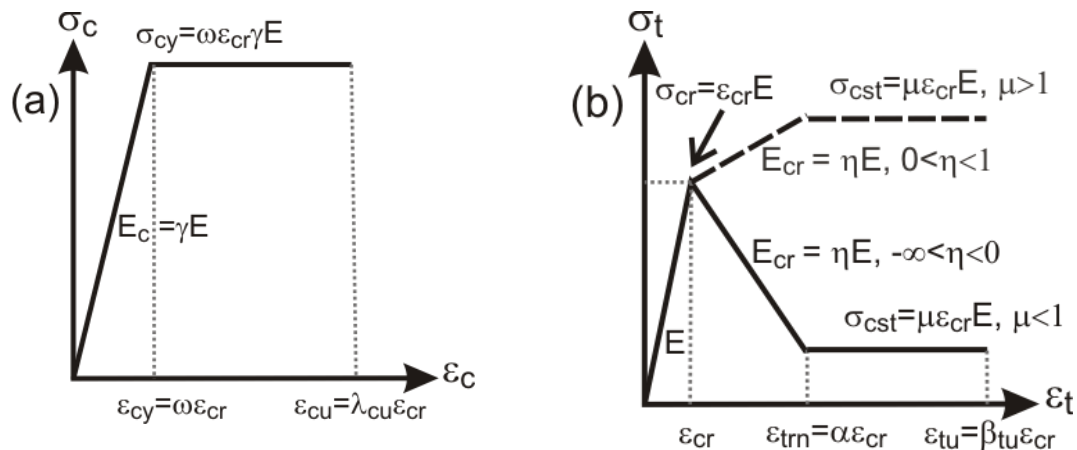


Figure 1.3.1 - Material Models for SHCC and SSCC FRC: (a) Compression; (b) Tension

Parameters, α , μ , η , ω are defined respectively as normalized tensile strain at peak strength, post-crack modulus, and compressive yield strain. Material parameters required for the simplified models are summarized as follows:

$$\text{Cracking tensile strain, } \varepsilon_{cr} = \frac{\sigma_{cr}}{E} \quad (1.3.1)$$

$$\text{Normalized tensile strain at peak strength, } \alpha = \frac{\varepsilon_{peak}}{\varepsilon_{cr}} ; \quad (1.3.2)$$

$$\text{Normalized post-crack modulus, } \eta = \frac{E_{cr}}{E} \quad (1.3.3)$$

$$\text{Normalized yield compressive strain, } \omega = \frac{\sigma_{cy}}{E\varepsilon_{cr}} = \frac{\sigma_{cy}}{\sigma_{cr}} \quad (1.3.4)$$

The only variable defined in terms of the applied tensile strain at the extreme fiber, β , which can be correlated to the extreme compressive strains at extreme fiber, λ , are defined as:

$$\text{Normalized tensile strain at bottom fiber, } \beta = \frac{\varepsilon_t}{\varepsilon_{cr}} \quad (1.3.5)$$

$$\text{Normalized compressive strain at top fiber, } \lambda = \frac{\varepsilon_c}{\varepsilon_{cr}} \quad (1.3.6)$$

The ratio of compressive and tensile modulus, parameter γ , has negligible effect on the ultimate moment capacity [17]. In typical SHCC, the compressive strength is several times higher than tensile strength; hence the flexural capacity is controlled by the tensile component.

1.3.2 Moment-Curvature Relationship

Moment capacity of a beam section according to the imposed tensile strain at the bottom fiber ($\varepsilon_t = \beta\varepsilon_{cr}$) can be derived based on the assumed linear strain distribution as shown in

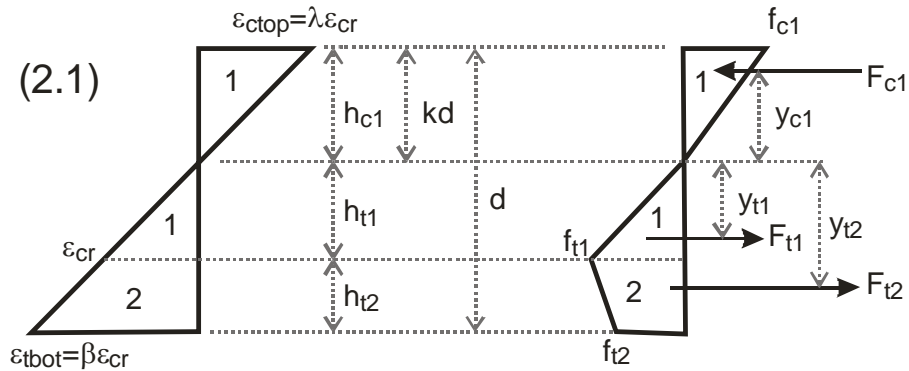
Fig. 1.3.4 (a). Figure 1.4 shows the strain and stress distribution of cross-section in stage 2.1. The corresponding strain and stress distributions of other stage also can be generated by flowing the tension and compression models. By using material models described in Figure 1.3.3 (a) and (b), the corresponding stress diagram is obtained as shown in Figure 1.3.4 (b) in which the stress distribution is subdivided into a compression zone 1, tension zone 1 and 2. Force components and their centroidal distance to the neutral axis in each zone can be expressed as:

$$\frac{F_{c1}}{bh\sigma_{cr}} = \frac{\beta\gamma k^2}{2(1-k)}; \quad \frac{y_{c1}}{h} = \frac{2}{3}k \quad (1.3.7)$$

$$\frac{F_{t1}}{bh\sigma_{cr}} = \frac{(1-k)}{2\beta}; \quad \frac{y_{t1}}{h} = \frac{2(1-k)}{3\beta} \quad (1.3.8)$$

$$\frac{F_{t2}}{bh\sigma_{cr}} = \frac{(1-k)(\beta-1)(\eta\beta-\eta+2)}{2\beta}; \quad \frac{y_{t2}}{h} = \frac{2\eta\beta^2-\eta\beta-\eta+3\beta+3}{3\beta(\eta\beta-\eta+2)}(1-k) \quad (1.3.9)$$

where F and y are the force and its centroid, respectively; subscripts $c1, t1, t2$ designate compression zone 1, tension zone 1 and 2, respectively; b and h are the width and the height of the beam, respectively. The neutral axis parameter k is found by solving the equilibrium of net internal forces equal to zero, $F_{c1} + F_{t1} + F_{t2} = 0$.



(a)

(b)

Figure 1.3.4 - Strain and Stress Diagrams at the Post Crack Stage (Ranges 2.1) (a) Strain Distribution; (b) Stress Distribution

The neutral axis parameter k is found by solving the equilibrium of net internal forces and the nominal moment capacity M_n is obtained by taking the first moment of force about the neutral axis. This procedure can also be done for every combination of tension and compression (three tensile modes and two compression modes). In case 2.1 which represents cracking tension and elastic compression response the parameters for neutral axis and bending moment are expressed as:

$$k = \frac{C_1 - \sqrt{\beta^2 C_1}}{C_1 - \beta^2}; \text{ where } C_1 = \eta(\beta^2 - 2\beta + 1) + 2\beta - 1 \quad (1.3.10)$$

The nominal moment capacity M_n is obtained by taking the first moment of force about the neutral axis, $M_n = F_{c1}y_{c1} + F_{t1}y_{t1} + F_{t2}y_{t2}$, and it is expressed as a product of the normalized nominal moment m_n and the cracking moment M_{cr} as follows:

$$M_n = m_n M_{cr} \quad , \quad M_{cr} = \frac{\sigma_{cr} b h^2}{6} \quad (1.3.11)$$

$$m_n = C_2 \frac{k^2 - 2k + 1}{\beta^2} + \frac{2\beta k^3}{1 - k}; \text{ where } C_2 = C_1 + 2C_1\beta - \beta^2 \quad (1.3.12)$$

According to bilinear tension and elastic compression models shown in Figure 1.3.1 (a) and (b), the maximum moment capacity is obtained when the normalized tensile strain at the bottom fiber ($\beta = \varepsilon_t / \varepsilon_{cr}$) reaches the tensile strain at peak strength ($\alpha = \varepsilon_{peak} / \varepsilon_{cr}$). However, the simplified equations (1.3.7) to (1.3.12) for moment capacity are applicable for the compressive stress in elastic region only. The elastic condition must be checked

by computing the normalized compressive strain developed at the top fiber λ and compare it to the normalized yield compressive strain ω . The general solutions for all the cases are presented in Table 1.2. Using the strain diagram in Figure 1.3.4 (a), the relationship between the top compressive strain and bottom tensile strain as follow:

$$\frac{\varepsilon_c}{kh} = \frac{\varepsilon_t}{(1-k)h} \quad (1.3.13)$$

By substituting $\varepsilon_c = \lambda\varepsilon_{cr}$ and $\varepsilon_t = \beta\varepsilon_{cr}$ in equation (1.3.13), then defining the maximum compressive strain to the yield compressive strain $\varepsilon_{cy} = \omega\varepsilon_{cr}$, equation (1.3.13) is expressed in normalized form:

$$\lambda = \frac{k}{1-k}\beta \leq \omega \quad (1.3.14)$$

The case represented by case 2.1 of the Table 1.3.1, where the tensile behavior is in elastic-plastic while the compressive behavior is still elastic is studied in this section. Equations for other cases can also be developed. The general solution presented in Table 1.3.1 can be simplified as follows. The location of neutral axis represented as a function of applied tensile strain β is represented as:

$$k = \frac{\sqrt{A}}{\sqrt{A} + \beta\sqrt{\gamma}} \quad A = \eta(\beta^2 + 1 - 2\beta) + 2\beta - 1 \quad (1.3.15)$$

This equation can be easily simplified by assuming equal tension and compression stiffness ($\gamma=1$). For an elastic perfectly plastic tension material ($\eta=0$) equation (1.3.15) reduces to:

$$k = \frac{\sqrt{2\beta-1}}{\sqrt{2\beta-1} + \beta} \quad (1.3.16)$$

Table 1.3.1 - Neutral Axis k , Normalized Moment and Normalized Curvature for Each Stage of Normalized Tensile Strain at Bottom Fiber

| Stage | k | $m = M/M_{cr}$ | $\phi = \Phi / \Phi_{cr}$ |
|---|--|--|--|
| 1 $0 < \beta \leq 1$ | $k_1 = \begin{cases} \frac{1}{2} & \text{for } \gamma=1 \\ \frac{-1+\sqrt{\gamma}}{-1+\gamma} & \text{for } \gamma \neq 1 \end{cases}$ | $m_1 = \frac{2\beta \left[(\gamma-1)k_1^3 + 3k_1^2 - 3k_1 + 1 \right]}{1-k_1}$ | $\phi_1 = \frac{\beta}{2(1-k_1)}$ |
| 2.1 $1 < \beta \leq \alpha$ $0 < \lambda \leq \omega$ | $k_{21} = \frac{D_{21} - \sqrt{D_{21}\gamma\beta^2}}{D_{21} - \gamma\beta^2}$ $D_{21} = \eta(\beta^2 - 2\beta + 1) + 2\beta$ | $M'_{21} = \frac{(2\gamma\beta^3 - C_{21})k_{21}^3 + 3C_{21}k_{21}^2 - 3C_{21}k_{21} + C_{21}}{1-k_{21}}$ $C_{21} = \frac{(2\beta^3 - 3\beta^2 + 1)\eta + 3\beta^2 - 1}{\beta^2}$ | $\phi'_{21} = \frac{\beta}{2(1-k_{21})}$ |
| 2.2 $1 < \beta \leq \alpha$ $\omega < \lambda \leq \lambda_{cu}$ | $k_{22} = \frac{D_{22}}{D_{22} + 2\omega\gamma\beta}$ $D_{22} = D_{21} + \gamma\omega^2$ | $M'_{22} = (3\gamma\omega\beta^2 + C_{22})k_{22}^2 - 2C_{22}k_{22} + C_{22}$ $C_{22} = C_{21} - \frac{\gamma\omega^3}{\beta^2}$ | $\phi'_{22} = \frac{\beta}{2(1-k_{22})}$ |
| 3.1 $\alpha < \beta \leq \beta_{tu}$ $0 < \lambda \leq \omega$ | $k_{31} = \frac{D_{31} - \sqrt{D_{31}\gamma\beta^2}}{D_{31} - \gamma\beta^2}$ $D_{31} = \eta(\alpha^2 - 2\alpha + 1) + 2\mu(\beta - \alpha) + 2\alpha - (2\alpha^3 - 3\alpha^2 + 1)\eta - 3\mu(\alpha^2 - \beta^2) + 3\alpha^2 - 1$ | $M'_{31} = \frac{(2\gamma\beta^3 - C_{31})k_{31}^3 + 3C_{31}k_{31}^2 - 3C_{31}k_{31} + C_{31}}{1-k_{31}}$ $C_{31} = \frac{(2\alpha^3 - 3\alpha^2 + 1)\eta - 3\mu(\alpha^2 - \beta^2) + 3\alpha^2 - 1}{\beta^2}$ | $\phi'_{31} = \frac{\beta}{2(1-k_{31})}$ |
| 3.2 $\alpha < \beta \leq \beta_{tu}$ $\omega < \lambda \leq \lambda_{cu}$ | $k_{32} = \frac{D_{32}}{D_{32} + 2\omega\gamma\beta}$ $D_{32} = D_{31} + \gamma\omega^2$ | $M'_{32} = (3\gamma\omega\beta^2 + C_{32})k_{32}^2 - 2C_{32}k_{32} + C_{32}$ $C_{32} = C_{31} - \frac{\gamma\omega^3}{\beta^2}$ | $\phi'_{32} = \frac{\beta}{2(1-k_{32})}$ |

Once the neutral axis parameter k is solved, the normalized force component can be obtain. The nominal moment capacity M_n is obtained by taking the first moment of force about the neutral axis.

1.4 Thesis Motivation and Objectives

The motivation of this research is to improve the design procedure of reinforced concrete, especially to complete or optimize the design and analysis of fiber reinforced concrete

structure. In this study, the closed-form deflection equations of beam subjected with bending are presented and the accuracy of these analytical solutions of flexural behavior is verified by comparing with the experimental data. Moment-curvature relationship is the start point in this research and based on the moment-curvature which derived from tension and compression models which is discussed in Section 1.3, a simplified bilinear moment-curvature model are presented and discussed in next Chapter. Using the algorithm of this study, one can use the model prediction tools as a design tool and customize the material properties of the composite for any structural application.

Lots of researcher studied the moment-curvature relationship and predictions of load-deflection responses for cement-based composites. Barros, Joaquim AO, et al [18] presented a close-form solution for the prediction of the moment-curvature relationship of cross sections of fiber reinforced concrete (FRC) elements failing in bending and reinforced longitudinally with steel and fiber reinforced polymer (FRP) bars based on the strain compatibility analysis. A numerical method is applied to predict the load-middle span deflection response. However, this procedure of predicting moment-curvature is impractical for general users and only the mid-span deflection can be simulated in this study. The numerical method of simulating the load-deflection may not be easier applied than the analytical solution. Kwak et al [19] presented the moment-curvature relationships which is acceptable for RC sections and the finite element method is implemented in the prediction of load-deflection response of simply supported beam. The empirical expression of plastic hinge length is included in the analysis. Lim, T. Y , et al [20] developed an analytical method for the moment-curvature characteristics of steel-fiber concrete (SFC) beams based on the tensile and compressive stress-strain behavior of

the composite. Deflection equations of mid-span of three- and four-point bending beam are derived.

However, prediction of the load-deflection responses in this study is acceptable not only for RC but also for FRC and hybrid reinforced concrete beam. In addition, instead of finite element method and numerical approach, the closed-form deflection equations of simply supported beam and cantilever beam with various loading patterns are presented in this study. Thus, our equations are more acceptable and powerful for general users.

2. - DERIVATION OF CLOSED-FORM DEFLECTION EQUATIONS FOR BEAMS WITH SIMPLIFIED MOMENT-CURVATURE MODELS

Soranakom and Mobasher [21] developed a procedure to use a parameterized bilinear or trilinear stress-strain response of a strain-softening and or strain-hardening material and derived closed form solutions for moment and curvature response of an arbitrary cross section. Once the moment-curvature response is obtained, it can be used in the context of slope-deflection equations to obtain the closed form solutions for load vs. rotation and load vs. deflection response of a beam subjected to a specified loading and boundary conditions [22]. Due to the nature of tension or compression dominated modes of failure, various cases must be considered, therefore closed form solutions to load-deflection equations is not obtainable directly due to mode interaction.

An approach to simplify and parametrically represent the moment-curvature response as a bilinear or trilinear function is presented. In this manner, moment-curvature response can be used to obtain a strain softening, or deflection hardening load-deflection response from the parametrized moment model. A set of closed form solutions to calculate deflection profile as well as mid-span deflection of a beam under three- and four- point bending was presented using moment-area method previously. In this study, a bilinear moment-curvature model was developed which can be applied to reinforced concrete, fiber reinforced concrete and general composite materials that exhibit some level of damage such that the moment curvature response is represented by means of a non-linear

response. The procedures to calculate the closed form equations for the deflection calculation at any point along a beam throughout the entire load range are developed.

2.1 Bilinear Moment-Curvature Relationship

A simplified parametric moment curvature response is represented by a bilinear function in elastic pre-cracked and post-cracked stages as shown in Figure 2.1.1 and the normalized moment-curvature relationship is shown in Figure 2.1.2. The elastic stage extends to the onset of first flexural crack. The second stage follows until the ultimate flexural capacity which corresponds to the ultimate state. This level can be specified as the curvature associated with the maximum tensile or compressive strain based on a specified flexural failure or ultimate mode defined for the structure. The bilinear elastic post-cracking moment-curvature response is fully defined by two control points (M_{cr}, φ_{cr}) and (M_u, φ_u) and expressed as:

$$M(\varphi) = EI_g \varphi \quad 0 < M \leq M_{cr} \quad 0 < \varphi \leq \varphi_{cr} \quad (2.1.1)$$

$$M(\varphi) = \frac{M_u - M_{cr}}{\varphi_u - \varphi_{cr}} (\varphi - \varphi_{cr}) + M_{cr} \quad M_{cr} \leq M \leq M_u \quad \varphi_{cr} \leq \varphi \leq \varphi_u \quad (2.1.2)$$

The first cracking moment and first cracking curvature defined as:

$$M_{cr} = \frac{1}{6} b d^2 E \varepsilon_{cr} \quad (2.1.3)$$

$$\varphi_{cr} = \frac{2 \varepsilon_{cr}}{d} \quad (2.1.4)$$

Eq.(2.1.1) and (2.1.2) can be presented in normalized form by introducing two normalizing constants as

$$m'(q') = q' \quad 0 < m' \leq 1 \quad 0 < q' \leq 1 \quad (2.1.5)$$

$$m'(q') = \frac{m-1}{q-1}(q'-1)+1 \quad 1 \leq m' \quad 1 \leq q' \quad (2.1.6)$$

The parameter based moment curvature relationships are therefore:

$$m'(q') = \frac{M'(\varphi)}{M_{cr}}; \quad q' = \frac{\varphi_i}{\varphi_{cr}} \quad m = \frac{M_u}{M_{cr}}; \quad q = \frac{\varphi_u}{\varphi_{cr}} \quad (2.1.7)$$

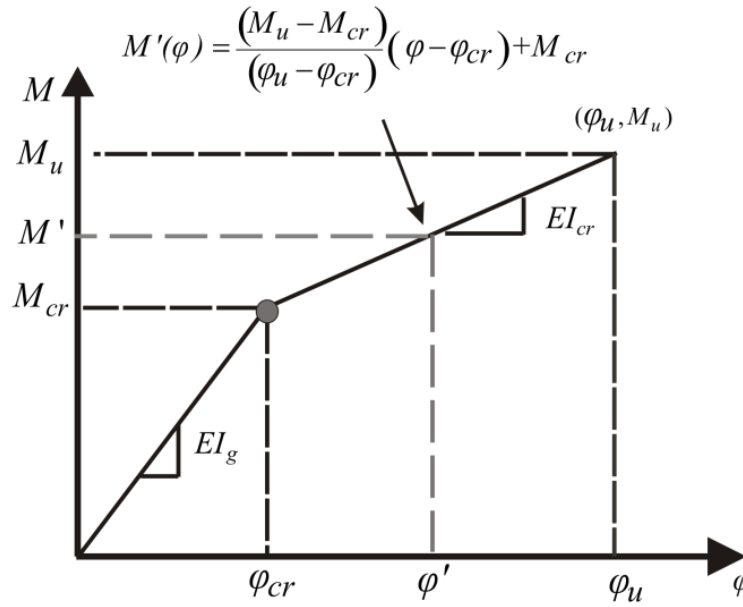


Figure 2.1.1 - Bilinear Moment-Curvature Relationship

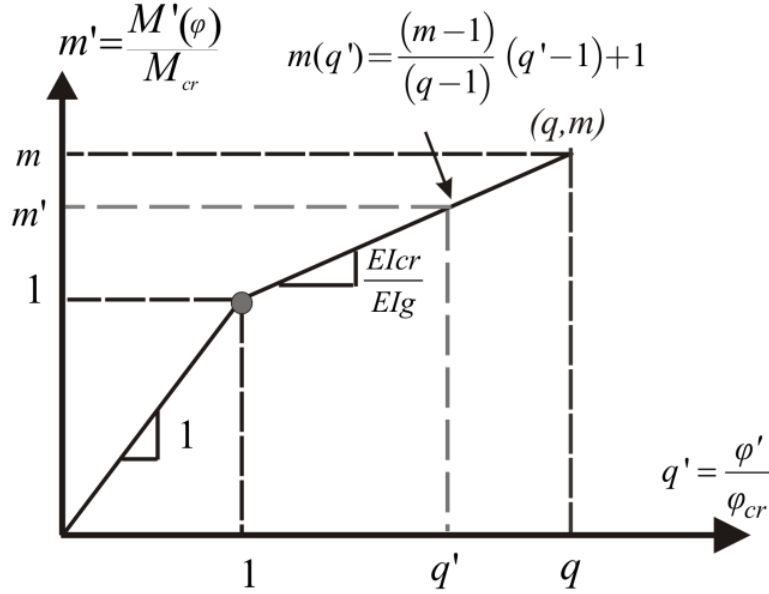


Figure 2.1.2 - Normalized Moment-Curvature Relationship Represented as (q', m')

2.2 Moment-Curvature Distributions

Once the relationship of moment-curvature can be simplified as in Section 2.1, the curvature distributions along the beams are generated based on simplified moment-curvature relationship with known moment distributions. The equilibrium of the beam under the applied load and support conditions is governed by the rotation and displacement boundary conditions and determines the statically determinate distribution of the moment across the length of the beam.

A case of three-point bending of a prismatic beam is presented here to demonstrate the generation of moment and curvature distributions. In Region I, where there is an elastic distribution of moments and curvature, as represented by an increasing moment up until the cracking moment M_{cr} (dash line in Fig. 2.2.1) with $0 \leq M'(x = L/2) \leq M_{cr}$. Since the loading and geometric is symmetric, left-half of beam is considered here. Eq. (2.2.1) shows the relationship of moment at mid-span and the moment at any cross section of x

($x \leq L/2$). Imposed the bilinear moment-curvature relationship, the relationship of curvature at mid-span and curvature at any cross section of x is presented in Eq. (2.2.2)

$$\frac{M'(x)}{M'(x=L/2)} = \frac{2}{L}x \quad \text{for } 0 < x < \frac{L}{2} \quad (2.2.1)$$

$$\varphi_1(x) = \frac{2\varphi'(x=L/2)}{L}x \quad \text{for } 0 < x < \frac{L}{2} \quad (2.2.2)$$

In the general post cracking range, the beam is divided into two distinct regions, where a portion of the beam enters the nonlinear zone. When the moment on the section exceeds the cracking moment, both the moment and curvature distribution are bilinear as a function of the position along the length of the beam, as shown in Figure 2.2.1 (solid line) with $M_{cr} \leq M'(x=L/2) \leq M_u$. Region I and Region II is defined by the coordinate $x=\xi$ such that $M'(x)=M_{cr}$. ξ is obtained from similar triangles of moment distribution diagram as shown in Figure 2.2.1(b). The curvature of two regions as a function of the position along the beam is then represented by relating the curvature distribution using the bilinear assumption.

The curvature distribution is obtained as:

$$\varphi_{21}(x) = \frac{\varphi_{cr}}{\xi}x \quad \text{for } 0 \leq x \leq \xi; \quad (2.2.3)$$

$$\varphi_{22}(x) = \varphi_{cr} \left(\frac{2(q'-1)(x-\xi)}{L-2\xi} + 1 \right) \quad \text{for } \xi \leq x \leq \frac{L}{2} \quad (2.2.4)$$

Wherein $q' = \frac{\varphi'(x=L/2)}{\varphi_{cr}}$

Similar triangles of geometry in Figure 2.2.1(b):

$$m'(x=L/2) = \frac{M'(x=L/2)}{M_{cr}} = \frac{L}{2\xi} \quad (2.2.5)$$

$$\xi = \frac{L}{2m'} \quad (2.2.6)$$

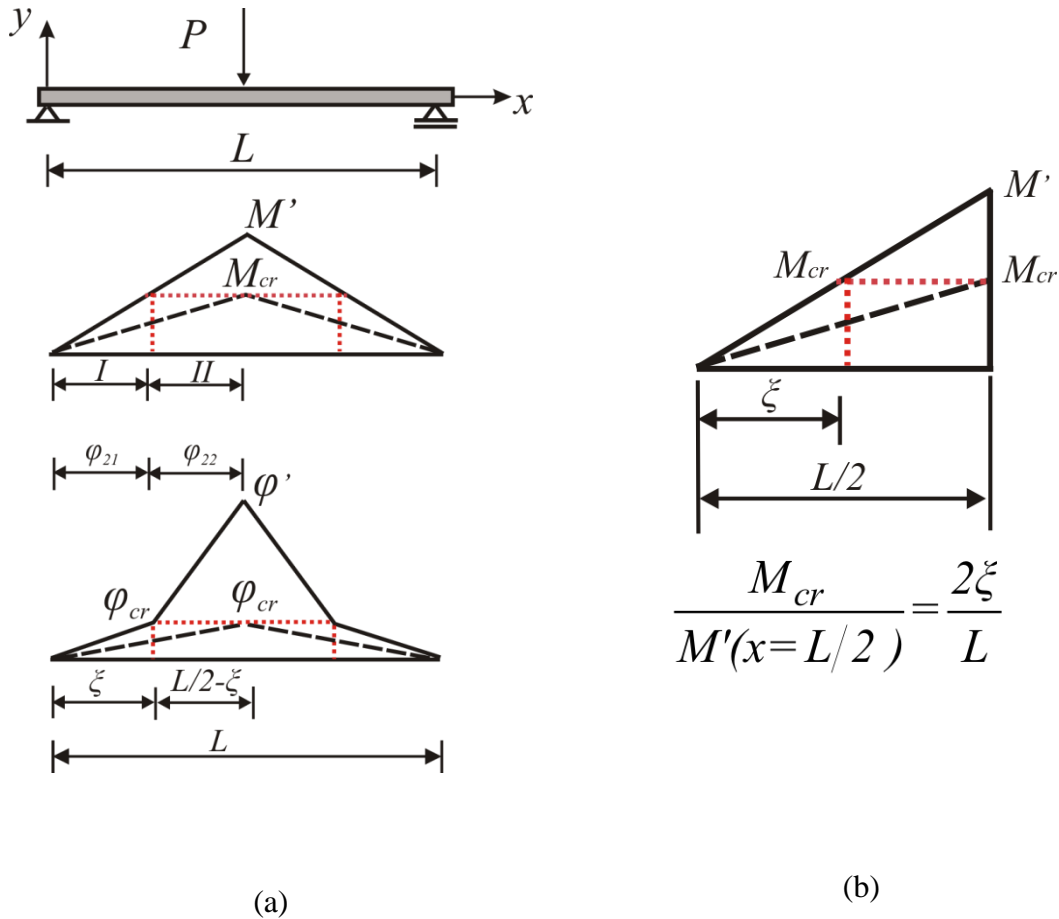


Figure 2.2.1 - Three-Point Bending ;(a) Moment and Curvature Distributions along the Beam;(b) Calculation of ξ ;

Using the same procedure, the moment and curvature distribution along the beam can be generated for a certain loading conditions. Note that the subscript of only '1' means the maximum moment of beam is less than cracking moment, in other word, whole beam is in the pre-cracked region. However, subscript of '2i (i=1,2)' means the some portion of

beam is in the post-creaked region and $i=1$ and 2 means the pre-creaked and post-creaked region, respectively.

2.3 Derivation of Load-Deflection Equations for a Beam in Flexure

Closed-form deflection equations of a beam in flexure are obtained from the analytical integration based on the curvature distribution and boundary conditions. The algorithm of generation of load-deflection equations are shown in Figure 2.3.1.

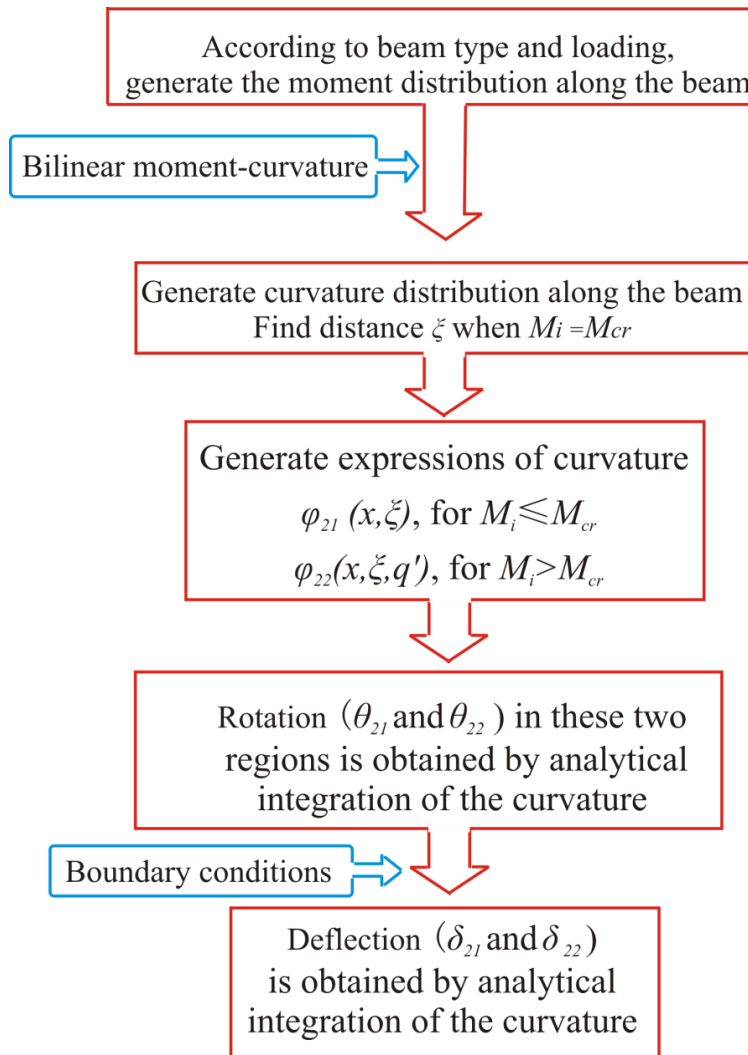


Figure 2.3.1 - Flowchart for the Derivation of Load-Deflection Equation

Calculation of the load-deflection response of an elastic beam is obtained from elementary beam formula up to the point where the linearity condition is satisfied ($q' \leq 1$), i.e. $m'(q') = q' \leq 1$. The procedure for the calculation of the beam deflection profile based on a bilinear moment-curvature response is therefore limited to the case that a portion of the beam is still elastic whereas another portion is in the secondary region with reduced modulus. The applied bending moment of the secondary region is sufficiently large to cause the cracking, i.e. ($m'(q') > 1, q' > 1$) These two regions are defined by the transition point along the length of the beams $x = \xi$ when $m'(q') = m'(x) = 1$. Thus, ξ is the length of origin $x=0$ to the point of $m'(x) = m'(q') = 1$. Figure 2.3.2 shows the pre-cracked and post-cracked regions for general loading for simply supported beam. S_{cr} is defined as post cracking region and $x=L_m$ is defined as the point which is subjected by maximum moment.

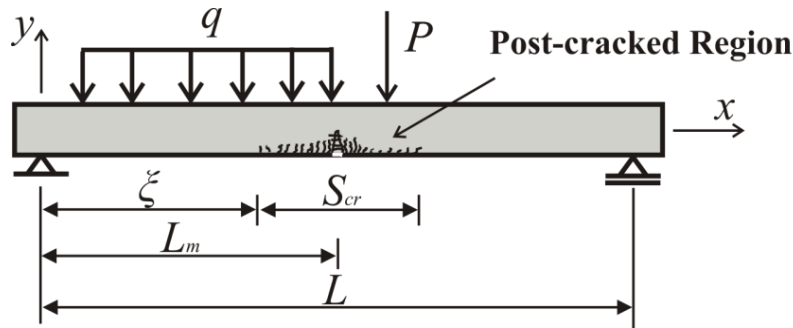


Figure 2.3.2 - Flexural Stiffness Regions for General Loading for Simply Supported Beam

The elastic curve representing deflection depends on the loadings and the flexural stiffness distribution along the beam as well as the continuity of the boundary condition

separating the two regions. The slope of elastic curve at any arbitrary cross section is computed based on the equations (2.3.1) and (2.3.2).

$$\theta_{21} = \int_0^x \varphi_{21}(x) dx + C_1 \quad \text{for } 0 \leq x \leq \xi \quad (2.3.1)$$

$$\theta_{22} = \int_0^{\xi} \varphi_{21}(x) dx + \int_{\xi}^x \varphi_{22}(x) dx + C_2 \quad \text{for } \xi \leq x \leq L_m \quad (2.3.2)$$

Likewise, the distribution of deflection along the beam is computed based on the following:

$$\delta_{21} = \int_0^x \theta_{21}(x) dx + C_3 \quad \text{for } 0 \leq x \leq \xi \quad (2.3.3)$$

$$\delta_{22} = \int_0^{\xi} \theta_{21}(x) dx + \int_{\xi}^x \theta_{22}(x) dx + C_4 \quad \text{for } \xi \leq x \leq L_m \quad (2.3.4)$$

The above integrals are performed after the curvature φ , is related to the magnitude of the moment, M , or expressed as: $\varphi = \varphi(M)$ defined within each segment of bilinear moment curvature model and $M(x)$ is represented as a polynomial function of the beam equilibrium. The constants of integration defined in terms of C_i are numerical values determined based on boundary conditions.

In a case of symmetrical loading and geometry, the boundary conditions at the mid-span are specified by a zero slope. To obtain the slope and deflection prior to cracking, equations (2.3.1) and (2.3.4) are used where the special case of $\xi = L/2$ is used. The general expression of deflection is expressed in terms of equation (10), wherein δ^* is the deflection coefficient:

$$\delta = \delta^* \varphi_{cr} L^2 \quad (2.3.5)$$

Deflection equations for simply supported beam and cantilever beam under different loading conditions for pre-cracked and post-cracked regions are derived in detail in the following section using analytical integrations.

2.3.1 Case 1 – Load-Deflection with Simply Supported Beam

Simply supported beam of length L is considered here with the symmetric loading conditions which are-

- i) Concentrated point load at the mid-span of the beam (3-point bending) (Case 1.1)
- ii) Two concentrated point load with the distance of $3/L$ to either two supports (Case 1.2)
- iii) Two concentrated point load with the distance of a to either two supports (Case 1.3)
- iv) Uniform loading along the beam (Case 1.4)
- v) Concentrated moment at the mid-span of the beam (Case 1.5)
- vi) Two concentrated moment at the two ends of beam (Pure bending) (Case 1.6)

Half of the beam in Case 1 is considered to generate the closed-form deflection equations due to the symmetric loading conditions. The rotation and deflection of the beam are obtained by successive integration and application of the boundary conditions as presented in Section 2.3. The procedure is described in details for the Case 1.1, Case 1.2 and Case 1.3 and then results are presented for other cases.

Case Study 1.1 – Three-point bending

The beam behaves in accordance to the elementary mechanics approaches up until the cracking at a moment equal to $M'(x) = M_{cr}$ or $(m'(x) = I)$. Beyond this moment level, as

the load increases ($m'(x) > I$), the cracking region progresses along the length of the beam, so the length of the cracked region is determined based on the static equilibrium of the moment distribution.

First, considering the maximum moment $M'(x=L/2) \leq M_{cr}$, the whole beam is in the pre-cracked region. The curvature distribution as shown in Equation (2.3.1.1)

$$\varphi_1(x) = \frac{2\varphi'}{L}x, \quad 0 \leq x \leq L/2 \quad (2.3.1.1)$$

The rotation in any cross section is obtained by analytical integration of the curvature distribution as following:

$$\theta_1(x) = \int_0^x \frac{2\varphi'}{L}x dx + C_1, \quad 0 \leq x \leq L/2 \quad (2.3.1.2)$$

C_1 is calculated by imposing the boundary condition of the rotation of mid-span is zero.

The deflection in any cross section is obtained as equation (2.3.1.3):

$$\delta_1(x) = \int_0^x \theta_1(x) dx + C_2, \quad 0 \leq x \leq L/2 \quad (2.3.1.3)$$

Applying the deflection boundary condition at the left support, one could get C_2 equal to zero and the deflection coefficient equation as:

$$\delta_1^* = \left(\frac{x^3}{3L^3} - \frac{x}{4L} \right) q', \quad 0 \leq x \leq L/2 \quad (2.3.1.4)$$

Second, considering the maximum moment $M'(x=L/2) \geq M_{cr}$, the beam can be considered to consist of two distinct regions. The transition point of pre-cracked and post-cracked region is $x = \zeta$. ζ is related to the length of beam and a given value of applied moment defined as $m'(x=L/2) = M'(x=L/2)/M_{cr}$, shown in Figure 2.3.1.1

The two regions of three-point bending beam are defined as:

- 1) Region I ($0 \leq x \leq \xi$), as pre-cracked region.
- 2) Region II ($\xi \leq x \leq L/3$), as the post cracked region.

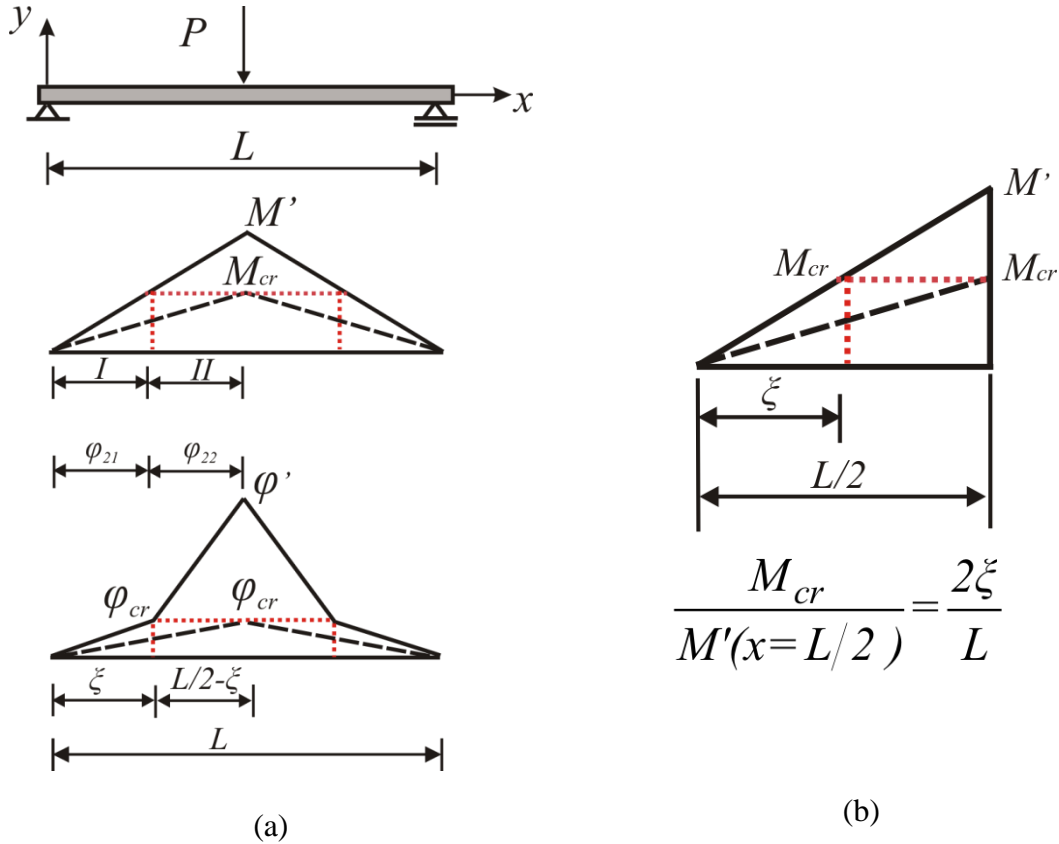


Figure 2.3.1.1 - Three-Point Bending ;(a) Moment and Curvature Distributions along the Beam;(b) Calculation of ξ ;

Curvature distributions for these two regions are presented in the Equation (2.3.1.5) and (2.3.1.6), which are based on the moment distribution shown in in Figure 2.3.1.1(a).

$$\varphi_{21}(x) = \frac{\varphi_{cr}}{\xi} x \quad \text{for } 0 < x < \xi \quad (2.3.1.5)$$

$$\varphi_{22}(x) = \varphi_{cr} \left(\frac{2(q'-1)(x-\xi)}{L-2\xi} + 1 \right) \quad \text{for } \xi \leq x \leq L/2; \quad (2.3.1.6)$$

Wherein,

$$\xi = \frac{L}{2m'}$$

The rotation in any cross section in Region I is obtained by analytical integration of the curvature distribution in Region I as following:

$$\theta_{21}(x) = \int_0^x \frac{\varphi_{cr}}{\xi} x dx + C_3 \quad 0 \leq x \leq \xi \quad (2.3.1.7)$$

Likewise rotation in Region I, rotation in Region II is obtained as below

$$\theta_{22}(x) = \int_0^\xi \frac{\varphi_{cr}}{\xi} x dx + \int_\xi^x \varphi_{cr} \left(\frac{2(q'-1)(x-\xi)}{L-2\xi} + 1 \right) dx + C_4 \quad \xi \leq x \leq L/2 \quad (2.3.1.8)$$

C_3 , C_4 are integration constants determined based on the boundary conditions. The Boundary conditions specific to this case include zero rotation at the middle of the beam as well as continuity of the rotations at the end of Regions I and II from Equations (2.3.1.7) and (2.3.1.8).

The deflection distribution in Region I is obtained by analytical integration of the rotation distribution as:

$$\delta_{21}(x) = \int_0^x \theta_{21}(x) dx + C_5 \quad 0 \leq x \leq \xi \quad (2.3.1.9)$$

Applying the deflection boundary condition at the left support, one could get C_5 equal to zero and the deflection coefficient equation in Region I as:

$$\delta_{21}^* = \frac{x^3}{6L^2\xi} - \frac{(L+Lq'-2q'\xi)x}{4L^2} \quad 0 \leq x \leq \xi \quad (2.3.1.10)$$

Using the above expression for Region I, the deflection equation in Region II is obtained as below

$$\delta_{22} = \delta_{21}(\xi) - \delta_{21}(0) + \int_\xi^x \theta_{22}(x) dx + C_6 \quad \xi \leq x \leq L/2 \quad (2.3.1.11)$$

Applying the boundary condition $\delta_{21}(\xi) = \delta_{22}(\xi)$, one would get $C_6 = 0$ and the deflection coefficient in Region II obtained as (2.3.1.12).

$$\delta_{22}^* = \frac{1}{L-2\xi} \left(\frac{(q'-1)x^3}{3L^2} + \frac{(L-2q'\xi)x^2}{2L^2} + \frac{x(4q'\xi-L-Lq')}{4L} + \frac{(L\xi^2-2q'\xi^3)}{6L^2} \right) \quad (2.3.1.12)$$

Case Study 1.2 –Four-point bend with distance of L/3 to either two supports

First, considering the simulation of maximum moment of beam is less than cracking moment. The maximum moment of four-point bending beam is at $x=L/2$. If the $M'(x=L/2) \leq M_{cr}$, the beam is in the pre-cracked region and the curvature distributions is shown in Equation (2.3.1.13) and (2.3.1.14).

$$\varphi_{1a}(x) = \frac{3\varphi'}{L}x \quad \text{for } 0 \leq x \leq L/3 \quad (2.3.1.13)$$

$$\varphi_{1b}(x) = \varphi' \quad \text{for } L/3 \leq x \leq L/2 \quad (2.3.1.14)$$

The rotation in any cross section is obtained by analytical integration of the curvature distribution as following:

$$\theta_{1a}(x) = \int_0^x \frac{3\varphi'}{L}x dx + C_1 \quad 0 \leq x \leq L/3 \quad (2.3.1.15)$$

$$\theta_{1b}(x) = \int_0^{L/3} \frac{3\varphi'}{L}x dx + \int_{L/3}^x \varphi' dx + C_2 \quad L/3 \leq x \leq L/2 \quad (2.3.1.16)$$

C_2 is calculated by imposing the boundary condition of the rotation of mid-span is zero.

C_1 is calculated by applying the boundary condition $\theta_{1a}(L/3) = \theta_{1b}(L/3)$. The deflection

in any cross section is obtained as equation (2.3.1.17) and (2.3.1.18).

$$\delta_{1a}(x) = \int_0^x \theta_{1a}(x) dx + C_3 \quad 0 \leq x \leq L/3 \quad (2.3.1.17)$$

$$\delta_{1b}(x) = \int_0^{L/3} \theta_{1a}(x) dx + \int_{L/3}^{L/2} \theta_{1b}(x) dx + C_4 \quad L/3 \leq x \leq L/2 \quad (2.3.1.18)$$

Applying the deflection boundary condition at the left support and the continuity of $x=L/3$, one could get C_3 and C_4 equal to zero and the deflection coefficient equation as:

$$\delta_{1a}^* = q' \left(\frac{x^3}{2L^3} - \frac{x}{3L} \right), \quad 0 \leq x \leq L/3 \quad (2.3.1.19)$$

$$, \quad L/3 \leq x \leq L/2 \quad (2.3.1.20)$$

Second, considering the maximum moment $M'(x=L/2) \geq M_{cr}$, the beam can be considered to consist of two distinct regions. The two regions of four-point bending beam are defined as:

- i) Region I ($0 \leq x \leq \xi$), as pre-cracked region.
- ii) Region IIa ($\xi \leq x \leq L/3$), as the post cracked region.
- iii) Region IIb ($L/3 \leq x \leq L/2$), as the post cracked and constant moment region.

Curvature distributions for these three regions are generated based on the moment distribution (shown in Figure 2.3.1.2) and simplified bilinear moment-curvature, presented in the equation (2.3.1.21) to (2.3.1.23). The calculation of ξ is presented in Figure 2.3.1.2(b).

$$\varphi_{21}(x) = \frac{\varphi_{cr}}{\xi} x \quad 0 \leq x \leq \xi \quad (2.3.1.21)$$

$$\varphi_{22a}(x) = \varphi_{cr} \frac{3(q'x - q'\xi - x) + L}{L - 3\xi} \quad \xi \leq x \leq L/3 \quad (2.3.1.22)$$

$$\varphi_{22b}(x) = q' \varphi_{cr} \quad L/3 \leq x \leq L/2 \quad (2.3.1.23)$$

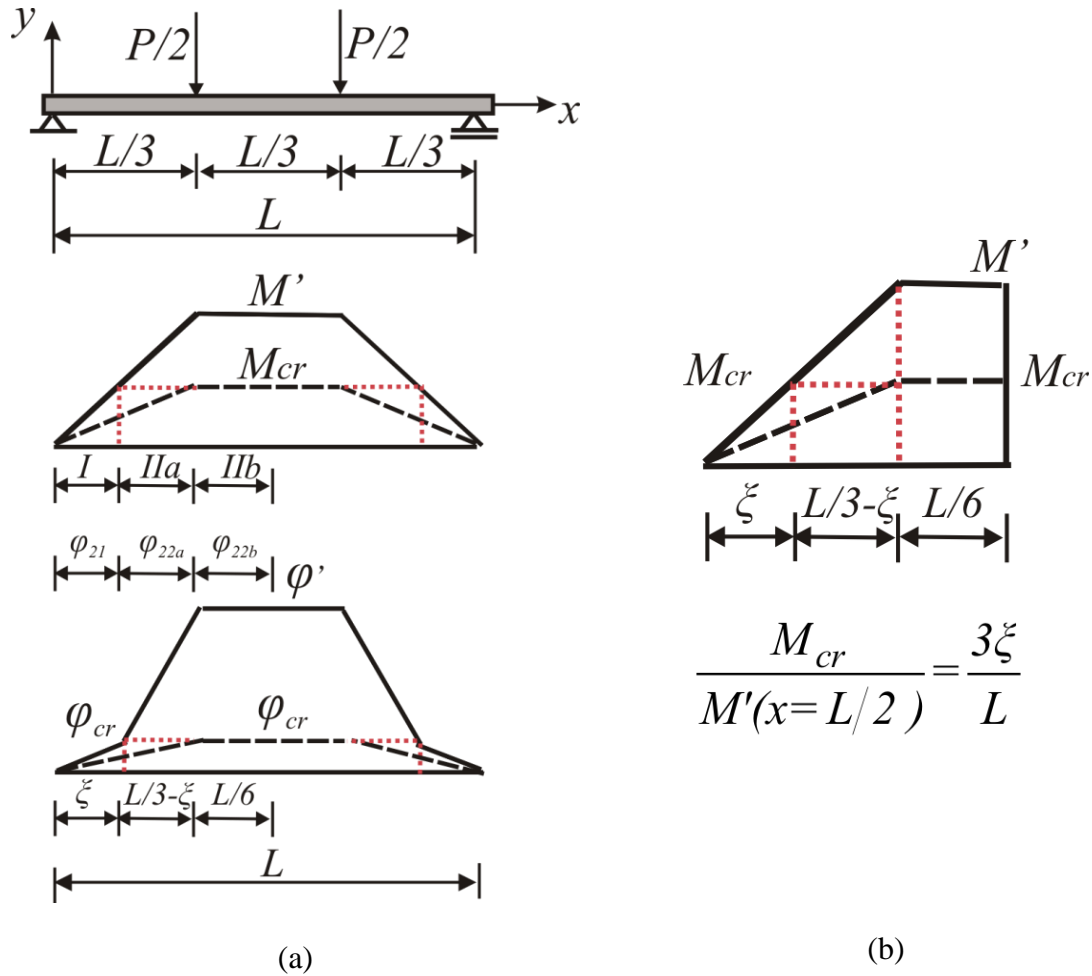


Figure 2.3.1.2 - Four-Point Bending ;(a) Moment and Curvature Distributions along the Beam;(b) Calculation of ξ ;

Wherein,

$$\xi = \frac{L}{3m'}$$

The rotation in any cross section in Region I is obtained by analytical integration of the curvature distribution in Region I as following:

$$\theta_{21}(x) = \int_0^x \frac{\varphi_{cr}}{\xi} x dx + C_5 \quad 0 \leq x \leq \xi \quad (2.3.1.24)$$

Likewise rotation in Region I, rotations in Region IIa and IIb are obtained as below

$$\theta_{22a}(x) = \int_0^{\xi} \frac{\varphi_{cr}}{\xi} x dx + \int_{\xi}^x \varphi_{cr} \frac{3(q'x - q'\xi - x) + L}{L - 3\xi} dx + C_6 \quad \xi \leq x \leq L/3 \quad (2.3.1.25)$$

$$\theta_{22b}(x) = \int_0^{\xi} \frac{\varphi_{cr}}{\xi} x dx + \int_{\xi}^{L/3} \varphi_{cr} \frac{3(q'x - q'\xi - x) + L}{L - 3\xi} dx + \int_{L/3}^x q' \varphi_{cr} dx + C_7 \quad L/3 \leq x \leq L/2 \quad (2.3.1.26)$$

C_5 , C_6 and C_7 are integration constants determined based on the boundary conditions. The Boundary conditions specific to this case include zero rotation at the middle of the beam as well as continuity of the rotations at the end of Regions I and IIa as well as Region IIa and IIb obtained from Equations (2.3.1.24), (2.3.1.25) and (2.3.1.26).

The deflection distribution in Region I is obtained by analytical integration of the rotation distribution as:

$$\delta_{21}(x) = \int_0^x \theta_{21}(x) dx + C_8 \quad 0 \leq x \leq \xi \quad (2.3.1.27)$$

Applying the deflection boundary condition at the left support, one could get C_8 equal to zero and the deflection coefficient equation in Region I as:

$$\delta_{21}^* = \frac{1}{6\xi L^2} \left(x^3 + x(3q'\xi^2 - L\xi - 2\xi Lq') \right) \quad 0 \leq x \leq \xi \quad (2.3.1.28)$$

Using the above expression for Region I, the deflection equation in Region IIa is obtained as below

$$\delta_{22a} = \delta_{21}(\xi) - \delta_{21}(0) + \int_{\xi}^x \theta_{22}(x) dx + C_9 \quad \xi \leq x \leq L/3 \quad (2.3.1.29)$$

Applying the boundary condition $\delta_{21}(\xi) = \delta_{22a}(\xi)$, one would get $C_9 = 0$ and the deflection coefficient in Region IIa obtained as (2.3.1.30).

$$\delta_{22a}^* = \frac{1}{6L^2(L - 3\xi)} \left(3x^3 q' - 3x^3 + 3x^2 L - 9x^2 q' \xi - 2xL^2 q' - xL^2 + 9xLq' \xi + \xi^2 L - 3\xi^3 q' \right)$$

$$\xi \leq x \leq L/3 \quad (2.3.1.30)$$

Similar to the procedure in Region IIa, the deflection equation in Region IIb is written as

$$\delta_{22b}(x) = \delta_{21}(\xi) - \delta_{21}(0) + \delta_{22a}(L/3) - \delta_{22a}(\xi) + \int_{L/3}^x \theta_{22b}(x) dx + C_6$$

$$L/3 \leq x \leq L/2 \quad (2.3.1.31)$$

Deflection compatibility at $x=L/3$ results in $C_6 = 0$ and the expression for deflection coefficient in Region IIb is simplified as shown in equation (2.3.1.32).

$$\delta_{22b}^* = \frac{q'x^2}{2L^2} - \frac{q'x}{2L} + \frac{1}{54} \left(\left(\frac{3\xi}{L} + 1 \right) \left(\frac{3q'\xi}{L} - 1 \right) + q' \right) \quad L/3 \leq x \leq L/2 \quad (2.3.1.32)$$

Case Study 1.3 - Four-point bend with distance of a to either two supports

First, considering the simulation of maximum moment of beam is less than cracking moment. The maximum moment of four-point bending beam is at $x=L/2$. If the $M'(x=L/2) \leq M_{cr}$, the beam is in the pre-cracked region and the curvature distributions is shown in Equation (2.3.1.33) and (2.3.1.34).

$$\varphi_{1a}(x) = \frac{\varphi'}{a} x \quad \text{for } 0 \leq x \leq a \quad (2.3.1.33)$$

$$\varphi_{1b}(x) = \varphi' \quad \text{for } a \leq x \leq L/2 \quad (2.3.1.34)$$

The rotation in any cross section is obtained by analytical integration of the curvature distribution as following:

$$\theta_{1a}(x) = \int_0^x \frac{\varphi'}{a} x dx + C_1 \quad 0 \leq x \leq a \quad (2.3.1.35)$$

$$\theta_{1b}(x) = \int_0^a \frac{\varphi'}{a} x dx + \int_a^x \varphi' dx + C_2 \quad a \leq x \leq L/2 \quad (2.3.1.36)$$

C_1 is calculated by imposing the boundary condition of the rotation of mid-span is zero.

C_2 is calculated by applying the boundary condition $\theta_{1a}(a) = \theta_{1b}(a)$, The expressions of rotation is presented in Equation (2.3.1.37) and (2.3.1.38).

$$\theta_{1a} = \frac{\varphi' x^2}{2a} + \frac{\varphi' a}{2} - \frac{\varphi' L}{2} \quad 0 \leq x \leq a \quad (2.3.1.37)$$

$$\theta_{1b} = \varphi' a + \varphi'(x-a) - \frac{1}{\varphi'} \quad a \leq x \leq L/2 \quad (2.3.1.38)$$

The deflection in any cross section is obtained as:

$$\delta_{1a}(x) = \int_0^x \theta_{1a}(x) dx + C_3 \quad 0 \leq x \leq a \quad (2.3.1.39)$$

$$\delta_{1b}(x) = \int_0^a \theta_{1a}(x) dx + \int_a^{L/2} \theta_{1b}(x) dx + C_4 \quad a \leq x \leq L/2 \quad (2.3.1.40)$$

Applying the deflection boundary condition at the left support and the continuity of $x=a$, one could get C_3 and C_4 equal to zero and the deflection coefficient equation as:

$$\delta_{1a} = \frac{\varphi_{cr} x^3}{6a} - \frac{\varphi_{cr} (-3a^2 + 3La)x}{6a}, \quad 0 \leq x \leq a \quad (2.3.1.41)$$

$$\delta_{1b} = \frac{1}{6} \varphi_{cr} a^2 + \frac{1}{2} \varphi_{cr} x^2 - \frac{1}{2} \varphi_{cr} Lx, \quad a \leq x \leq L/2 \quad (2.3.1.42)$$

Second, considering the maximum moment $M'(x=L/2) \geq M_{cr}$, the beam can be considered to consist of two distinct regions. The two regions of the four-point bending beam are defined as:

- i) Region I ($0 \leq x \leq \xi$), as pre-cracked region.
- ii) Region IIa ($\xi \leq x \leq a$), as the post cracked region.
- iii) Region IIb ($a \leq x \leq L/2$), as the post cracked and constant moment region.

Curvature distributions for these three regions are generated based on the moment distribution (shown in Figure 2.3.1.3) and simplified bilinear moment-curvature, presented in the equation (2.3.1.43) to (2.3.1.45). The calculation of ξ is presented in Figure 2.3.1.3(b).

$$\varphi_{21}(x) = \frac{\varphi_{cr}}{\xi} x \quad 0 \leq x \leq \xi \quad (2.3.1.43)$$

$$\varphi_{22a}(x) = \varphi_{cr} \left(1 + \frac{q'-1}{a-\xi} (x-\xi) \right) \quad \xi \leq x \leq a \quad (2.3.1.44)$$

$$\varphi_{22b}(x) = q' \varphi_{cr} \quad a \leq x \leq L/2 \quad (2.3.1.45)$$

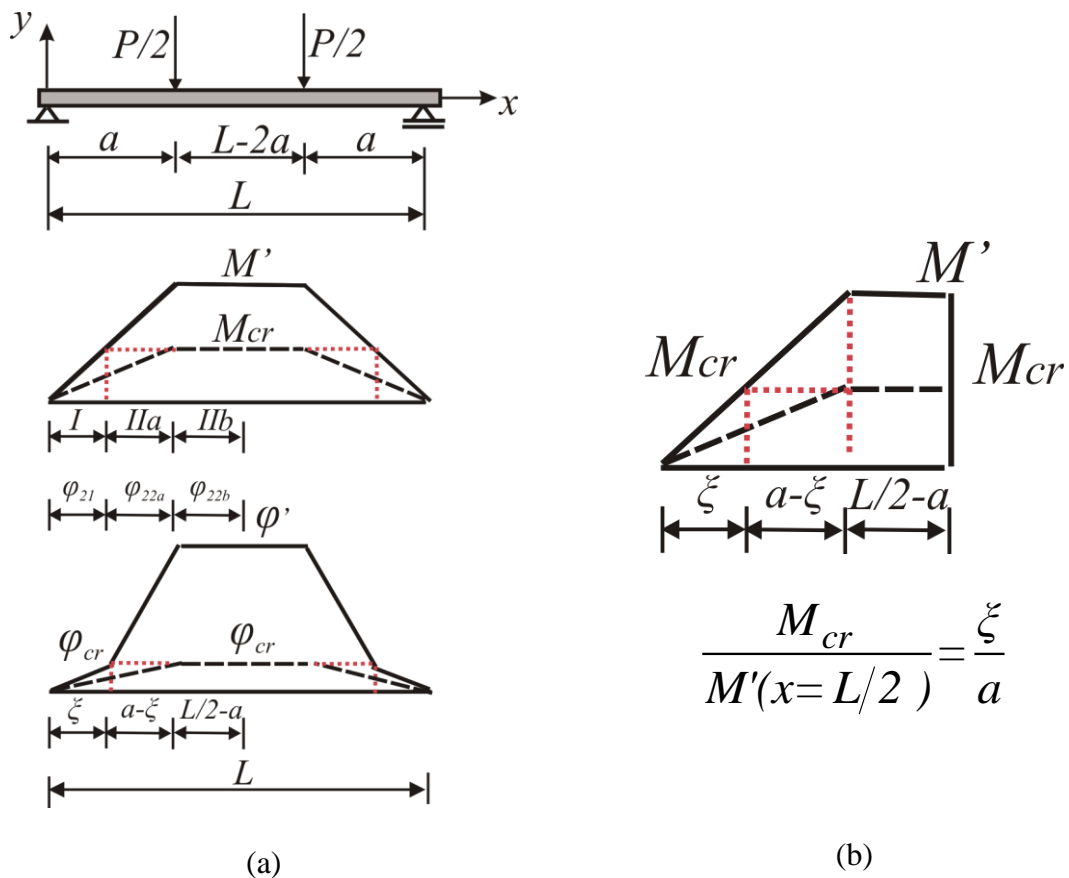


Figure 2.3.1.2 - Four-Point Bending (with arbitrary distance a); (a) Moment and Curvature distributions along the Beam; (b) Calculation of ξ ;

Wherein,

$$\xi = \frac{a}{m'}$$

The rotation in any cross section in Region I is obtained by analytical integration of the curvature distribution in Region I as following:

$$\theta_{21}(x) = \int_0^x \frac{\varphi_{cr}}{\xi} x dx + C_5 \quad 0 \leq x \leq \xi \quad (2.3.1.46)$$

Likewise rotation in Region I, rotations in Region IIa and IIb are obtained as below

$$\theta_{22a}(x) = \int_0^\xi \frac{\varphi_{cr}}{\xi} x dx + \int_\xi^x \varphi_{cr} \left(1 + \frac{q'-1}{a-\xi} (x-\xi) \right) dx + C_6 \quad \xi \leq x \leq a \quad (2.3.1.47)$$

$$\theta_{22b}(x) = \int_0^\xi \frac{\varphi_{cr}}{\xi} x dx + \int_\xi^a \varphi_{cr} \left(1 + \frac{q'-1}{a-\xi} (x-\xi) \right) dx + \int_a^x q' \varphi_{cr} dx + C_7$$

$$a \leq x \leq L/2 \quad (2.3.1.48)$$

C_5 , C_6 and C_7 are integration constants determined based on the boundary conditions. The Boundary conditions specific to this case include zero rotation at the middle of the beam as well as continuity of the rotations at the end of Regions I and IIa as well as Region IIa and IIb obtained from Equations (2.3.1.46), (2.3.1.47) and (2.3.1.48).

The deflection distribution in Region I is obtained by analytical integration of the rotation distribution as:

$$\delta_{21}(x) = \int_0^x \theta_{21}(x) dx + C_8 \quad 0 \leq x \leq \xi \quad (2.3.1.49)$$

Applying the deflection boundary condition at the left support, one could get C_8 equal to zero and the deflection coefficient equation in Region I as:

$$\delta_{21}^* = \frac{x^3}{6\xi L^2} - \frac{(-q'a + a + q'L - q'\xi)x}{2L^2} \quad 0 \leq x \leq \xi \quad (2.3.1.50)$$

Using the above expression for Region I, the deflection equation in Region IIa is obtained as below

$$\delta_{22a} = \delta_{21}(\xi) - \delta_{21}(0) + \int_{\xi}^x \theta_{22}(x) dx + C_9 \quad \xi \leq x \leq a \quad (2.3.1.51)$$

Applying the boundary condition $\delta_{21}(\xi) = \delta_{22a}(\xi)$, one would get $C_9 = 0$ and the deflection coefficient in Region IIa obtained as (2.3.1.52).

$$\delta_{22a}^* = \frac{1}{L^2 6(a-\xi)} \left((q'-1)x^3 - (3\xi q' - 3a)x^2 - (3q'La + 3a^2 - 3q'a^2 - 3q' L\xi)x - (q'\xi^3 - \xi^2 a) \right) \quad \xi \leq x \leq a \quad (2.3.1.52)$$

Similar to the procedure in Region IIa, the deflection equation in Region IIb is written as

$$\delta_{22b}(x) = \delta_{21}(\xi) - \delta_{21}(0) + \delta_{22a}(L/3) - \delta_{22a}(\xi) + \int_{L/3}^x \theta_{22b}(x) dx + C_6 \quad a \leq x \leq L/2 \quad (2.3.1.53)$$

Deflection compatibility at $x = L/3$ results in $C_6 = 0$ and the expression for deflection coefficient in Region IIb is simplified as shown in equation (2.3.1.54).

$$\delta_{22b}^* = \frac{1}{2L^2} q' x^2 - \frac{1}{2L} q' x - \frac{1}{6L^2} (-q'a^2 + a^2 - \xi q'a + a\xi - q'\xi^2) \quad a \leq x \leq L/2 \quad (2.3.1.54)$$

Case 1.4 to Case 1.6 can be derived similarly. Results of load-deflection equations based on bilinear moment-curvature relationship for various loading pattern in summarized in Table 2.3.1 to Table 2.3.3

Table 2.3.1 - Curvature and Deflection of Elastic Region for Simply Supported Beam

| Case # | Beam Type | ϕ_1 | δ_1^* |
|----------|-------------------------|--|--|
| Case 1.1 | 3PB | $\frac{2\phi'}{L}x$ | $q' \left(\frac{x^3}{3L^3} - \frac{x}{4L} \right)$ |
| Case 1.2 | 4PB with L/3 | $x \leq \frac{L}{3}$ | $q' \left(\frac{x^3}{2L^3} - \frac{x}{3L} \right)$ |
| | | $\frac{L}{3} \leq x \leq \frac{L}{2}$ | $q' \left(\frac{x^2}{2L^2} - \frac{x}{2L} + \frac{1}{54} \right)$ |
| Case 1.3 | 4PB with a | $x \leq a$ | $q' \left(\frac{x^3}{6a} - \frac{(-3a^2 + 3La)x}{6a} \right)$ |
| | | $a \leq x \leq \frac{L}{2}$ | $q' \left(\frac{1}{6}a^2 + \frac{1}{2}x^2 - \frac{1}{2}Lx \right)$ |
| Case 1.4 | SS-Uniform loading | $\frac{-4\phi'}{L^2}x^2 + \frac{4\phi'}{L}x$ | $q' \left(\frac{-x^4}{3L^4} + \frac{2x^3}{3L^3} - \frac{x}{3L} \right)$ |
| Case 1.5 | SS-Moment at the middle | $\frac{2\phi'}{L}x$ | $q' \left(\frac{x^3}{3L^3} - \frac{x}{12L} \right)$ |
| Case 1.6 | SS-Pure bending | ϕ' | $q' \left(\frac{x^2}{2L^2} - \frac{x}{2L} \right)$ |

Table 2.3.2 - Curvature and Deflection of Post- cracked Region 1 for Simply Supported
Beam

| Case # | Beam Type | ξ | Region 1 | Curvature φ_{21} | Deflection coefficient δ_{21}^* |
|----------|-------------------------|--|---------------|---|--|
| Case 1.1 | 3PB | $\frac{L}{2m'}$ | $0 < x < \xi$ | $\frac{\varphi_{cr}x}{\xi}$ | $g_1 + g_2$ |
| Case 1.2 | 4PB with 3/L | $\frac{L}{3m'}$ | $0 < x < \xi$ | $\frac{\varphi_{cr}x}{\xi}$ | $f_1(f_2 + f_3)$ |
| Case 1.3 | 4PB with a | $\frac{a}{m'}$ | $0 < x < \xi$ | $\frac{\varphi_{cr}}{\xi} x$ | $s_1 + s_2$ |
| Case 1.4 | SS-Uniform loading | $\frac{L}{2} \left(1 - \sqrt{1 - \frac{1}{m'}} \right)$ | $0 < x < \xi$ | $-\frac{\varphi_{cr}}{\xi(L-\xi)} (x^2 - Lx)$ | j_1 |
| Case 1.5 | SS-Moment at the middle | $\frac{L}{2m'}$ | $0 < x < \xi$ | $\frac{\varphi_{cr}x}{\xi}$ | i_1 |
| Case 1.6 | SS-Pure bending | / | / | $m' \varphi_{cr}$ | $t_1 + t_2$ |

Table 2.3.3 - Curvature and Deflection of Post- cracked Region 2 for Simply Supported
Beam

| C a s e # | Beam Type | ξ | Region 2 | Curvature φ_{22} | Deflection coefficient δ_{22}^* |
|-----------------------|-----------------------------|--|---------------------------------|---|---|
| 1 . 1 | 3PB | $\frac{L}{2m'}$ | $\xi < x < \frac{L}{2}$ | $\varphi_{cr} \left(\frac{2(q'-1)(x-\xi)}{L-2\xi} + 1 \right)$ | $g_3 \left(\begin{matrix} g_4 + g_5 + \\ g_6 + g_7 \end{matrix} \right)$ |
| 1 . 2 | 4PB (L/3) | $\frac{L}{3m'}$ | $\xi < x < \frac{L}{3}$ | $\varphi_{cr} \frac{3(q'x - q'\xi - x) + L}{L - 3\xi}$ | $f_4(f_5 + f_6 + f_7)$ |
| | | | $\frac{L}{3} < x < \frac{L}{2}$ | $q' \varphi_{cr}$ | $f_8 + f_9$ |
| 1 . 3 | 4PB with a | $\frac{a}{m'}$ | $\xi < x < a$ | $\varphi_{cr} \left(1 + \frac{q'-1}{a-\xi} (x-\xi) \right)$ | $s_3(s_4 + s_5 + s_6 + s_7)$ |
| | | | $a < x < \frac{L}{2}$ | $q' \varphi_{cr}$ | $s_8 + s_9 + s_{10}$ |
| 1 . 4 | Unifor m loading | $\frac{L}{2} \left(1 - \sqrt{1 - \frac{1}{m'}} \right)$ | $\xi < x < \frac{L}{2}$ | $\frac{4\varphi_{cr}}{(L-2\xi)^2} \begin{pmatrix} xq'L - q'x^2 \\ -xL + x^2 - \xi q'L \\ + q'\xi^2 + \frac{L^2}{4} \end{pmatrix}$ | $j_2(j_3 + j_4 + j_5 + j_6 + j_7)$ |
| 1 . 5 | Momen t at the middle | $\frac{L}{2m'}$ | $\xi < x < \frac{L}{2}$ | $\varphi_{cr} \left(\frac{2(q'-1)(x-\xi)}{L-2\xi} + 1 \right)$ | i_2 |
| 1 . 6 | Pure bending | / | / | φ | $t_1 + t_2$ |

Table 2.3.4 - Notations of the Deflection Equations for Simply Supported Beam

| | |
|--|--|
| $g_1 = \frac{x^3}{6L^2\xi}$ | $j_1 = -\frac{1}{12} \cdot \frac{x(x^3 - 2Lx^2 + 2\xi L^2 + 4\xi q' L^2 - 12Lq'\xi^2 + 8q'\xi^3)}{\xi(L-\xi) \cdot L^2}$ |
| $g_2 = -\frac{(L + Lq' - 2q'\xi)x}{4L^2}$ | $j_2 = \frac{-1}{12(L-\xi)(L^2 - 4L\xi + 4\xi^2)}$ |
| $g_3 = \frac{1}{L - 2\xi}$ | $j_3 = 2(1 + 2q')xL^2 + (-6x^2 + 2(-\xi - 14\xi q')x - 2\xi^2)L$ |
| $g_4 = \frac{(q'-1)x^3}{3L^2}$ | $j_4 = 8(1 - q')x^3 + 2(3\xi + 2\xi q')x^2$ |
| $g_5 = \frac{(L - 2q'\xi)x^2}{2L^2}$ | $j_5 = 48\xi^2 q'x + 8q'\xi^3 + 3\xi^3$ |
| $g_6 = \frac{x(4q'\xi - L - Lq')}{4L}$ | $j_6 = \frac{4}{L}((q'-1)x^4 + 2(\xi q' - \xi)x^3 - 12\xi^2 q'x^2 - 6q'\xi^3 x - 5q'\xi^4)$ |
| $g_7 = \frac{(L\xi^2 - 2q'\xi^3)}{6L^2}$ | $j_7 = \frac{4}{L^2}(\xi(1 - q')x^4 + 6q'\xi^3 x^2 + 3q'\xi^5)$ |
| $t_1 = \frac{m'x^2}{2L^2}; t_2 = -\frac{m'x}{2L}$ | $i_1 = -\frac{1}{12} \frac{x(-2x^3L + \xi q' L^2 + 2\xi L^2 - 2\xi^2 L - 4\xi^2 q' L + 4q'\xi^3)}{\xi L^3}$ |
| $f_8 = \frac{q'x^2}{2L^2} - \frac{q'x}{2L}$ | $i_2 = -\frac{1}{12} \frac{(6Lq'x\xi - 4q'\xi^3 + 2L\xi^2)(2x - L) + 4L(1 - q')x^3 - 6L^2x^2 + L^3(q' + 2)x}{L^3(L - 2\xi)}$ |
| $f_9 = \frac{1}{54} \left(\left(\frac{3\xi}{L} + 1 \right) \left(\frac{3q'\xi}{L} - 1 \right) + q' \right)$ | $f_4 = \frac{1}{6L^2(L - 3\xi)}$ |
| $s_3 = \frac{1}{L^2 6(a - \xi)}$ | $f_5 = 3x^3 q' - 3x^3 + 3x^2 L$ |
| $s_4 = (q' - 1)x^3$ | $f_6 = -9x^2 q' \xi - 2xL^2 q' - xL^2$ |
| $s_5 = -(3\xi q' - 3a)x^2$ | $f_7 = 9xLq' \xi + \xi^2 L - 3\xi^3 q'$ |
| $s_6 = -(3q'La + 3a^2 - 3q'a^2 - 3q'L\xi)x$ | $f_1 = \frac{1}{6\xi L^2}; f_2 = x^3$ |
| $s_7 = -(q'\xi^3 - \xi^2 a)$ | $f_3 = x(3q'\xi^2 - L\xi - 2\xi Lq')$ |
| | $s_1 = \frac{x^3}{6\xi L^2}, s_2 = -\frac{(-q'a + a + q'L - q'\xi)x}{2L^2}$ |
| | $s_8 = \frac{1}{2L^2} q'x^2, s_9 = -\frac{1}{2L} q'x$ |
| | $s_{10} = -\frac{1}{6L^2} (-q'a^2 + a^2 - \xi q'a + a\xi - q'\xi^2)$ |

2.3.2 Case 2- Load-Deflection with Cantilever Beam

Cantilever beam of length L is considered here with three different loading conditions which are-

- i) Concentrated point load at the free end (Case 2.1)
- ii) Uniform loading along the beam (Case 2.2)
- iii) Concentrated point load at the arbitrary cross-section with the distance S from the fixed end (Case 2.3)

The rotation and deflection of the beam are obtained by successive integration and application of the boundary conditions as presented in Section 2.3. The procedure is described in details for the Case 2.1 and Case 2.2. The summery results are presented in Table 2.3.5 to 2.3.7

Case Study 2.1 –Cantilever beam with concentrated point load at the free end

The coordinate system remains the same as the left end of the beam is the origin and the positive direction of x - and y -axis as shown in Figure 2.3.2.1. The derivation of closed-form deflection equations for cantilever beam presented here based on the assumptions of left end of beam is fixed and right end of beam is free.

First, considering the maximum moment $M'(x=0) \leq M_{cr}$, the whole beam is in the pre-cracked region. The curvature distribution is shown in Equation (2.3.2.1).

$$\varphi_1(x) = \frac{\varphi'}{L}(x-L) \quad 0 \leq x \leq L \quad (2.3.2.1)$$

The rotation in any cross section is obtained by analytical integration of the curvature distribution as following:

$$\theta_1(x) = \int_0^x \frac{\varphi'}{L}(x-L)dx + C_1 \quad 0 \leq x \leq L \quad (2.3.2.2)$$

Imposing the boundary condition of the rotation of fixed end is zero to get $C_1=0$. The rotation in any cross section is obtained as equation (2.3.2.3):

$$\theta_1(x) = \frac{\varphi'}{L} \left(Lx - \frac{1}{2}x^2 \right) \quad 0 \leq x \leq L \quad (2.3.2.3)$$

The deflection in any cross section is calculated by:

$$\delta_1(x) = \int_0^x \theta_1(x)dx + C_2 \quad 0 \leq x \leq L \quad (2.3.2.4)$$

Applying the deflection boundary condition at the fixed end, one could get C_2 equal to zero and the deflection coefficient equation as:

$$\delta_1^* = q' \left(\frac{-x^3}{6L^3} + \frac{x^2}{2L^2} \right) \quad 0 \leq x \leq L \quad (2.3.2.5)$$

Second, considering the maximum moment $M'(x=0) \geq M_{cr}$, the beam can be considered to consist of two distinct regions. The transition point of pre-cracked and post-cracked region is $x = \xi$. ξ is related to the length of beam and a given value of applied moment defined as $m'(x=L/2) = M'(x=L/2)/M_{cr}$, shown in Figure 2.3.2.1

The two regions of cantilever beam subjected with the point load at the free end are defined as:

1) Region I ($\xi \leq x \leq L$), as pre-cracked region.

2) Region II ($0 \leq x \leq \xi$), as the post cracked region.

Curvature distributions for these two regions are presented in the Equation (2.3.2.6) and (2.3.2.7), which are based on the moment distribution shown in in Figure 2.3.1.1(a).

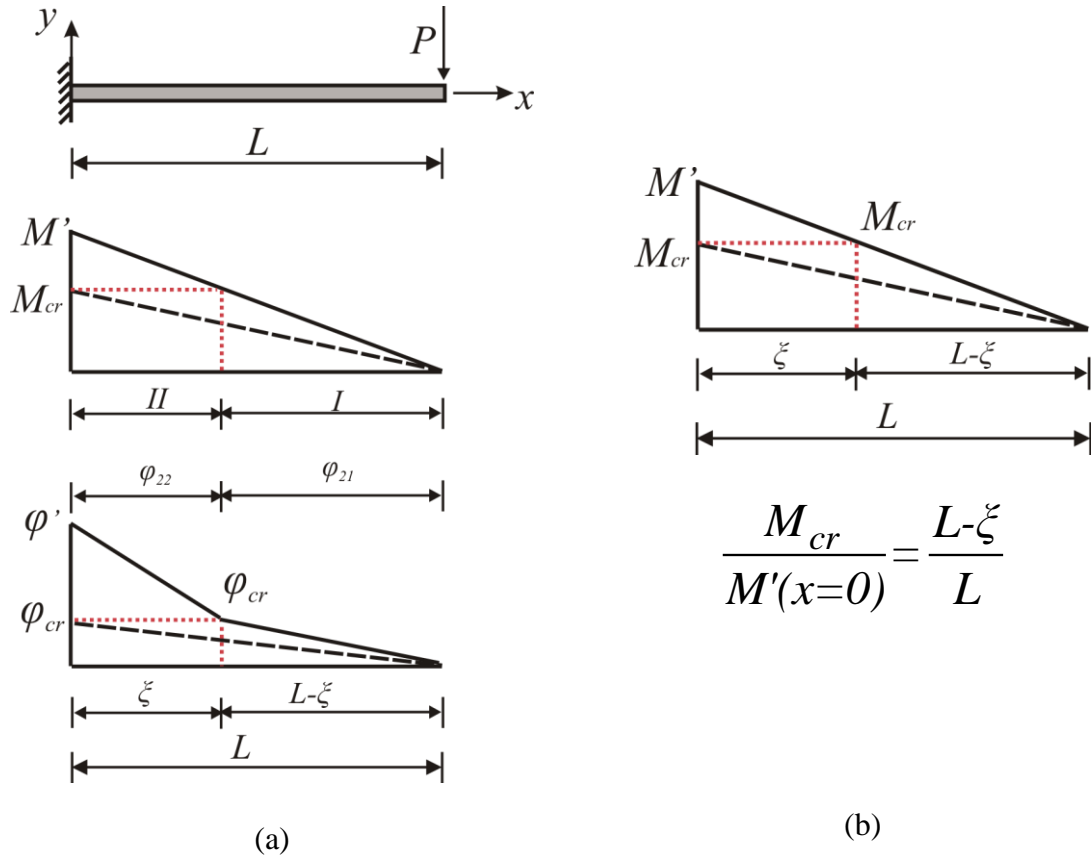


Figure 2.3.2.1 - Cantilever Beam Subjected with Point Load at Free End;(a) Moment and Curvature Distributions along the Beam;(b) Calculation of ξ ;

$$\varphi_{21}(x) = \frac{\varphi_{cr}(x-L)}{L-\xi}, \quad \xi < x < L \quad (2.3.2.6)$$

$$\varphi_{22}(x) = \varphi_{cr} \left(\frac{(q'-1)(x-\xi)}{\xi} - 1 \right), \quad 0 < x < \xi \quad (2.3.2.7)$$

Wherein,

$$\xi = \left(1 - \frac{1}{m'} \right) L$$

The order of integrations of rotation and deflection for this case is different with the simply supported beam, which is first to get the rotation and deflection of Region II and

then to calculate that of Region I. The rotation in any cross section in Region II is obtained by analytical integration of the curvature distribution in Region I as following:

$$\theta_{22}(x) = \int_0^x \varphi_{cr} \left(\frac{(q'-1)(x-\xi)}{\xi} - 1 \right) dx + C_3 \quad 0 < x < \xi \quad (2.3.2.8)$$

The rotation in Region I is obtained as below:

$$\theta_{21}(x) = \int_0^\xi \varphi_{cr} \left(\frac{(q'-1)(x-\xi)}{\xi} - 1 \right) dx + \int_\xi^x \frac{\varphi_{cr}(x-L)}{L-\xi} dx + C_4 \quad \xi < x < L \quad (2.3.2.9)$$

C_3 , C_4 are integration constants determined based on the boundary conditions. The Boundary conditions specific to this case include zero rotation at the left end of the beam as well as continuity of the rotations at the transition point of Regions I and II. The deflection distribution in Region II is obtained by analytical integration of the rotation distribution as:

$$\delta_{22}(x) = \int_0^x \theta_{22}(x) dx + C_5 \quad 0 < x < \xi \quad (2.3.2.10)$$

Applying the deflection boundary condition at the free end of beam, one could get C_5 equal to zero and the deflection coefficient equation in Region I as:

$$\delta_{22}^* = -\frac{(1-q')x^3}{6L^2\xi} - \frac{q'x^2}{2L^2} \quad 0 < x < \xi \quad (2.3.2.11)$$

Using the above expression for Region II, the deflection equation in Region I is obtained as below

$$\delta_{21} = \delta_{22}(\xi) - \delta_{22}(0) + \int_\xi^x \theta_{21}(x) dx + C_6 \quad \xi < x < L \quad (2.3.2.12)$$

Applying the boundary condition $\delta_{21}(\xi) = \delta_{22}(\xi)$, one would get $C_6 = 0$ and the deflection coefficient in Region II obtained as (2.3.1.13).

$$\delta_{21}^* = \frac{1}{L-2\xi} \left(\frac{(q'-1)x^3}{3L^2} + \frac{(L-2q'\xi)x^2}{2L^2} + \frac{x(4q'\xi-L-Lq')}{4L} + \frac{(L\xi^2-2q'\xi^3)}{6L^2} \right)$$

$$\xi < x < L \quad (2.3.2.13)$$

Case Study 2.2 –Cantilever beam subjected with the uniform loading

The moment and curvature distributions are obtained from the static equilibrium and bilinear moment-curvature relationship as shown in Figure 2.3.2.2. First, considering the maximum moment $M'(x=0) \leq M_{cr}$, the whole beam is in the pre-cracked region. The curvature distribution is shown in Equation (2.3.2.14).

$$\frac{-\varphi'}{L^2}x^2 + \frac{2\varphi'}{L}x - \varphi' \quad 0 \leq x \leq L \quad (2.3.2.14)$$

The rotation in any cross section is obtained by analytical integration of the curvature distribution as following:

$$\theta_1(x) = \int_0^x \left(\frac{-\varphi'}{L^2}x^2 + \frac{2\varphi'}{L}x - \varphi' \right)' dx + C_1 \quad 0 \leq x \leq L \quad (2.3.2.15)$$

Imposing the boundary condition of the rotation of fixed end is zero to get $C_1 = -\varphi'L/3$.

The rotation in any cross section is obtained as equation (2.3.2.16):

$$\theta_1(x) = -\frac{4\varphi'}{3L^2}x^2 + \frac{2\varphi'}{L}x - \frac{\varphi'}{3} \quad 0 \leq x \leq L \quad (2.3.2.16)$$

The deflection in any cross section is calculated by:

$$\delta_1(x) = \int_0^x \theta_1(x) dx + C_2 \quad 0 \leq x \leq L \quad (2.3.2.17)$$

Applying the deflection boundary condition at the fixed end, one could get C_2 equal to zero and the deflection coefficient equation as:

$$\delta_1^* = q' \left(\frac{x^4}{12L^4} - \frac{x^3}{3L^3} + \frac{x^2}{2L^2} \right) \quad 0 \leq x \leq L \quad (2.3.2.18)$$

Second, considering the maximum moment $M'(x=0) \geq M_{cr}$, the beam can be considered to consist of two distinct regions. The transition point of pre-cracked and post-cracked region is $x = \xi$. ξ is related to the length of beam and a given value of applied moment defined as $m'(x=L/2) = M'(x=L/2)/M_{cr}$, shown in Figure 2.3.2.2

The two regions of cantilever beam subjected with the point load at the free end are defined as:

1) Region I ($\xi \leq x \leq L$), as pre-cracked region.

2) Region II ($0 \leq x \leq \xi$), as the post cracked region.

Curvature distributions for these two regions are presented in the Equation (2.3.2.19) and (2.3.2.20), which are based on the moment distribution shown in Figure 2.3.1.1(a).

$$\varphi_{21}(x) = \frac{\varphi_{cr}(-x^2 + 2Lx - L^2)}{L^2 - 2L\xi + \xi^2}, \quad \xi < x < L \quad (2.3.2.19)$$

$$\varphi_{22}(x) = \varphi_{cr} \left(\frac{(q'-1)(x^2 - 2Lx)}{(\xi^2 - 2L\xi)} - q' \right) \quad 0 < x < \xi \quad (2.3.2.20)$$

Wherein,

$$\xi = \left(1 - \sqrt{\frac{1}{m'}} \right) L$$

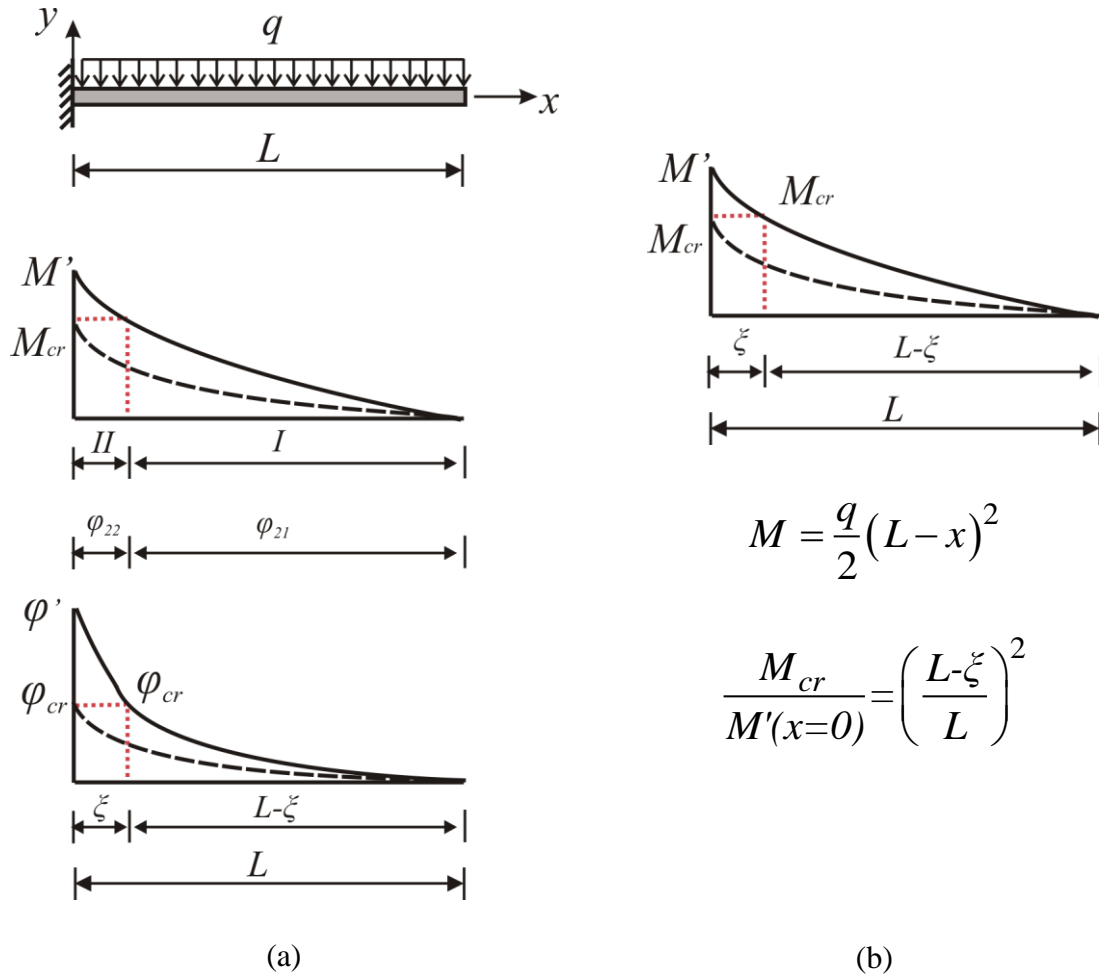


Figure 2.3.2.2 - Cantilever Beam Subjected with Uniform Loading ;(a) Moment and Curvature Distributions along the Beam;(b) Calculation of ξ ;

The rotation in any cross section in Region II is obtained by analytical integration of the curvature distribution in Region I as following:

$$\theta_{22}(x) = \int_0^x \varphi_{cr} \left(\frac{(q'-1)(x^2 - 2Lx)}{(\xi^2 - 2L\xi)} - q' \right) dx + C_3 \quad 0 < x < \xi \quad (2.3.2.21)$$

The rotation in Region I is obtained as below:

$$\theta_{21}(x) = \int_0^{\xi} \varphi_{cr} \left(\frac{(q'-1)(x-\xi)}{\xi} - 1 \right) dx + \int_{\xi}^x \left(\frac{\varphi_{cr}(-x^2 + 2Lx - L^2)}{L^2 - 2L\xi + \xi^2} \right) dx + C_4 \quad \xi < x < L \quad (2.3.2.22)$$

C_3, C_4 are integration constants determined based on the boundary conditions. The Boundary conditions specific to this case include zero rotation at the left end of the beam as well as continuity of the rotations at the transition point of Regions I and II. The deflection distribution in Region II is obtained by analytical integration of the rotation distribution as:

$$\delta_{22}(x) = \int_0^x \theta_{22}(x) dx + C_5 \quad 0 < x < \xi \quad (2.3.2.23)$$

Applying the deflection boundary condition at the fixed end of beam, one could get C_5 equal to zero and the deflection coefficient equation in Region I as:

$$\delta_{21}^* = -\frac{1}{12} \frac{(q'x^2 - 4xq'L - x^2 + 4Lx + 12q'\xi L - 6q'\xi^2)x^2}{L^2(2L-\xi)\xi} \quad 0 < x < \xi \quad (2.3.2.24)$$

Using the above expression for Region I, the deflection equation in Region II is obtained as below

$$\delta_{21} = \delta_{22}(\xi) - \delta_{22}(0) + \int_{\xi}^x \theta_{21}(x) dx + C_6 \quad \xi < x < L \quad (2.3.1.25)$$

Applying the boundary condition $\delta_{21}(\xi) = \delta_{22}(\xi)$, one would get $C_6 = 0$ and the deflection coefficient in Region I obtained as (2.3.1.26).

$$\delta_{21}^* = n_1(n_2 + n_3 + n_4) \quad \xi < x < L \quad (2.3.1.26)$$

Wherein,

$$n_1 = \frac{1}{12(1-A)};$$

$$n_2 = -\frac{(1-A)}{AL^2} \left(\frac{x^4}{L^2} - \frac{4x^3}{L} + 6x^2 \right);$$

$$n_3 = \frac{12x(1-Aq')}{L} + \frac{4x(q'A-1)}{LA} - \frac{8x\sqrt{A}(1-Aq')}{L}$$

$$n_4 = (1-Aq')(8\sqrt{A}-3A-6) + \frac{1}{A} - q';$$

$$A = \left(1 - \frac{\xi}{L}\right)^2$$

Case 2.3 can be derived similarly. Results of load-deflection equations are summarized in Table 2.3.5 to Table 2.3.7

Table 2.3.5 - Curvature and Deflection of Elastic Region for Cantilever Beam

| Case # | Beam Type | | φ_1 | δ_1^* |
|----------|---------------------|-------------------|--|---|
| Case 2.1 | C-Load at the end | | $\frac{\varphi'}{L}(x-L)$ | $q' \left(\frac{-x^3}{6L^3} + \frac{x^2}{2L^2} \right)$ |
| Case 2.2 | C-Uniform loading | | $\frac{-\varphi'}{L^2}x^2 + \frac{2\varphi'}{L}x - \varphi'$ | $q' \left(\frac{x^4}{12L^4} - \frac{x^3}{3L^3} + \frac{x^2}{2L^2} \right)$ |
| Case 2.3 | C-Load at any point | $0 \leq x \leq S$ | $\frac{\varphi'}{S}(x-S)^*$ | $q' \left(\frac{-x^3}{6S^3} + \frac{x^2}{2S^2} \right)$ |
| | | $S \leq x \leq L$ | 0 | $q' \left(\frac{x}{2S} - \frac{1}{6} \right)$ |

Table 2.3.6 - Curvature and Deflection of Post-cracked Region 1 for Cantilever Beam

| Case # | Beam Type | ξ | Region 1 | Curvature φ_{21} | Deflection coefficient δ_{21}^* |
|----------|---------------------|--|---------------|--|--|
| Case 2.1 | C-Load at the end | $\xi = (1 - \frac{1}{m'})L$ | $\xi < x < L$ | $\frac{\varphi_{cr}(x-L)}{L-\xi}$ | u_1 |
| Case 2.2 | C-Uniform loading | $L \left(1 - \sqrt{\frac{1}{m'}} \right)$ | $\xi < x < L$ | $\frac{\varphi_{cr}(-x^2 + 2Lx - L^2)}{L^2 - 2L\xi + \xi^2}$ | $n_1(n_2 + n_3 + n_4)$ |
| Case 2.3 | C-Load at any point | $\xi = (1 - \frac{1}{m'})S$ | $\xi < x < S$ | $\frac{\varphi_{cr}(x-S)}{S-\xi}$ | $c_1(c_2 + c_3 + c_4)$ |
| | | | $S < x < L$ | 0 | $c_5(c_6 + c_7 + c_8)$ |

Table 2.3.7 - Curvature and Deflection of Post- cracked Region 2 for Cantilever Beam

| Case # | Beam Type | ξ | Region 2 | Curvature φ_{22} | Deflection coefficient δ_{22}^* |
|----------|---------------------|--|---------------|--|--|
| Case 2.1 | C-Load at the end | $\xi = (1 - \frac{1}{m'})L$ | $0 < x < \xi$ | $\varphi_{cr} \left(\frac{(q'-1)(x-\xi)}{\xi} - 1 \right)$ | u_2 |
| Case 2.2 | C-Uniform loading | $L \left(1 - \sqrt{\frac{1}{m'}} \right)$ | $0 < x < \xi$ | $\varphi_{cr} \left(\frac{(q'-1)(x^2 - 2Lx)}{(\xi^2 - 2L\xi)} - q' \right)$ | n_5 |
| Case 2.3 | C-Load at any point | $\xi = (1 - \frac{1}{m'})S$ | $0 < x < \xi$ | $\varphi_{cr} \left(\frac{(q'-1)(x-\xi)}{\xi} - 1 \right)$ | $c_9 + c_{10}$ |

Table 2.3.8 - Notations of the Deflection Equations for Cantilever Beam

| | |
|--|--|
| $c_1 = -\frac{1}{6SL^2}$ $c_2 = -\xi^2 Sq' - 2\xi^2 S - m'x^3$ $c_3 = -2m'\xi^3 + 3m'Sx^2 + 3m'S\xi^2$ $c_4 = 3\xi Sq'x + 3\xi Sx + 3m'\xi^2x - 6m'S\xi x$ $c_5 = \frac{1}{6SL^2}$ $c_6 = -3\xi Sxq - 3\xi Sx - 3mxS^2$ $c_7 = -3m\xi^2x + 6mS\xi x + \xi^2 Sq$ $c_8 = 2\xi^2 S + mS^3 + 2m\xi^3 - 3mS\xi^2$ $c_9 = \frac{(q'-1)(x^3 - 3\xi x^2)}{6\xi L^2}; c_{10} = -\frac{x^2}{2L^2}$ | $u_1 = \frac{x^3 - 3x^2L + 3\xi Lx - 3q\xi Lx + 3q\xi^2x - \xi^2L + q\xi^2L - q\xi^3}{6L^2(L-\xi)}$ $u_2 = -\frac{(1-q')x^3}{6L^2\xi} - \frac{q'x^2}{2L^2}$ $n_1 = \frac{1}{12(1-A)}$ $n_2 = -\frac{(1-A)}{AL^2} \left(\frac{x^4}{L^2} - \frac{4x^3}{L} + 6x^2 \right) +$ $n_3 = \frac{12x(1-Aq')}{L} + \frac{4x(q'A-1)}{LA} - \frac{8x\sqrt{A}(1-Aq')}{L}$ $n_4 = (1-Aq')(8\sqrt{A}-3A-6) + \frac{1}{A} - q'; A = \left(1 - \frac{\xi}{L} \right)^2$ $n_5 = -\frac{1}{12} \frac{(q'x^2 - 4xq'L - x^2 + 4Lx + 12q'\xi L - 6q'\xi^2)x^2}{L^2(2L-\xi)\xi}$ |
|--|--|

2.4 Parametric Study and 2-D Contour

Two parameters are considered here for parametric study- normalized moment m' and normalized curvature q' . It is obvious that these two parameters mainly affect the deflection coefficient derived from Section 2.3. Two sets of parametric studies are conducted here to address the effect of moment-curvature models on the load-deflection response. One is the normalized curvature distribution along the beam with different m' or q' . Another one is the deflection coefficient distribution along the beam with different m' and q' .

2.4.1 Normalized Curvature Distribution

Assume the length of beam is unit length which is equal to one ($L=1$) and choose the three levels of normalized moment m' equal to 1.2, 1.5 and 1.8 with a constant normalized curvature $q'=2$ or choose the three levels of normalized curvature q' equal to 2, 2.5, 5 with a constant normalized moment $m'=2$, the normalized curvature distribution equations can be obtained by substituting one pair of parameters and unit length of beam in the curvature equations calculated in Section 2.3 for different types of beam. The derivation of normalized curvature equations with current parameters for three-point bending beam is presented here.

Based on the bilinear moment-curvature models and the derivation of curvature distributions discussed early, the curvature distribution along beam for three-point beam as re-call here in Eq. (2.4.1.1) and (2.4.1.2) with $\xi=L/2m'$.

$$\varphi_{21}(x) = \frac{\varphi_{cr}}{\xi} x \quad 0 < x < \xi \quad (2.4.1.1)$$

$$\varphi_{22}(x) = \varphi_{cr} \left(\frac{2(q'-1)(x-\xi)}{L-2\xi} + 1 \right) \quad \xi \leq x \leq L/2 \quad (2.4.1.2)$$

The normalized curvature distribution can be obtained by divided cracking curvature φ_{cr} on both side in Eq. (2.4.1.1) and (2.4.1.2), as shown in below.

$$\frac{\varphi_{21}(x)}{\varphi_{cr}} = \frac{1}{\xi} x \quad 0 < x < \xi \quad (2.4.1.3)$$

$$\frac{\varphi_{22}(x)}{\varphi_{cr}} = \frac{2(q'-1)(x-\xi)}{L-2\xi} + 1 \quad \xi \leq x \leq L/2 \quad (2.4.1.4)$$

Substituting the constant normalized moment $m'=2$, normalized curvature $q'=2, 2.5, 5$ and unit length $L=1$ in Eq. (2.4.1.1) and Eq. (2.4.1.2). The normalized curvature distribution equations are shown in Table 2.4.1.

Table 2.4.1 - Normalized Curvature Equations with Constant m' for 3PB Beam

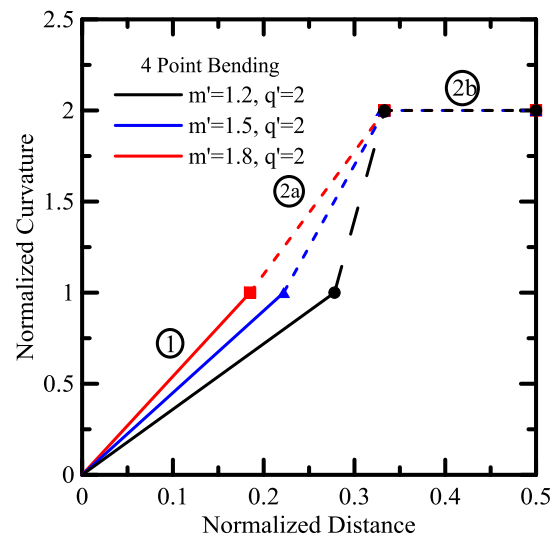
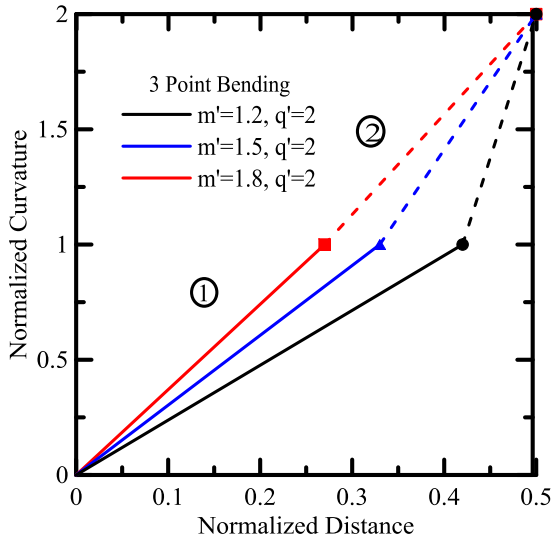
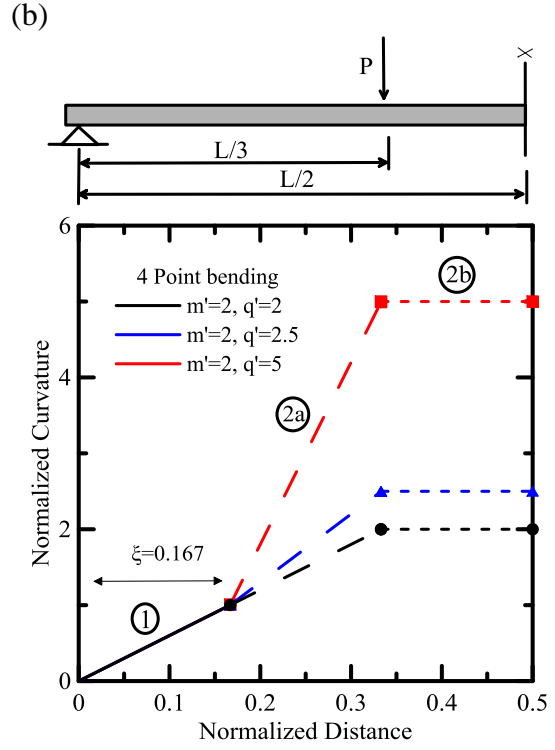
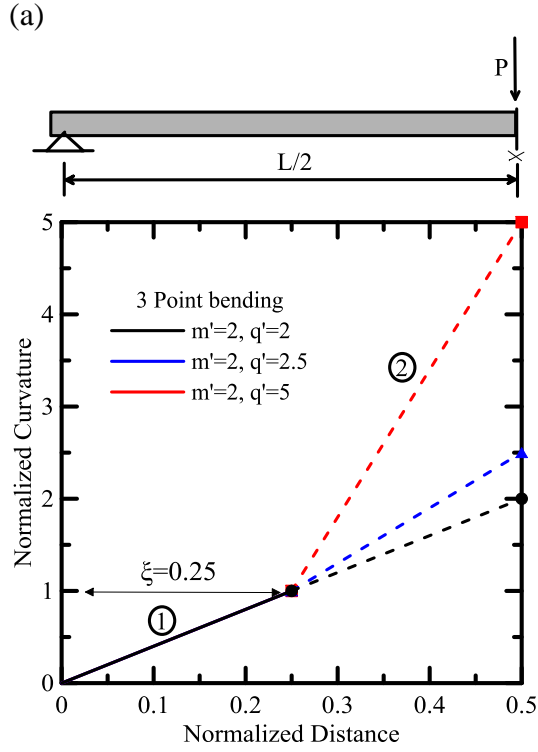
| m' | ξ | q' | Normalized curvature equation | |
|------|-------|------|-------------------------------|----------------|
| | | | φ_{21} | φ_{22} |
| 2 | 0.25 | 2 | $4x$ | $4x$ |
| 2 | 0.25 | 2.5 | $4x$ | $6x-0.5$ |
| 2 | 0.25 | 5 | $4x$ | $16x-3$ |

Substituting the constant normalized curvature $q'=2$, normalized moment $m'=1.2, 1.5, 1.8$ and unit length $L=1$ in the Eq. (2.4.1.1) and Eq. (2.4.1.2). The normalized curvature distribution equations are shown in Table 2.4.2.

Table 2.4.2 - Normalized Curvature Equations with Constant q' for 3PB Beam

| m' | ξ | q' | Normalized curvature equation | |
|------|-------|------|-------------------------------|----------------|
| | | | φ_{21} | φ_{22} |
| 1.2 | 0.42 | 2 | $2.38x$ | $12.5x-4.25$ |
| 1.5 | 0.33 | 2 | $3.03x$ | $5.88x-0.94$ |
| 1.8 | 0.27 | 2 | $3.70x$ | $4.35x-0.17$ |

Using the same procedure, the normalized curvature distributions along the beam for other cases with different pairs of parameters also can be obtained. Figure 2.4.1 shows the effects of m' and q' on normalized curvature distributions for simply supported beam with different loading cases. Figure 2.4.2 shows the effects of m' and q' on normalized curvature distributions for cantilever beam with different loading cases. It is obvious that increasing the normalized moment m' or normalized curvature q' , increases the curvature responses along the beam. Three levels of q' are 2, 2.5, 5 with a fixed $m'=2$, which means the post-cracked stiffness decreases from 1 to 0.667 to 0.25 with increasing the q' . However, the post-cracked stiffness in terms of normalized moment-curvature relationship increases from 0.2 to 0.5 to 0.8 with increasing the m' from 1.2 to 1.5 to 1.8 and the fixed $q'=0$.



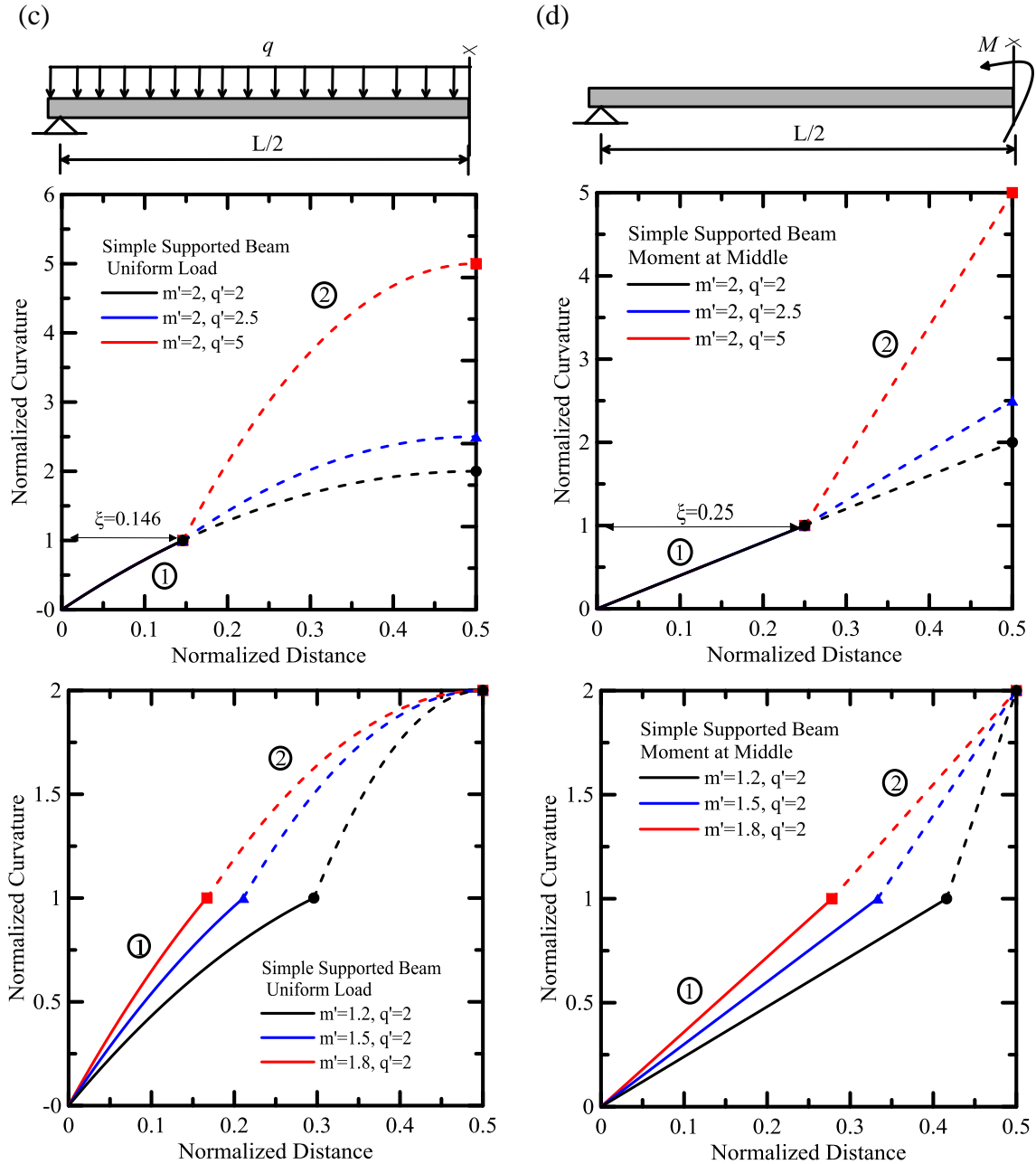
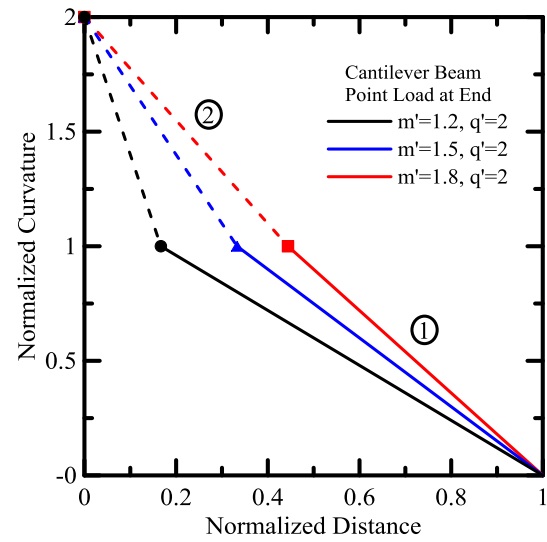
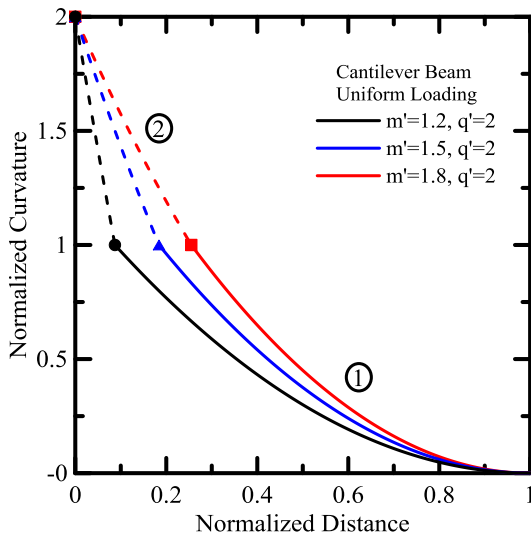
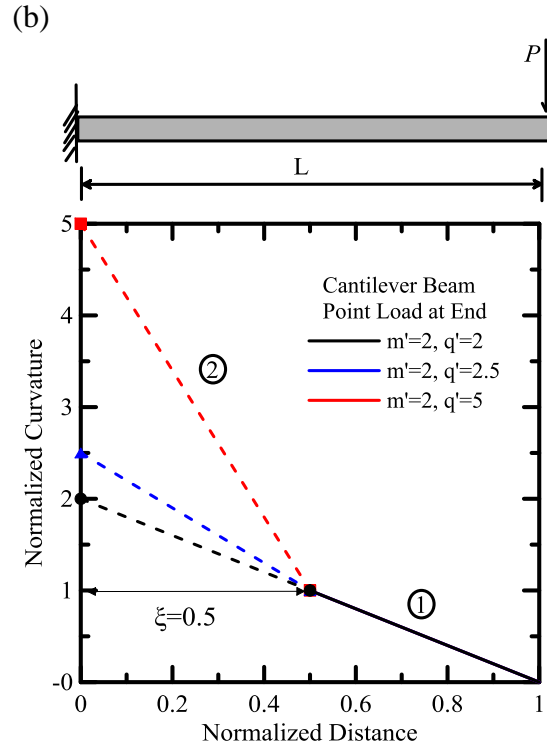
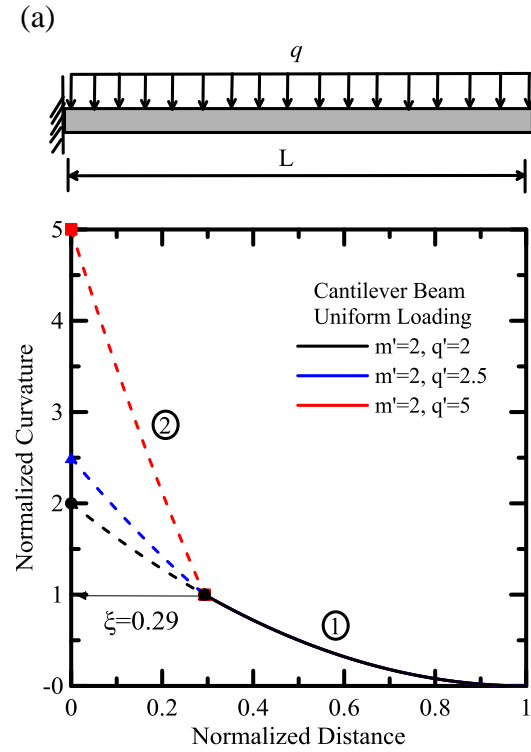


Figure 2.4.1 - Effects of m' and q' on Normalized Curvature Distribution for Simply Supported Beam; (a) 3PB; (b) 4PB; (c) Uniform Loading; (d) Moment at the Middle



(c)

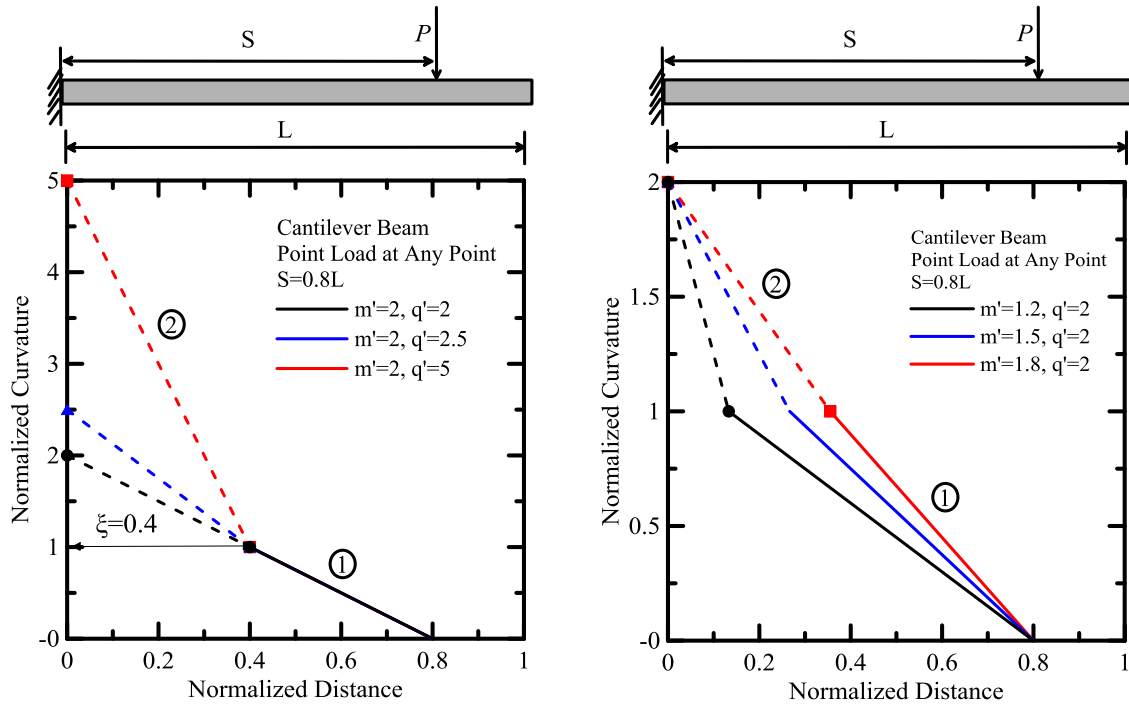


Figure 2.4.2 - Effects of m' and q' on Normalized Curvature Distribution for Cantilever Beam; (a) Uniform Loading; (b) Concentrated Load at Free End; (c) Concentrated Load with Distance S from Fixed End

2.4.2 Deflection Coefficient Distribution

Assume the length of beam is unit length which is equal to one ($L=1$) and choose the three levels of normalized moment m' equal to 1.2, 1.5 and 1.8 with a constant normalized curvature $q'=2$ or choose the three levels of normalized curvature q' equal to 2, 2.5, 5 with a constant normalized moment $m'=2$, the deflection coefficient equations can be obtained by substituting one pair of parameters and unit length of beam in the equations calculated in Section 2.3 for different types of beam. The derivation of deflection coefficient equations for three-point bending beam is presented here.

Re-call the deflection coefficient equations of three-point bending:

$$\delta_{21}^* = \frac{x^3}{6L^2\xi} - \frac{(L + Lq' - 2q'\xi)x}{4L^2} \quad 0 \leq x \leq \xi \quad (2.4.1.6)$$

$$\delta_{22}^* = \frac{1}{L - 2\xi} \left(\frac{(q' - 1)x^3}{3L^2} + \frac{(L - 2q'\xi)x^2}{2L^2} + \frac{x(4q'\xi - L - Lq')}{4L} + \frac{(L\xi^2 - 2q'\xi^3)}{6L^2} \right) \quad \xi \leq x \leq \frac{L}{2} \quad (2.4.1.7)$$

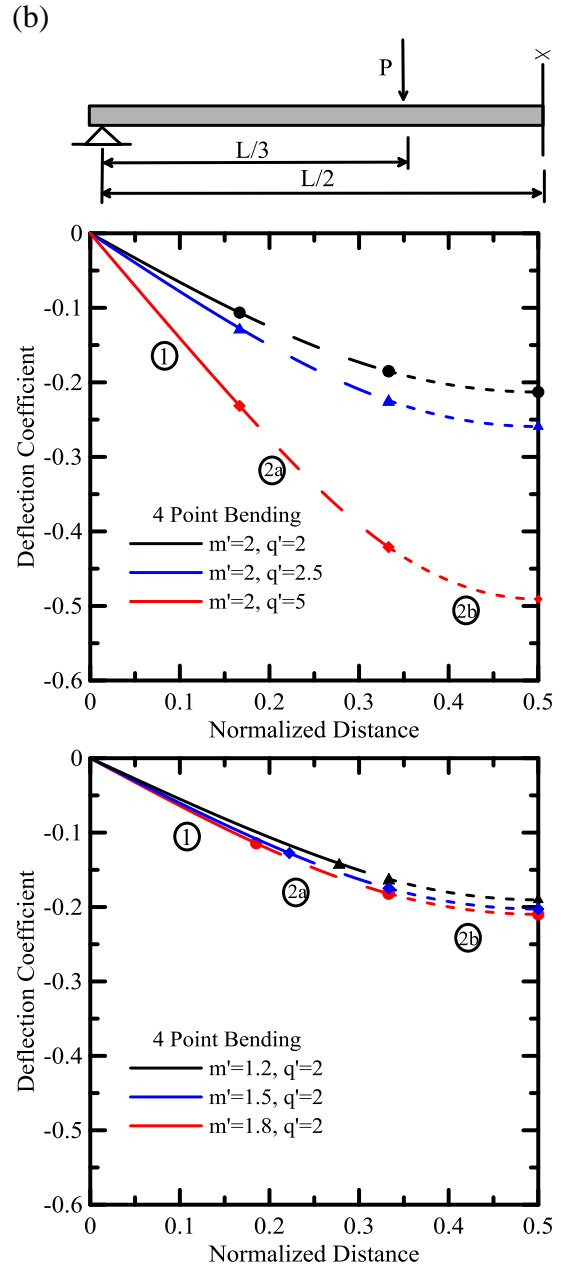
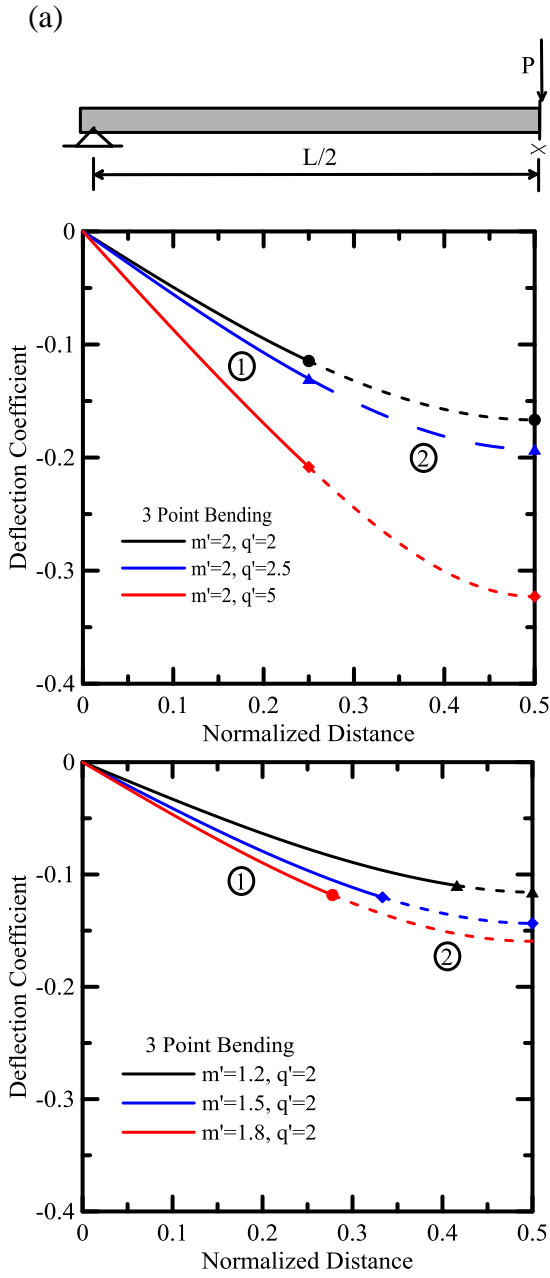
Using the same procedure with the derivation of normalized curvature distribution discussed in Section 2.4.1. Table 2.4.3 and 2.4.4 shows the deflection coefficient equations after substituting the parameters. Figure 2.4.3 shows the effects of m' and q' on deflection distributions for simply supported beam with different loading cases. Figure 2.4.4 shows the effects of m' and q' on deflection distribution for cantilever beam with different loading cases.

Table 2.4.3 - Deflection Coefficient Equations with Constant m' for 3PB Beam

| m' | ξ | q' | Deflection coefficient equation | |
|------|-------|------|---------------------------------|-------------------------------------|
| | | | δ_{21} | δ_{22} |
| 2 | 0.25 | 2 | $0.67x^3 - 0.5x$ | $0.67x^3 - 0.5x$ |
| 2 | 0.25 | 2.5 | $0.67x^3 - 0.56x$ | $x^3 - 0.25x^2 - 0.5x - 0.005$ |
| 2 | 0.25 | 5 | $0.67x^3 - 0.88x$ | $1.33x^3 - 0.75x^2 - 0.25x - 0.016$ |

Table 2.4.4 - Deflection Coefficient Equations with Constant q' for 3PB Beam

| m' | ξ | q' | Deflection coefficient equation | |
|------|-------|------|---------------------------------|---------------------------------------|
| | | | δ_{21} | δ_{22} |
| 1.2 | 0.42 | 2 | $0.4x^3 - 0.33x$ | $2x^3 - 2x^2 + 0.5x - 0.116$ |
| 1.5 | 0.33 | 2 | $0.5x^3 - 0.417x$ | $x^3 - 0.5x^2 - 0.25x - 0.018$ |
| 1.8 | 0.27 | 2 | $0.6x^3 - 0.472x$ | $0.75x^3 - 0.125x^2 - 0.437x - 0.003$ |



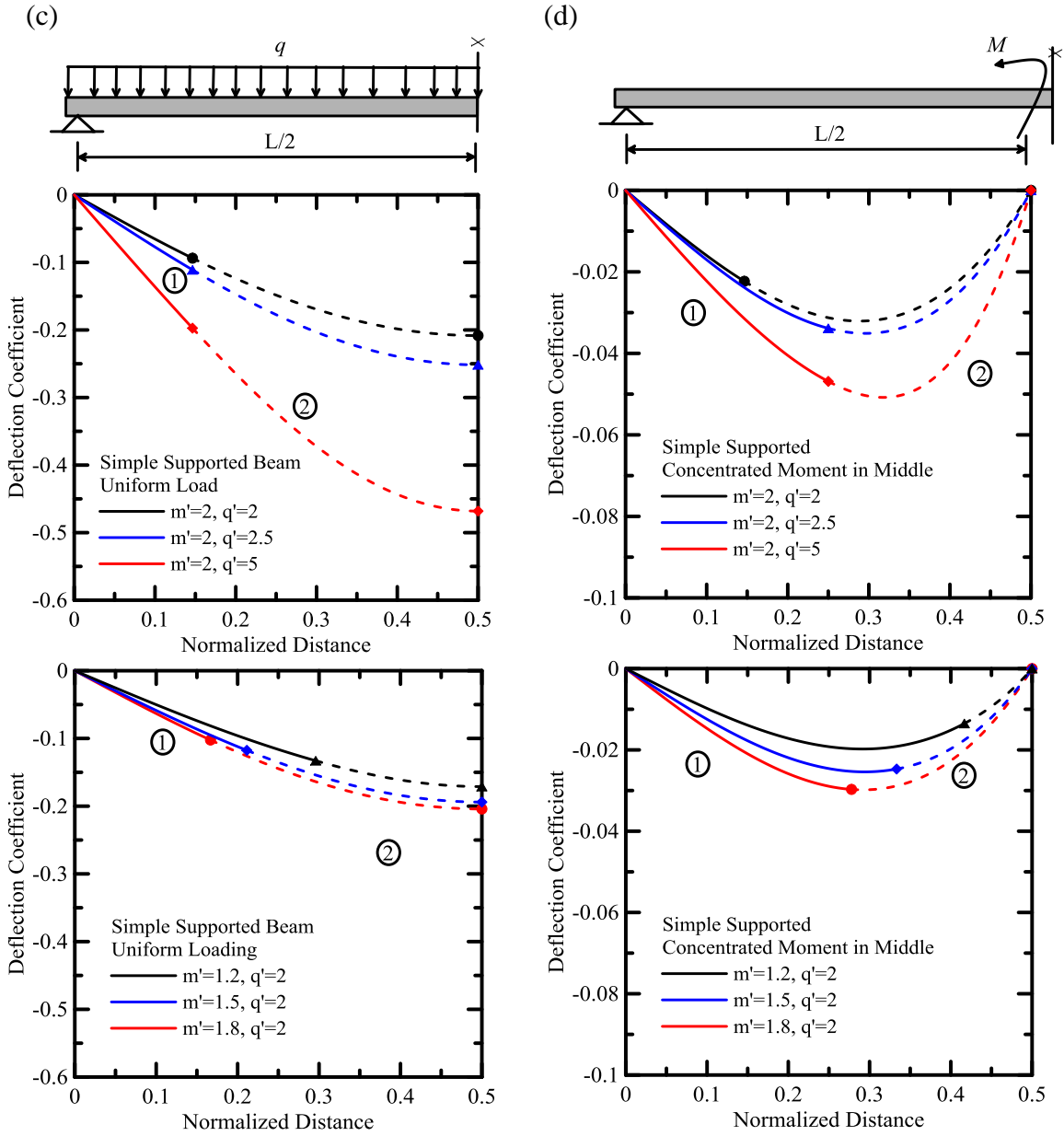
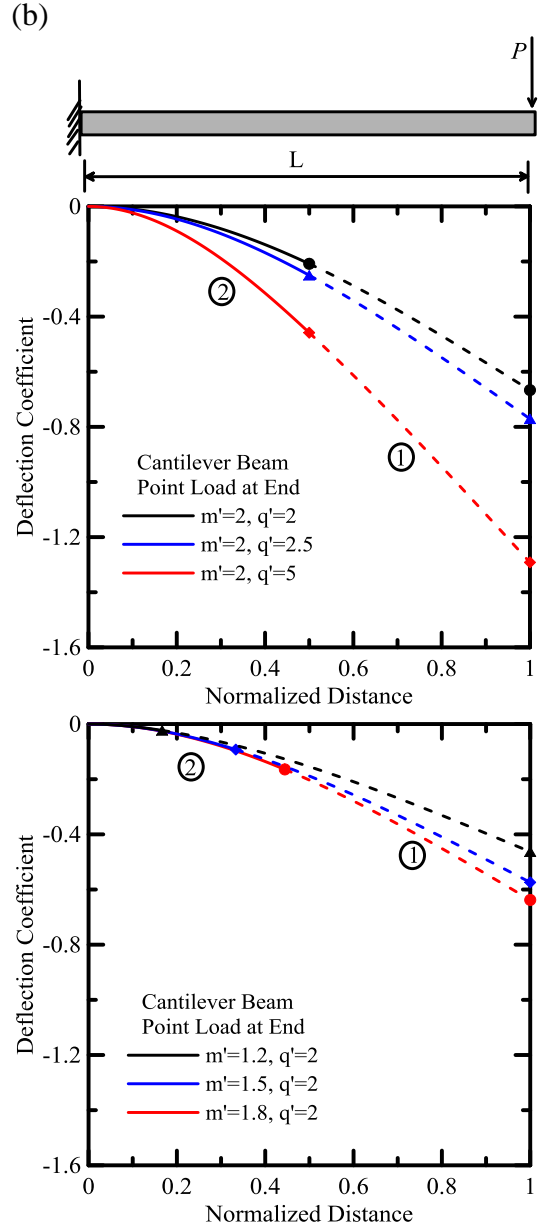
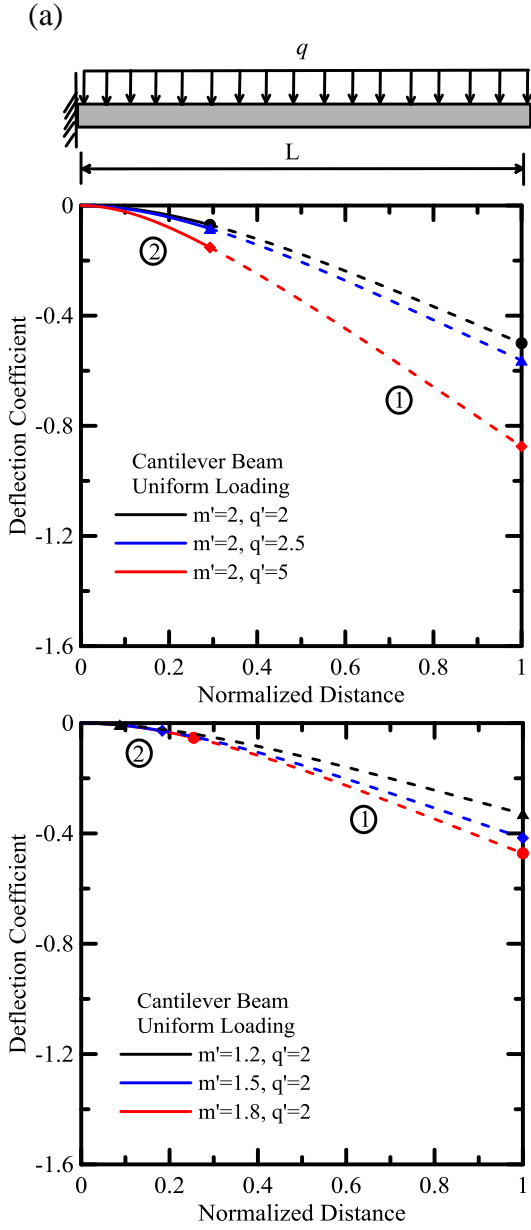


Figure 2.4.3 - Effects of m' and q' on Deflection Distribution for Simply Supported Beam; (a) 3PB; (b) 4PB; (c) Uniform Loading; (d) Moment at the Middle



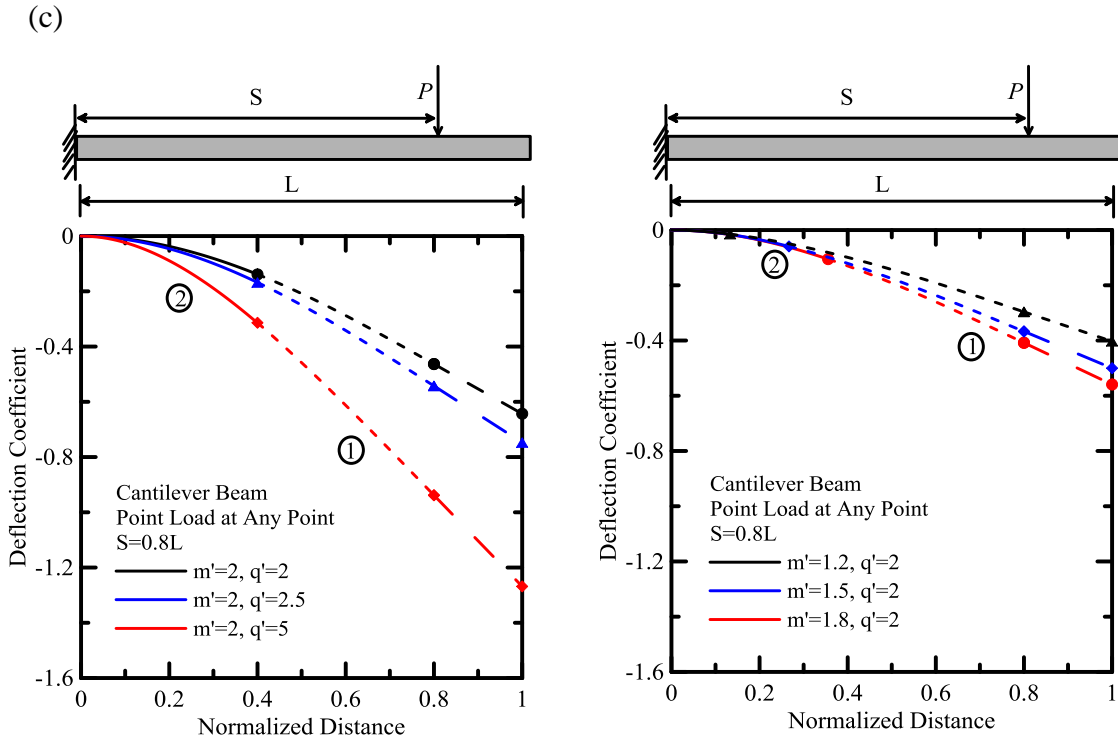


Figure 2.4.4 - Effects of m' and q' on Deflection Distribution for Cantilever Beam; (a) Uniform Loading; (b) Concentrated Load at Free End; (c) Concentrated Load with Distance S from Fixed End

2.4.3 2-D Contour

The deflection distributions for different loading types presented in Section 2.4.2 shows the deflection with the any cross-section of the beam for a certain magnitude of loading. In this section, 2-D deflection contours are shown in here for demonstrating the tendency of deflection distribution along the beam with increasing the magnitude of load from zero to the final stage. Implement the simplified bilinear moment-curvature relationship (Section 2.1) as the input, deflection can be calculated by using the equation derived in Section 2.3. In this procedure, the cracking moment and cracking curvature firstly to be calculated and then behaviour (pre-cracked or post-creaked) of any cross-section of beam under a certain magnitude of load can be verified. 2-D contours of three-point bending

and four-point bending beam are shown here. The assumed dimension of specimen and the material properties used in here is list in Table 2.4.5. Figure 2.4.5 and Figure 2.4.6 shows the 2-D deflection contours respect with the locations along the beam and applied load under the three and four-point bending tests, respectively. The parameter $\eta = EI_{cr}/EI_g$. Instead of the continuous variables, the levels of loading and the positions along the beam as the variables are evaluated the response of deflection as shown in Figure 2.4.7 and 2.4.8 based on the dimensions and parameters of Table 2.4.5. Note that the transition point from pre-cracked behavior to post- cracked behavior can be easily observed from Figure 2.4.7(a) and Figure 2.4.8(a). In the certain cross-section, the deflection increases with increasing the load and the deflection increases rapidly after first cracking point. It means the post-stiffness decreases after first cracking point.

Table 2.4.5- Parameters of 2-D Deflection Distribution

| Loading type | Span (L),mm | Width (b),mm | Height (d),mm | ϵ_{cr} , μstr | E, Mpa | η |
|--------------|-------------|--------------|---------------|-----------------------------------|--------|--------|
| 3PB | 300 | 100 | 100 | 244 | 20400 | 0.01 |
| 4PB | 750 | 100 | 100 | 244 | 20400 | 0.01 |

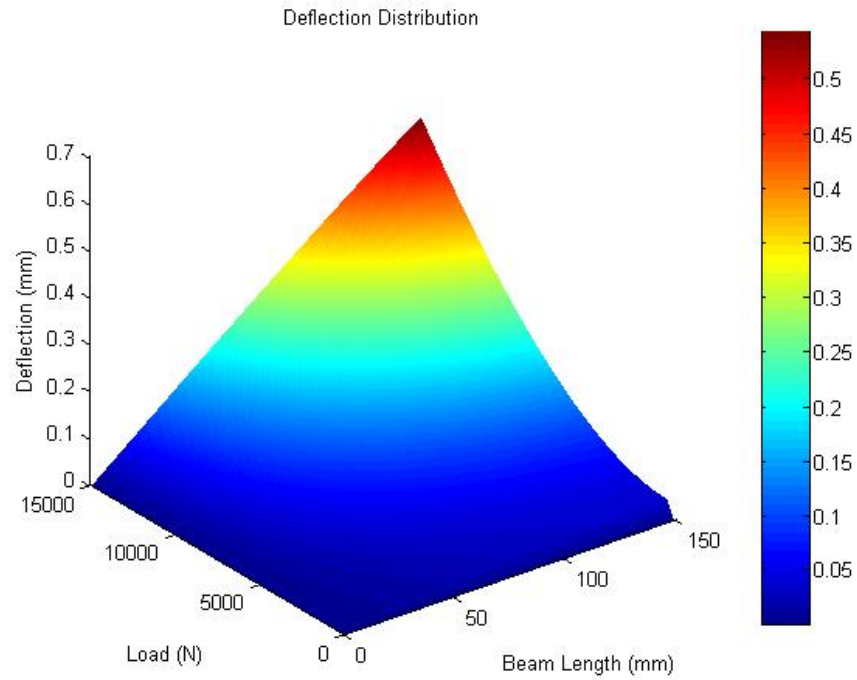


Figure 2.4.5 - 2-D Deflection Distribution of Three-Point Bending

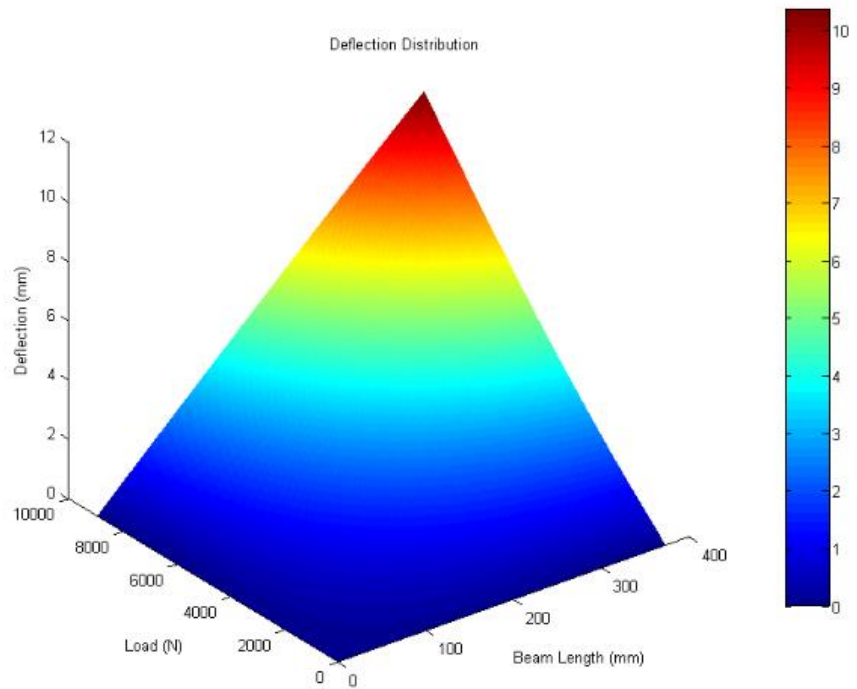


Figure 2.4.6 - 2-D Deflection Distribution of Four-Point Bending

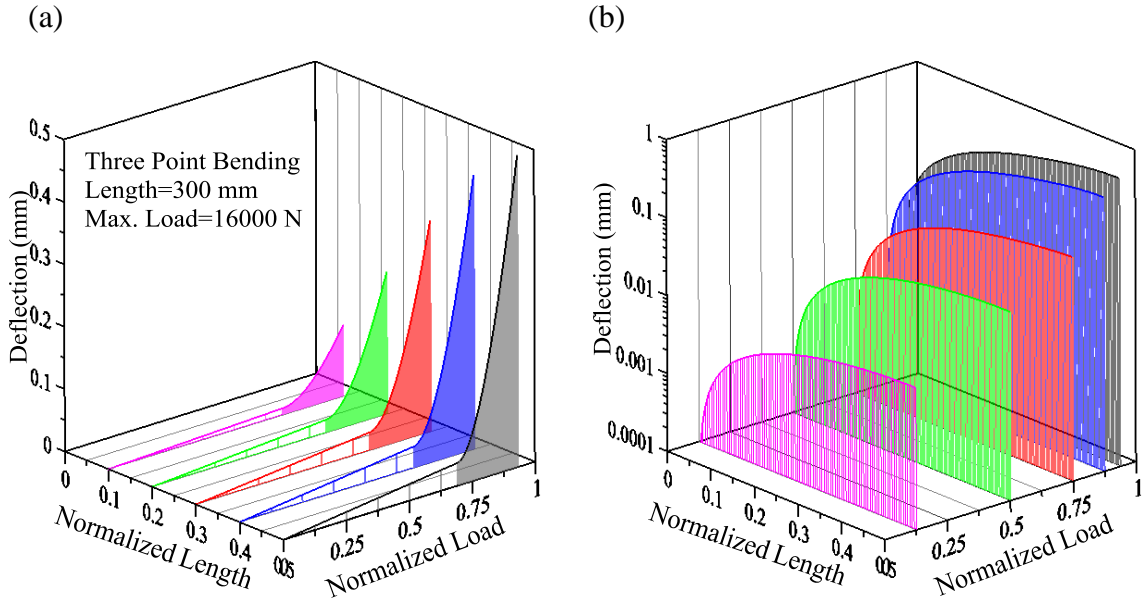


Figure 2.4.7 - Deflection Distributions of Three- Point Bending; (a) Different Locations along the Beam; (b) Different Loading Levels.

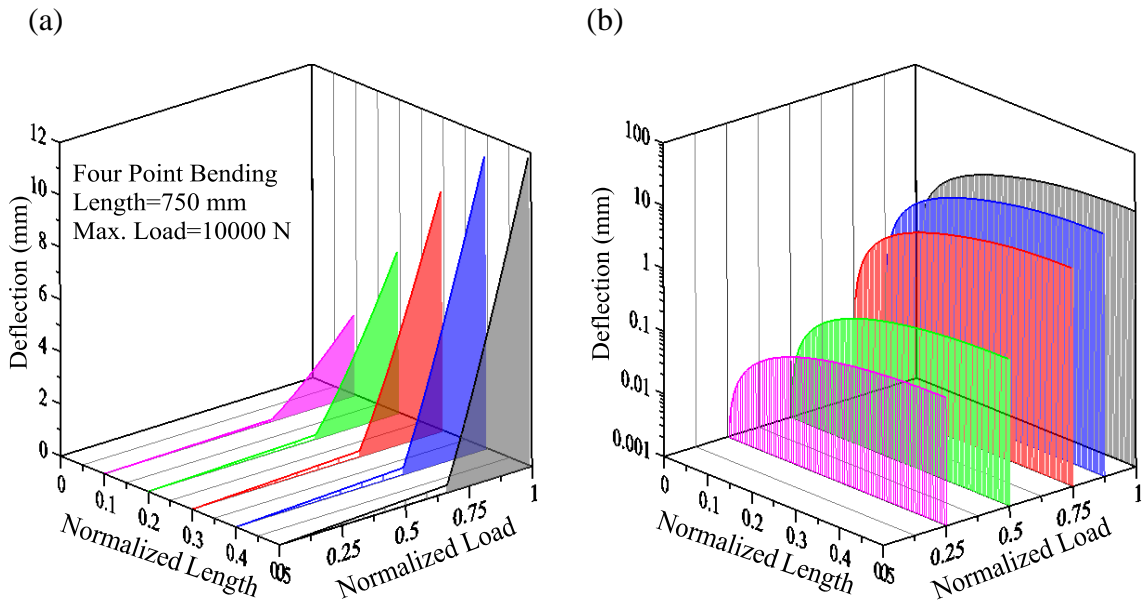


Figure 2.4.8 - Deflection Distributions of Four- Point Bending; (a) Different Locations along the Beam; (b) Different Loading Levels.

2.5 Experimental Verification

2.5.1 Algorithm to Predict Load Deflection Response

For the given dimensions of specimen including span, height and width and a set of material parameters E , ϵ_{cr} and η . The cracking moment and curvature M_{cr} , ϕ_{cr} are calculated from Eqs. (2.1.3) and (2.1.4), respectively. Deflection of beams with different regions is calculated by multiplying $\phi_{cr}L^2$ with simplified deflection coefficient equations specified in Table 2.3.1 to 2.3.8. The procedure of prediction of load deflection response follows the approach of curvature control, which means increasing normalized curvature q' from 0 to an assumed value which is corresponding to maximum load with a constant interval. Corresponding curvature ϕ' is calculated from Eq. (2.1.7) and relative moment M' can be obtained from the relationship of moment-curvature either in pre-cracking or post cracking stage. The load P' can be calculated from moment M' once the loading type known. Predicting the mid-span deflection by substituting $x=2/L$ in deflection coefficient equations, $\delta_{elastic}^*$ is applied for prediction when $q' \leq 1$ and only δ_{22}^* is used when $q' \geq 1$ since the point of $x=2/L$ is post-cracking region. Figure 2.5.1 shows the algorithm of predicting load-deflection response.

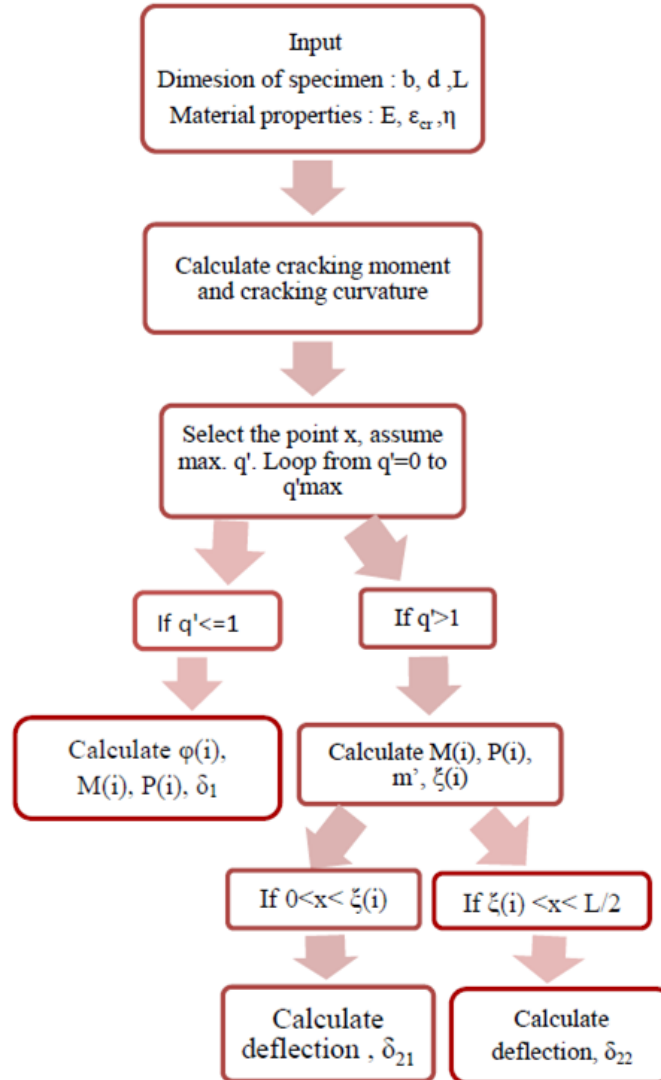


Figure 2.5.1 - Flow Chart of Prediction of Load-Deflection Response

2.5.2 Data Set 1

Experimental results of flexural tests of laminated Textile Reinforced Concrete (TRC) composites with alkali resistant (AR) glass, carbon, aramid, polypropylene textile fabrics, and a hybrid reinforcing system with aramid and polypropylene are presented by Mobasher, Barzin, et al.[23]. Three sets of experimental data from three-point bending tests are selected to simulate by implementing the proposed algorithm. The span is 220

mm with the rectangular cross section of width of 30 mm and height of 9 mm. Two of them are plain single fiber type composites made with both high and low modulus textiles and one of them is hybrid composite with these two type of textile. Aramid (A) were used as the high strength system and polypropylene (PP) were selected as low strength system as shown in Table 2.5.1. The volume fractions of reinforcement for these three sets of data are shown in Table 2.5.2. The normalized moment-curvature relationships and load-deflection responses of the three series were simulated by the algorithm proposed as shown in Figure 2.5.2 and Figure 2.5.3, respectively. The model parameters were obtained and summarized in Table 2.5.3.

Table 2.5.1 - Properties of Yarns Made up the Fabrics for Data Set 1

| Yarn type | Yarn nature | Strength (MPa) | Young's Modulus (MPa) | Filament size (mm) | Bundle diameter (mm) |
|-----------|-------------|----------------|-----------------------|--------------------|----------------------|
| PP | Bundle | 500 | 6900 | 0.040 | 0.40 |
| Aramid | Bundle | 2370 | 55000 | 0.012 | 0.38 |

Table 2.5.2- Volume Fraction (V_f) of Reinforcement for Data Set 1

| Specimen Code | | V_f % | PP | A |
|---------------|---------|---------|------|------|
| 100A | Average | 1.29 | | |
| | Std. | 0.06 | | |
| 100P | Average | 3.02 | | |
| | Std. | 0.09 | | |
| 25A75P | Average | 2.58 | 0.34 | 2.24 |
| | Std. | 0.07 | 0.01 | 0.06 |

Table 2.5.3 (a) - Simulated Parameters of 100A

| ID | $\frac{\epsilon_{cr},}{\mu\text{str}}$ | $\frac{E}{\text{GPa}}$ | η | m | q | $\frac{Mcr,}{KN-mm}$ | $\frac{\Phi cr,}{10^5/mm}$ | $EI, 10^7$ | $EI_{cr}, 10^6$ |
|--------|--|------------------------|--------|------|-------|----------------------|----------------------------|------------|-----------------|
| 100A-1 | 130 | 22 | 0.09 | 13.3 | 135 | 1158 | 2.89 | 4.0 | 3.7 |
| 100A-2 | 130 | 22 | 0.08 | 14.5 | 160 | 1158 | 2.89 | 4.0 | 3.4 |
| 100A-3 | 130 | 22 | 0.11 | 18.5 | 160 | 1158 | 2.89 | 4.0 | 4.4 |
| 100A-4 | 130 | 22 | 0.11 | 18.5 | 160 | 1158 | 2.89 | 4.0 | 4.4 |
| 100A-5 | 130 | 22 | 0.12 | 20.2 | 168 | 1158 | 2.89 | 4.0 | 4.6 |
| Avg. | 130 | 22 | 0.10 | 17.0 | 157 | 1158 | 2.89 | 4.0 | 4.1 |
| STD.DV | 0.0 | 0.0 | 0.01 | 2.93 | 12.56 | 0.00 | 0.00 | 0.0 | 5.2 |

Table 2.5.3(b) - Simulated Parameters of 100P

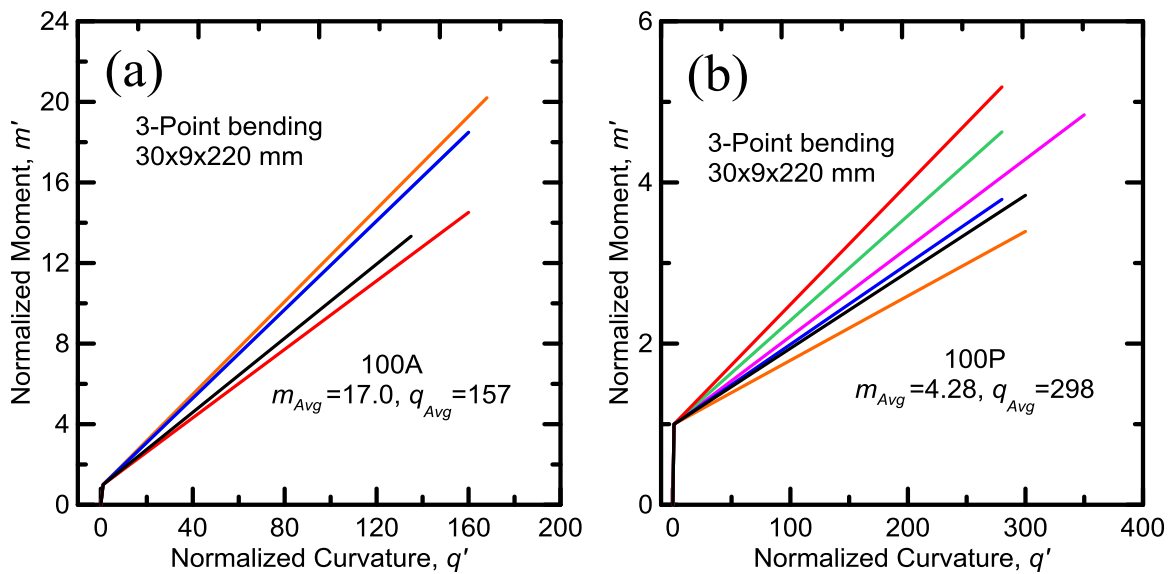
| ID | $\frac{\epsilon_{cr},}{\mu\text{str}}$ | $\frac{E}{\text{GPa}}$ | η | m | q | $\frac{Mcr,}{KN-mm}$ | $\frac{\Phi cr,}{10^5/mm}$ | $EI, 10^7$ | $EI_{cr}, 10^5$ |
|--------|--|------------------------|--------|------|-------|----------------------|----------------------------|------------|-----------------|
| 100P-1 | 130 | 22 | 0.01 | 3.84 | 300 | 1158 | 2.89 | 4.0 | 3.8 |
| 100P-2 | 130 | 22 | 0.015 | 5.19 | 280 | 1158 | 2.89 | 4.0 | 6.0 |
| 100P-3 | 130 | 22 | 0.01 | 3.79 | 280 | 1158 | 2.89 | 4.0 | 4.0 |
| 100P-4 | 130 | 22 | 0.013 | 4.63 | 280 | 1158 | 2.89 | 4.0 | 5.2 |
| 100P-5 | 130 | 22 | 0.008 | 3.39 | 300 | 1158 | 2.89 | 4.1 | 3.2 |
| 100P-6 | 130 | 22 | 0.011 | 4.84 | 350 | 1158 | 2.89 | 4.1 | 4.4 |
| Avg. | 130 | 22 | 0.01 | 4.28 | 298 | 1158 | 2.89 | 4.0 | 4.4 |
| STD.DV | 0.0 | 0.0 | 0.00 | 0.70 | 27.14 | 0.00 | 0.00 | 0.0 | 1.0 |

Table 2.5.3(c) - Simulated Parameters of 25A75P

| ID | $\frac{\epsilon_{cr},}{\mu\text{str}}$ | $\frac{E}{\text{GPa}}$ | η | m | q | $\frac{Mcr,}{KN-mm}$ | $\frac{\Phi cr,}{10^5/mm}$ | $EI, 10^7$ | $EI_{cr}, 10^6$ |
|----------|--|------------------------|--------|-------|--------|----------------------|----------------------------|------------|-----------------|
| 25A75P-1 | 130 | 22 | 0.05 | 11.5 | 230 | 1158 | 2.89 | 4.0 | 1.84 |
| 25A75P-2 | 130 | 22 | 0.05 | 11.5 | 230 | 1158 | 2.89 | 4.0 | 1.84 |
| 25A75P-3 | 130 | 22 | 0.02 | 6.98 | 240 | 1158 | 2.89 | 4.0 | 1.00 |
| 25A75P-4 | 130 | 22 | 0.09 | 15.0 | 160 | 1158 | 2.89 | 4.0 | 3.53 |
| 25A75P-5 | 130 | 22 | 0.04 | 8.10 | 170 | 1158 | 2.89 | 4.0 | 1.68 |
| 25A75P-6 | 130 | 22 | 0.06 | 9.74 | 160 | 1158 | 2.89 | 4.0 | 2.21 |
| AVE | 130 | 22 | 0.05 | 10.48 | 198.33 | 1158 | 2.89 | 4.0 | 2.02 |
| STD.DV | 0.0 | 0.0 | 0.02 | 2.87 | 38.69 | 0.00 | 0.00 | 0.0 | 8.39 |

Figure 2.5.2 shows the normalized moment-curvature relationships for the three sets of data. Note that composite made with high strength Aramid has highest ultimate

normalized moment $m = 17.0$, however the composite made with polypropylene has lowest ultimate normalized moment $m=4.18$. The ultimate normalized moment of hybrid composite is close to the average ultimate normalized moments of the two components. Figure 2.5.3 presented the simulated load-deflection responses for the three sets of experimental data. Comparing the stiffness ratio η in terms of moment-curvature relationship, η of 100P, 25A75P, 100A are increases from 0.011 to 0.05 to 0.102. With the similar pre-cracked behavior, it is obvious that the composite made with Aramid has highest post-cracked stiffness and the combination of low stiffness fibers in the presence of high stiffness fibers can improve the post-cracked stiffness.



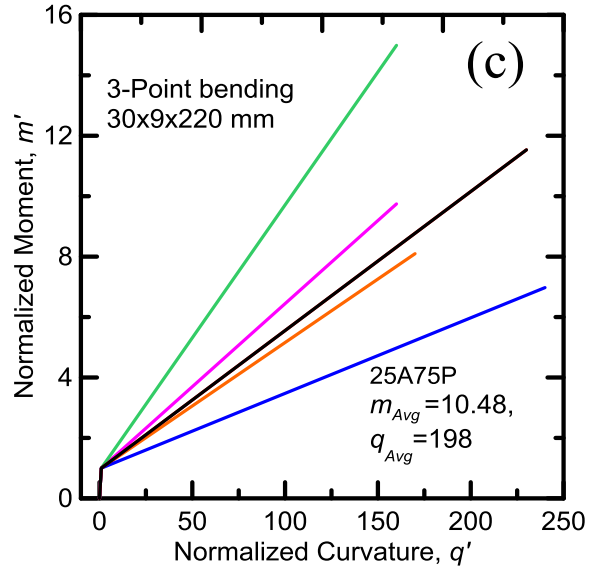
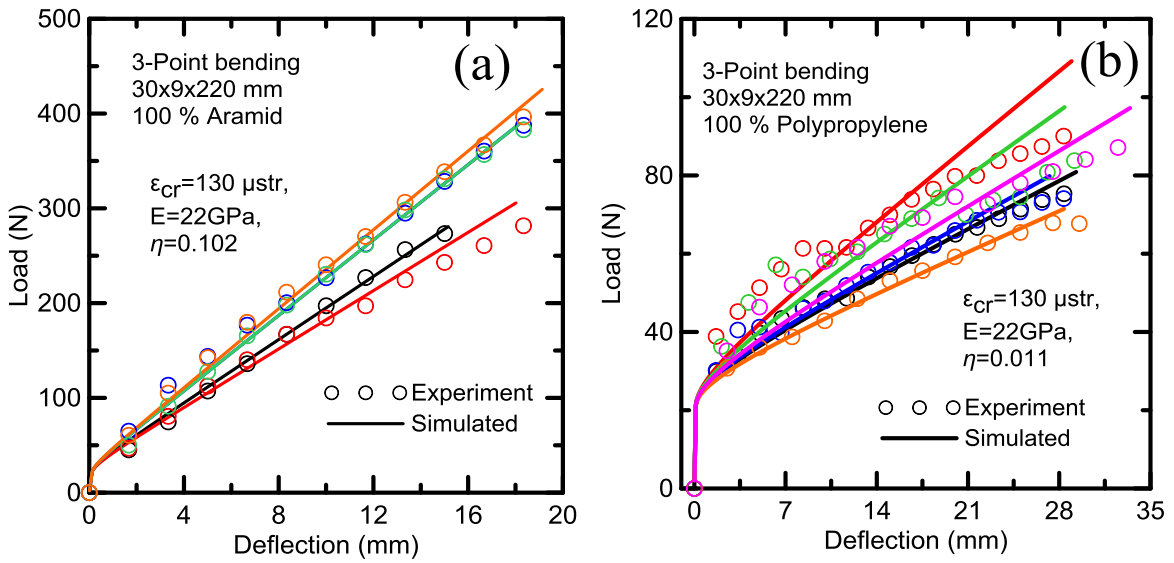


Figure 2.5.2 - Normalized Moment-Curvature Relationships; (a) 100A; (b) 100P; (c) 25A75P



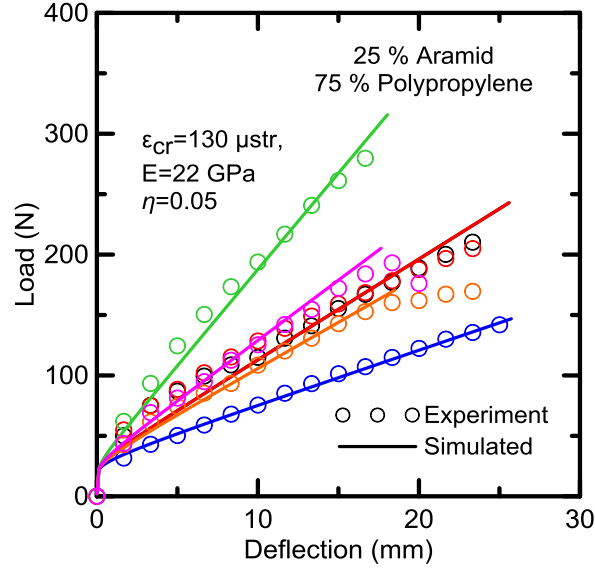


Figure 2.5.3 - Load-Deflection Responses ; (a) 100A; (b) 100P; (c) 25A75P

2.5.3 Data Set 2

Experimental data of six full scales FRC beams were tested under three point loading system are selected to demonstrate the algorithm for the load-deflection response [24]. The experimental program studied the effects of two variables: fiber dosage, dimension of beam. Beams were made with different amounts of steel fibres. 50 kg/m^3 and 75 kg/m^3 . For each fibre content, three beams with different depths were cast: 500 mm (specimen ID: H500), 1000 mm (H1000) and 1500 mm (H1500). All beams had the same width of 250 mm and distance between bottom fibre and rebar centroid of 60 mm. Table 4 summarizes all sample geometry details.

The load-deflection responses of the 6 beam series was simulated by the algorithm proposed. The parameters used in current model is Young's modulus E , first cracking tensile strain ϵ_{cr} and ratio of EI_{cr} to EI_g , η . Through adjusting these parameters between in a reasonable limitation, the experimental data were fitted as shown in Figure 2.5.5. The parameters used for current simulation are shown in Table 2.5.5. Figure 2.5.4 shows the

normalized moment-curvature diagram as the input for the simulated data for these 6 beams. Parameters m and q represents the normalized moment and normalized curvature of the ultimate stage respect to the experimental data.

Table 2.5.4 - Geometry Characteristics of Specimens

| Beams | H500 | H1000 | H1500 |
|--|--------------|--------------|--------------|
| Height (mm) | 500 | 1000 | 1500 |
| Effective depth (mm) | 440 | 940 | 1440 |
| Total length (mm) | 3000 | 5900 | 9000 |
| Span(mm) | 2640 | 5640 | 8640 |
| Width(mm) | 250 | 250 | 250 |
| Bottom to rebar centroid distance (mm) | 60 | 60 | 60 |
| Reinforcement longitudinal bars | 8- ϕ 14 | 8- ϕ 20 | 8- ϕ 24 |

Table 2.5.5 - Steel Fiber Reinforced Concrete Parameters for Current Model

| Beam Type | Fiber Content kg/m ³ | ϵ_{cr} , ustr | E GPa | η | m | q | EI | EI_{cr} |
|-----------|------------------------------------|---------------------------|----------|--------|------|-----|----------|-----------|
| H500 | 50 | 146 | 30.8 | 0.24 | 6.04 | 22 | 8.02E+13 | 1.93E+13 |
| | 75 | 120 | 31 | 0.26 | 9.32 | 33 | 8.07E+13 | 2.1E+13 |
| H1000 | 50 | 120 | 30 | 0.22 | 5.18 | 20 | 6.25E+14 | 1.38E+14 |
| | 75 | 120 | 31 | 0.28 | 6.88 | 22 | 6.46E+14 | 1.81E+14 |
| H1500 | 50 | 120 | 29 | 0.24 | 6.04 | 22 | 2.04E+15 | 4.89E+14 |
| | 75 | 120 | 30 | 0.28 | 7.16 | 23 | 2.11E+15 | 5.91E+14 |

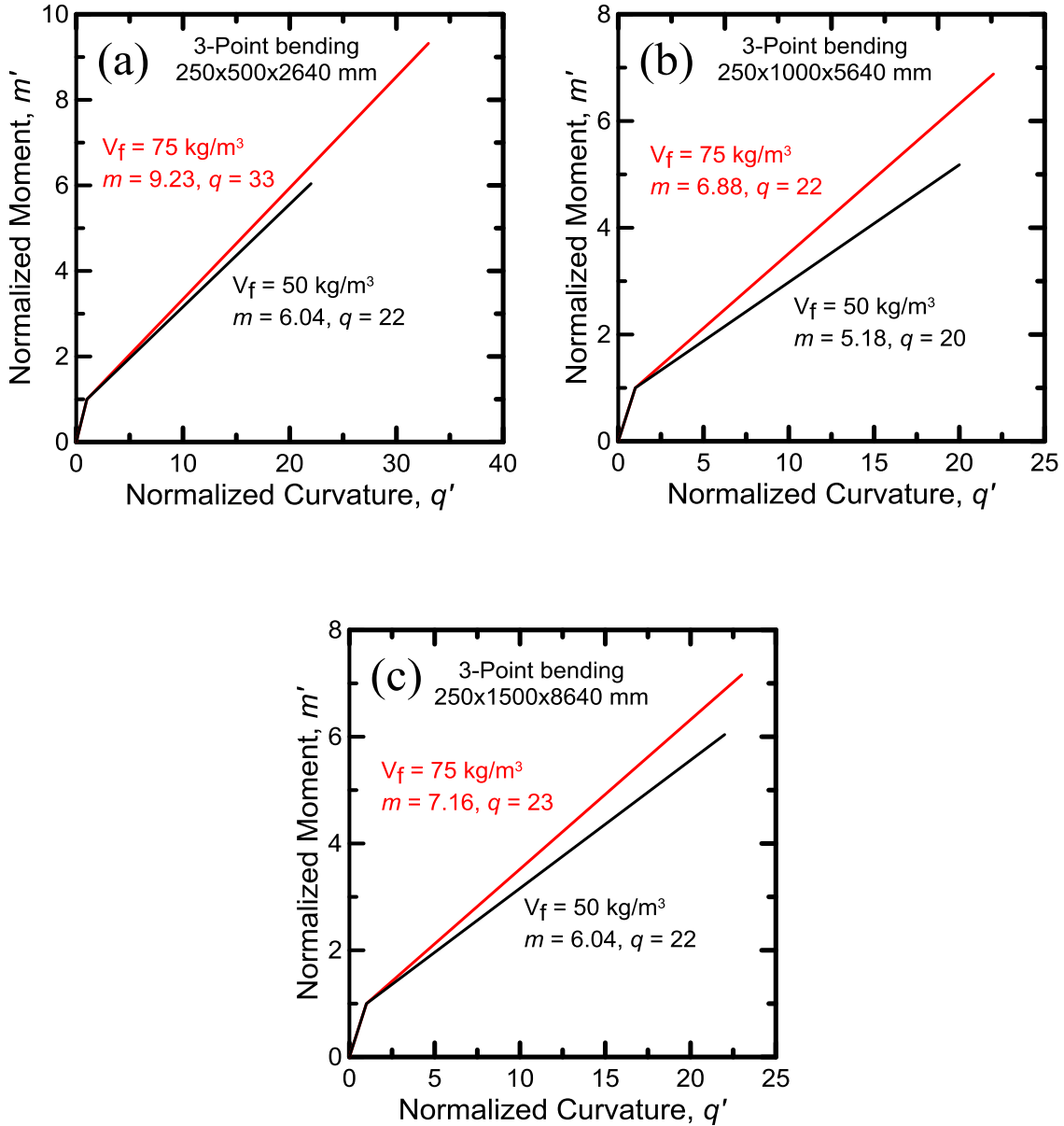
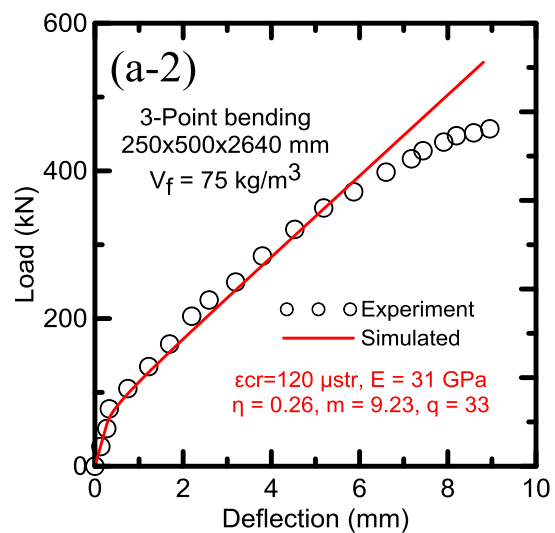
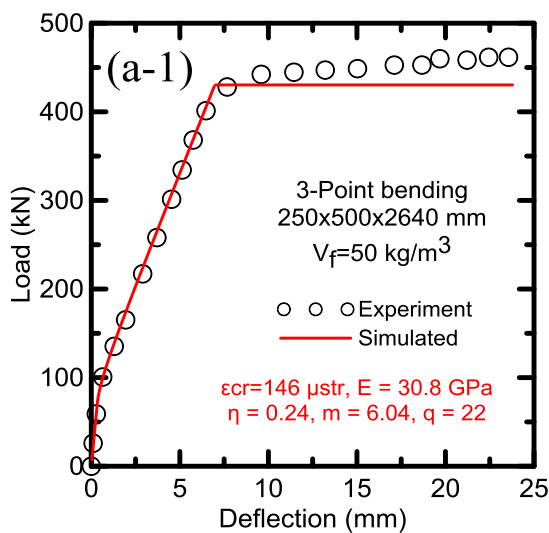


Figure 2.5.4 - Normalized Moment-Curvature Diagrams of Simulated Data; (a) H500; (b) H1000; (c) H1500

Figure 2.5.5 shows the simulation of the six beams representing the effect of fiber content and dimension of beam. The experimental response of each beam is compared to the simulation curve using the models parameters presented in Table 2.5.2. Note that the simulation of flexural load-deflection responses for H500 beams is generally accurate as

shown in Figure 2.5.3a. However, it is clearly that closed form deflection equation model slightly overestimates the experimental data for the initial linear portion of curve when the height of beam increased (Figure 2.5.3b and Figure 2.5.3c) It reveals the prediction slightly underpredicts the real deformation at portion of the beginning after the linear part but overestimates on the last portion of curve. This is attributed to the derivation of closed form deflection equations based on the simplified bilinear moment-curvature relationship which lead to the prediction of real deformation is biased and not perfectly matched.



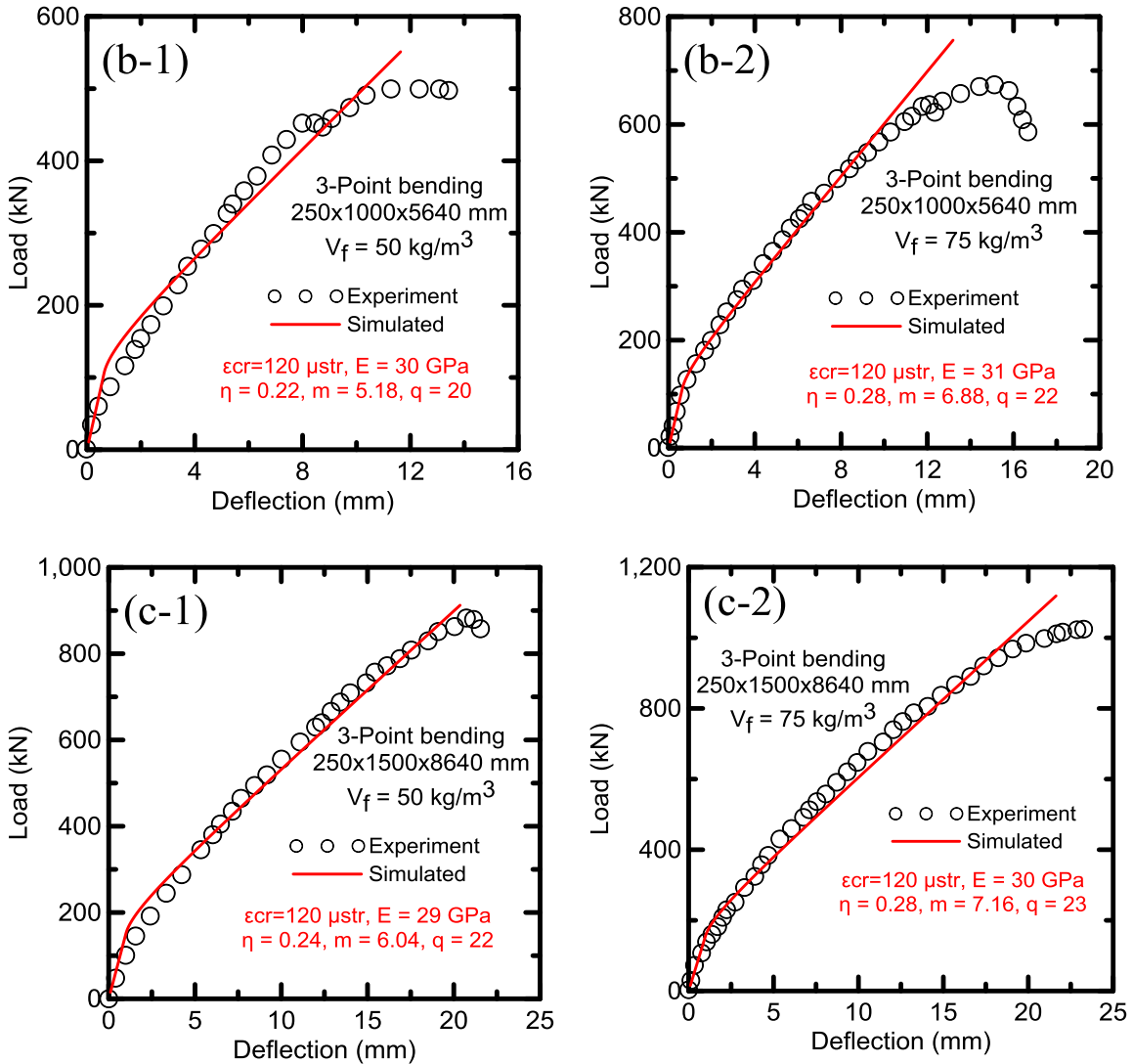


Figure 2.5.5 - Load Deflection Responses of FRC Beams at Two Levels of Fiber Contents (50 kg/m³ and 75 kg/m³)

2.5.4 Data Set 3

A total of eight rectangular reinforced concrete beams were investigated by Qu et al [25], named through B1 to B8. One reinforced with steel bars (B1), one reinforced with GFRP bars (B2), and six beams reinforced with a combination of steel and GFRP bars. The beams with rectangular cross section of 180 mm wide and 250 mm height and a span of

1.8m under a four-point bending test. Two steel bars of 10-mm diameter were used as reinforcement at the compression side. Steel stirrups with 10-mm diameter and 100-mm spacing were used as shear reinforcement. The details of the reinforced beam are shown in Table 2.5.6, where $A=A_s+A_f$ is the total area of reinforcement.

Table 2.5.6 – Details of Test Beam for Data Set 3

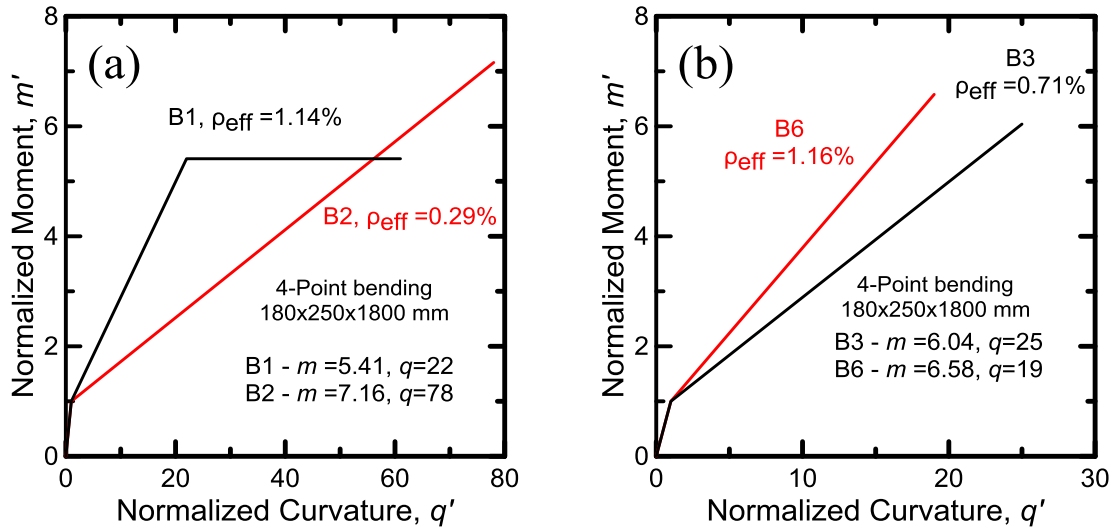
| Beam ID | A_s (mm ²) | A_f (mm ²) | A (mm ²) | ρ_{eff} (%) |
|---------|--------------------------|--------------------------|------------------------|------------------|
| B1 | 452.16 | - | 452.16 | 1.14 |
| B2 | - | 506.45 | 506.45 | 0.29 |
| B3 | 226.08 | 253.23 | 479.31 | 0.71 |
| B4 | 200.96 | 396.91 | 597.87 | 0.71 |
| B5 | 401.92 | 141.69 | 543.61 | 1.08 |
| B6 | 401.92 | 253.23 | 655.15 | 1.16 |
| B7 | 113.04 | 141.69 | 254.73 | 0.35 |
| B8 | 1205.76 | 396.91 | 1602.67 | 3.49 |

Table 2.5.7 - Simulated Parameters of Current Model for Data Set 3

| ID | ϵ_{cr} , 10 ⁻⁶ | E, GPa | η | m | q | M_{cr} , KN-mm | Φ_{cr} , 1/mm | EI | EI_{cr} |
|----|---------------------------------------|-----------|--------|-------|-----|---------------------|-----------------------|----------|-----------|
| B1 | 130 | 25 | 0.21 | 5.41 | 22 | 6094 | 1.04E-006 | 5.86E+12 | 1.23E+12 |
| B2 | 135 | 25 | 0.08 | 7.16 | 78 | 6328 | 1.08E-006 | 5.86E+12 | 4.69E+11 |
| B3 | 130 | 25 | 0.21 | 6.04 | 25 | 6094 | 1.04E-006 | 5.86E+12 | 1.23E+12 |
| B4 | 130 | 25 | 0.21 | 3.73 | 14 | 6094 | 1.04E-006 | 5.86E+12 | 1.23E+12 |
| B5 | 130 | 25 | 0.28 | 5.76 | 18 | 6094 | 1.04E-006 | 5.86E+12 | 1.64E+12 |
| B6 | 130 | 25 | 0.31 | 6.58 | 19 | 6094 | 1.04E-006 | 5.86E+12 | 1.82E+12 |
| B7 | 140 | 25.5 | 0.033 | 3.94 | 90 | 6694 | 1.12E-006 | 5.98E+12 | 1.97E+11 |
| B8 | 130 | 25 | 0.55 | 10.35 | 18 | 6094 | 1.04E-006 | 5.86E+12 | 3.22E+12 |

The proposed algorithm is implemented to predict the flexural responses of these tests. Figure 2.5.6 shows the normalized moment-curvature relationships of beam based on the simulated parameters (Table 2.5.7). Figure 2.5.6(a) shows the comparison of B1 and B2 and note that the post cracked stiffness in terms of moment- curvature response of B1 is

higher than B2 since the B1 is reinforced with steel bar and has a higher effective reinforcement ratio comparing with B2. The difference between B3 and B6 is that the B6 has more reinforced steel bar than that of B3. It is obvious that the post stiffness of B6 is higher than that of B3. The similar conclusions could be reached for comparing B4 with B8 and B5 with B7 (Figure 2.5.6(c), Figure 2.5.6(d)). The effect of reinforcement type and combination on the post cracked behavior also can be directly analysed by comparing the stiffness ratio η listed in Table 2.5.7. Figure 2.5.7 shows the predictions of load-deflection responses and it is clearly reveals that the proposed closed-form deflection equations can accurately simulate the flexural behavior of pre-cracked and post cracked stage. Use of steel reinforcement in combination with GFRP reinforcement enhances the flexural stiffness after the cracking.



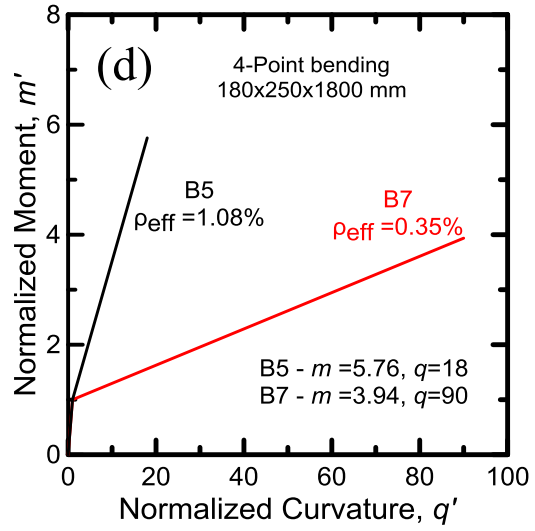
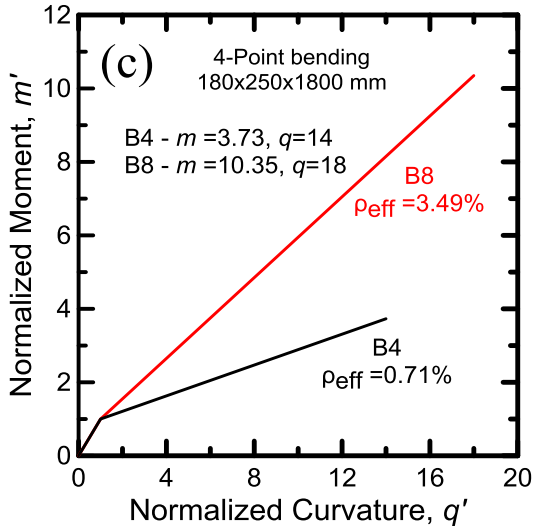
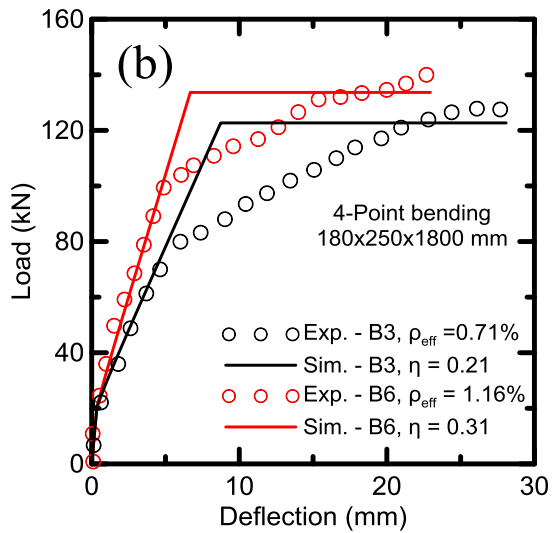
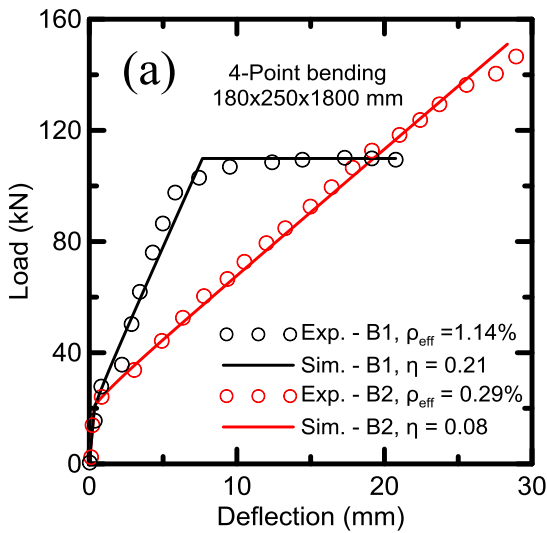


Figure 2.5.6 - Normalized Moment-Curvature Relationships;(a) B1,B2; (b) B3, B6; (c) B4, B8; (d)B5, B7



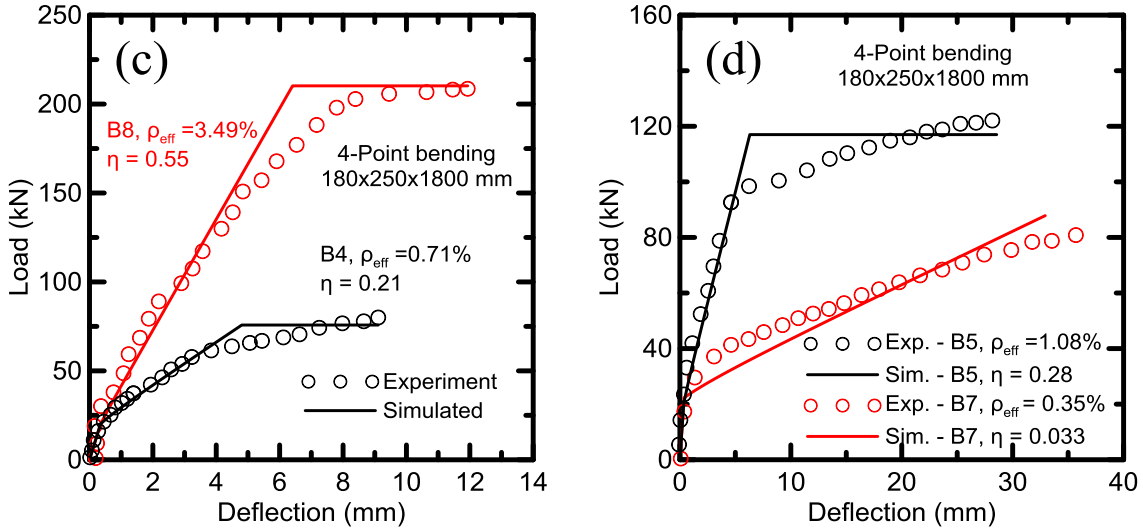


Figure 2.6.7 - Load-Deflection Responses ;(a) B1,B2; (b) B3, B6; (c) B4, B8; (d)B5, B7

2.5.5 Data Set 4

A total of nine rectangular RC beam with the dimension of $200 \times 600 \times 4000$ mm (bxdxL) were tested to study and compare the effect of hybrid internal reinforcements and shear reinforcement rebar by four-point bending tests, as shown in Figure 2.5.8. The details of the reinforcement with each beam are shown in Table 2.5.8.

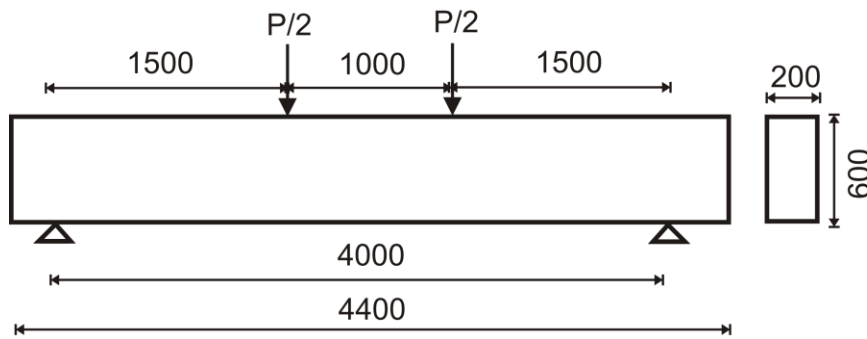


Figure 2.5.8 - Set up of four-point bending test (Unit: mm)

Table 2.5.8 - Details of Reinforced Beam

| Beam | Fiber volume fraction (%) | Longitudinal reinforcement | | | Shear reinforcement | |
|------|------------------------------------|----------------------------|---------|------------|------------------------|--------|
| | | Ratio (%) | Tension | Top bar | Ratio (%) | Rebars |
| V1 | 0 | 0.262 | 4φ10 | 2φ6.3 | 0.104 | 4φ6.3 |
| V2 | 0 | 0.262 | 4φ10 | 2φ6.3 | 0 | 0 |
| V3 | 0.75 | 0.052 | 2φ6.3 | 2φ6.3 | 0.052 | 2φ6.3 |
| V4 | 0.75 | 0.052 | 2φ6.3 | 2φ6.3 | 0 | 0 |
| V5 | 1 | 0.052 | 2φ6.3 | 2φ6.3 | 0 | 0 |
| V6 | 1.25 | 0.052 | 2φ6.3 | 2φ6.3 | 0 | 0 |
| V7 | 0.5 | 0.131 | 2φ10 | 2φ6.3 | 0 | 0 |
| V8 | 0.75 | 0.131 | 2φ10 | 2φ6.3 | 0 | 0 |
| V9 | 1.25 | 0.131 | 2φ10 | 2φ6.3 | 0 | 0 |

Implementing the procedure to predict the applied load and deflection of mid-span of beam, the parameters used in the simulation are presented in Table 2.5.9. Figure 2.4.9 to Figure 2.4.11 shows the normalized moment-curvature relationships and load-deflection responses with simulated parameters. Since the cement based mixture are same with these nine beam, the simulated first cracking strain and Young's modules just have slightly different with beam V4 and V9 compared with other beam which have the ϵ_{cr} is 160 μ str and E is 28 GPa.

From a conventional reinforcement point of view the effect of compression reinforcement as well as shear reinforcement can't be ignored. Figure 2.5.9 shows the responses of the beam V1 compared to beam V2. The difference between these two beams is that beam V1 has the additional shear reinforcement while the V2 only have the longitudinal reinforcement. Note that the combined effect of transverse and compression reinforcement is shown in ability of the rebar to hold in place and avoid the premature failure of the shear failure of the beam.

Note that stiffness ratio η of beam V2 is 0.07 which is smaller than that of beam V1, which means the post crack stiffness in the sample with transverse reinforcement is much higher than the sample without transverse reinforcement since the pre-cracking stiffness is same which is decided by the mixture. It is obvious that the yield load of beam V1 is 189 KN and normalized yield moment is 2.56, which are much higher than that of beam V2.

Table 2.5.9 - Simulated Parameters of Current Model for Data Set 4

| ID | $\epsilon_{cr}, 10^{-6}$ | E, GPa | η | m | q | $M_{cr}, KN-mm$ | $\Phi_{cr}, 10^{-7}/mm$ | $EI, 10^{14}$ | $EI_{cr} 10^{13}$ |
|----|--------------------------|--------|--------|------|------|-----------------|-------------------------|---------------|-------------------|
| V1 | 160 | 28 | 0.13 | 2.56 | 100 | 53760 | 5.33 | 1.01 | 1.31 |
| V2 | 160 | 28 | 0.07 | 1.91 | 92 | 53760 | 5.33 | 1.01 | 0.71 |
| V3 | 160 | 28 | 0.1 | 1.70 | 8 | 53760 | 5.33 | 1.01 | 1.01 |
| V4 | 155 | 28 | 0.065 | 1.36 | 6.5 | 52080 | 5.17 | 1.01 | 0.66 |
| V6 | 160 | 29 | 0.16 | 1.96 | 7.0 | 55680 | 5.33 | 1.04 | 1.67 |
| V7 | 160 | 28 | 0.09 | 1.58 | 7.5 | 53760 | 5.33 | 1.01 | 0.91 |
| V8 | 160 | 28 | 0.1 | 2.00 | 11.0 | 53760 | 5.33 | 1.01 | 1.01 |
| V9 | 165 | 29 | 0.13 | 2.23 | 10.5 | 57420 | 5.50 | 1.04 | 0.14 |

The Figure 2.5.10 shows the responses of the beam V2, V3, V4 and V6. The fiber content of beam V3 is 0.75% which is same as the beam V4, however, the fiber content of beam V6 is 1.25%. The beam V3 has both longitudinal reinforcement and shear reinforcement while the beam V4 and V6 only has the shear reinforcement. Comparing the load-deflection responses and the simulated parameters of beam V3 and V4, the post-creaked stiffness of beam V3 is much higher than the beam V4 since the effect of transverse reinforcement. The post creaked stiffness of beam V6 is also higher than the beam V3 since the effect of fiber content. Obviously, the yield load of beam V4 is lower than that of beam V3 and V6 and the yield load of beam V6 is much higher than that of V3 and V4.

Figure 2.5.11 shows the comparison between the samples V7, V8, and V9. Note that the difference between the three mixtures is expressed in the volume fraction of the fibers increasing from 0.5 to 0.75 and 1.25. Also note that the post cracking stiffness in terms of simulated moment-curvature diagram increases from 9.07×10^{12} to 1.01×10^{13} and 1.36×10^{13} .

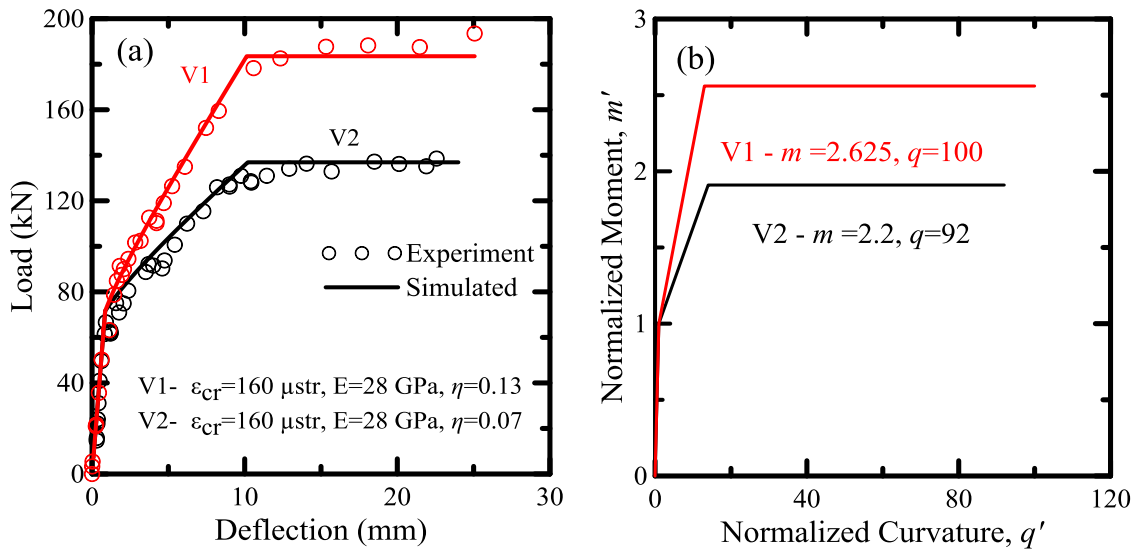


Figure 2.5.9 - (a) Load-Deflection Response of Beams V1, V2; (b) Simulated Normalized Moment-Curvature Relationship of Beams V1, V2

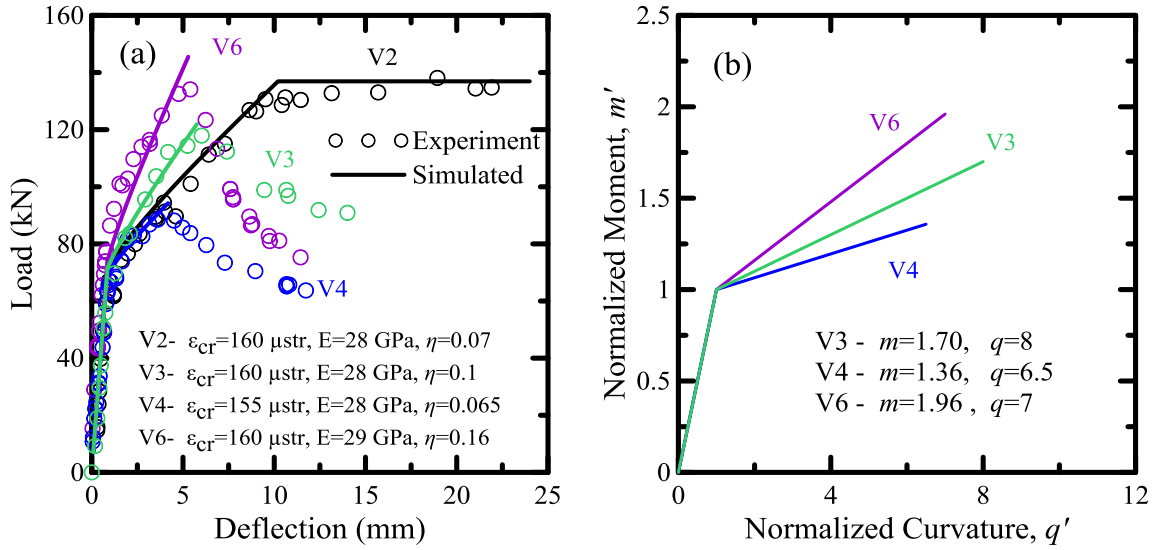


Figure 2.5.10 - (a) Load-Deflection Response of Beams V2, V3, V4, V6; (b) Simulated Normalized Moment-Curvature Relationship of Beams V2, V3, V4, V6

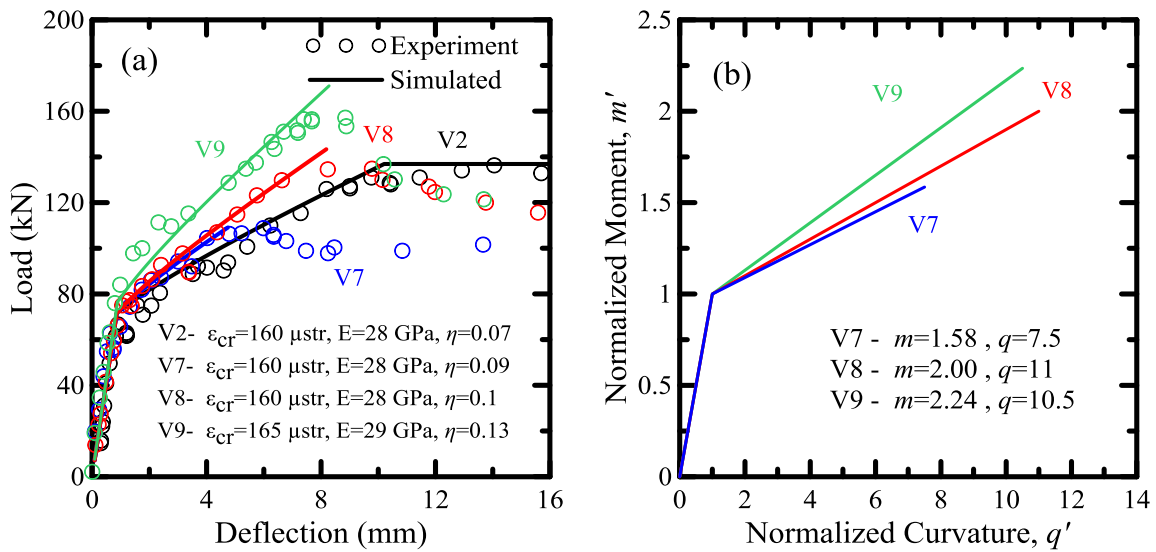


Figure 2.5.11 - (a) Load-deflection response of beams V2, V7, V8, V9; (b) Simulated normalized moment-curvature relationship of beams V2, V7, V8, V9

Comparison of the predictions with previous model

In order to verify and evaluate the accuracy of current model, the comparison with previous model is conducted here. Using the algorithm of strain-hardening material model which is discussed in Section 1.3, the predictions of load-deflection response and moment-curvature relationship were generated for this set of data and the simulated material parameters of previous model are shown in Table 2.5.10. Figure 2.5.12 to Figure 2.5.15 shows the comparisons of current model with previous model. Note that the parameter of first creaking strain ϵ_{cr} used in current model is $160 \mu\text{str}$ and the ϵ_{cr} of previous model is in the range of 125 to 150. The Young's modulus of current model is slightly lower than that of existed model. Since the current model is a simplified model based on the strain-hardening model (previous model), the predictions of load-deflection and moment-curvature responses with the both models are similar.

Table 2.5.10 - Parameters with Previous Model for Data Set 4

| Beam | Vf (%) | μ | Concrete | | | | | | Steel | | |
|------|--------|-------|----------|-----------------------------------|--------------|----------|----------------|----------|------------|-------------|----------------|
| | | | E (GPa) | ϵ_{cr} ($\mu\epsilon$) | β_{tu} | ω | λ_{cu} | γ | ρ (%) | E_s (GPa) | f_{sy} (MPa) |
| V1 | 0 | 0.10 | | 150 | | | | | 0.262 | | |
| V2 | 0 | 0.40 | | 150 | | | | | 0.262 | | |
| V3 | 0.75 | 0.65 | | 125 | | | | | 0.052 | | |
| V4 | 0.75 | 0.45 | | 125 | | | | | 0.052 | | |
| V6 | 1.25 | 0.60 | 30 | 125 | 50 | 5 | 12 | 0.9 | 0.052 | 210 | 500 |
| V7 | 0.5 | 0.35 | | 150 | | | | | 0.131 | | |
| V8 | 0.75 | 0.45 | | 150 | | | | | 0.131 | | |
| V9 | 1.25 | 0.65 | | 150 | | | | | 0.131 | | |

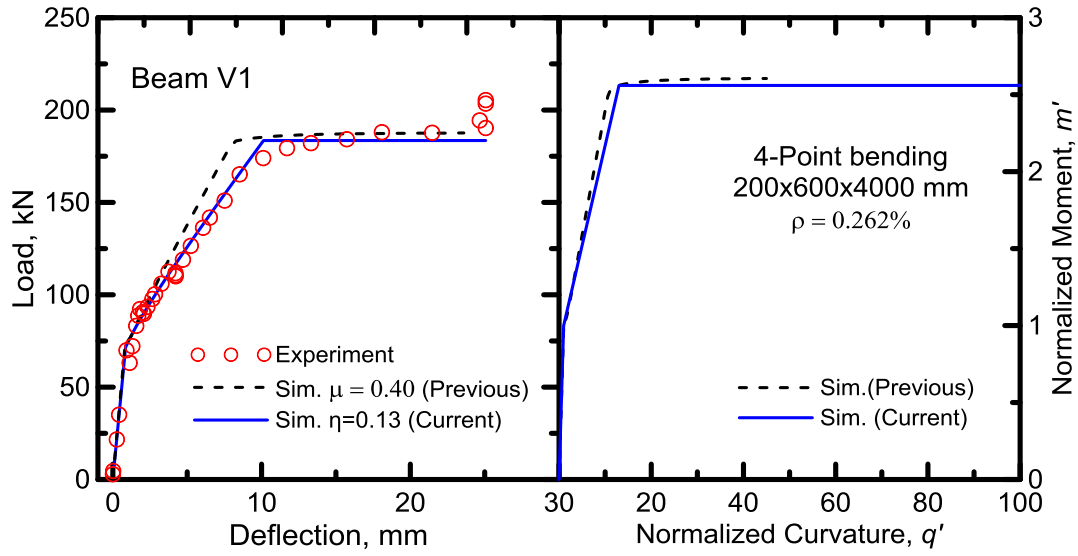


Figure 2.5.12 - Comparison of Current Model with Previous Model for Beam V1

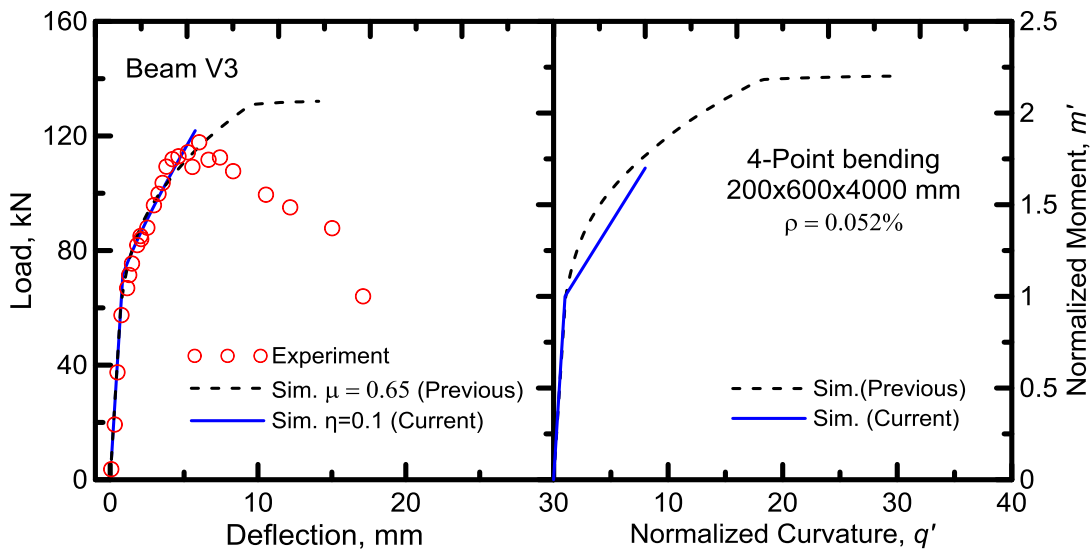


Figure 2.5.13 - Comparison of Current Model with Previous Model for Beam V3

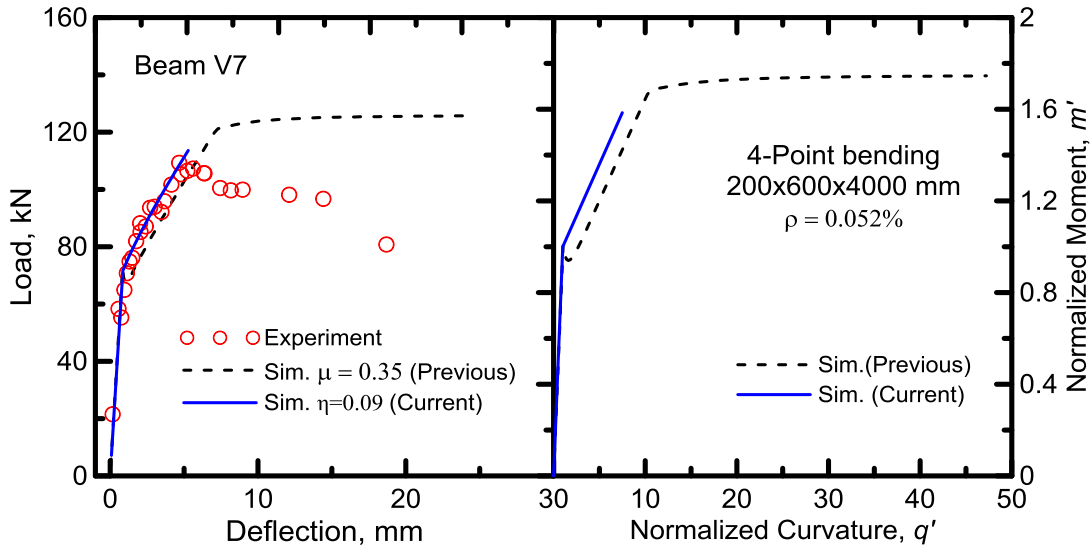


Figure 2.5.14 - Comparison of Current Model with Previous Model for Beam V7

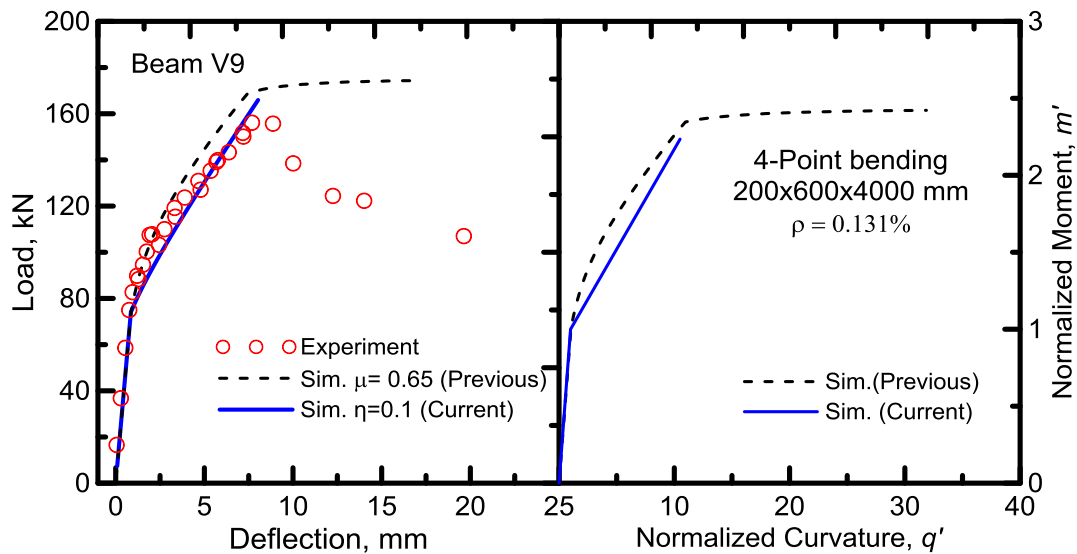


Figure 2.5.15 - Comparison of Current Model with Previous Model for Beam V9

2.5.6 Data Set 5

Full scale beam tests from the Brite/Euram project BRPR-CT98-0813 “Test and design methods for steel fibre reinforced concrete” by Dupont were used for model

verification[26] . Table 2.5.11 provides the details of the 6 beam series, each with 2 replicates, of two grades of normal (NSC), and high strength concrete (HSC). Normal strength concrete used fiber type RC 65/60 BN at 25 and 50 kg/m³ while HSC used fiber type RC 80/60 BP at 60 kg/m³. All beams had a cross section of 0.20 x 0.20 m, with two different span lengths of 1.0 and 2.0 m and tested under four point bending set up with a constant spacing between the two point loads at 0.2 m. These six beams labeled as B7 – B12 which are contained two rebars of size 8, 12 and 16 mm. Steel parameters were Young modulus of 200 GPa, yield strength of 560 MPa, and a concrete cover of 15 mm.

Table 2.5.11 - Details of Beam for Data Set 5

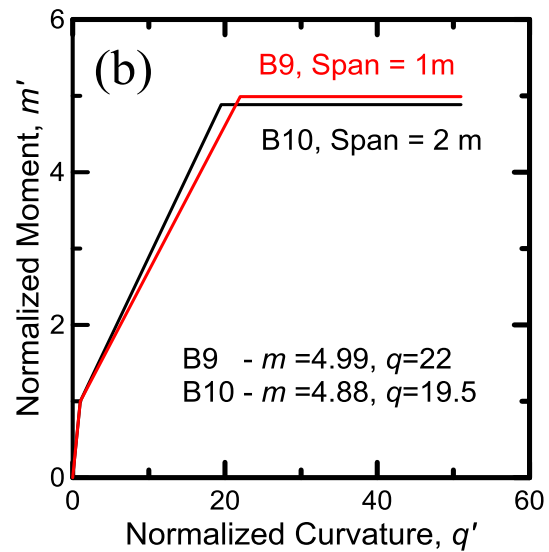
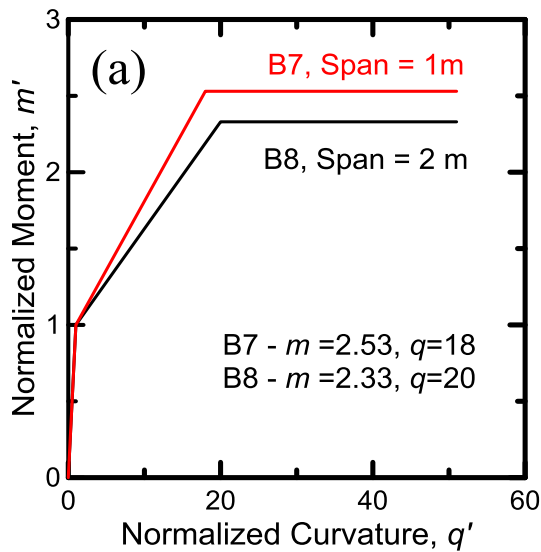
| Beam ID | Mix | Fiber content kg/m ³ | Span m | Rebar |
|---------|-----|---------------------------------|--------|-------|
| B7 | NSC | 25 | 1 | 2-φ8 |
| B8 | NSC | 25 | 2 | 2-φ8 |
| B9 | NSC | 50 | 1 | 2-φ12 |
| B10 | NSC | 50 | 2 | 2-φ12 |
| B11 | HSC | 60 | 1 | 2-φ16 |
| B12 | HSC | 60 | 2 | 2-φ16 |

The normalized moment-curvature relationships and load-deflection responses of the 6 beam series were simulated by the algorithm proposed as shown in Figure 2.5.16 and Figure 2.5.17, respectively. The model parameters were obtained and summarized in Table 2.5.12. Note that the differences between the beam B7, B9 and B11 are expressed in the fiber content increasing from 25 kg/m³ to 50 kg/m³ and 60 kg/m³ and with three levels of rebars of size 8, 12 and 16 mm. Also it is presented that the post cracking stiffness EI_{cr} in terms of simulated moment-curvature diagram increases from 3.72×10^{11} to 7.6×10^{11} and 1.09×10^{12} . Comparing the moment-curvature relationship of beam B8,

B10 and B12, the same conclusion can be made that the increasing the fiber content and reinforced ratio, increases the post-creaked stiffness. It is obvious that the beam with larger span (B8, B10, 12) has slightly lower yield normalized moment than the beam with smaller span but same reinforced mixtures (B7, B9, B11) since the effect of size.

Table 2.5.12 - Simulated Parameters of Current Model for Data Set 5

| ID | $\epsilon_{cr}, 10^{-6}$ | E, GPa | η | m | q | $M_{cr}, KN-mm$ | $\Phi_{cr}, 10^{-6}/mm$ | $EI, 10^{12}$ | $EI_{cr}, 10^{11}$ |
|-----|--------------------------|--------|--------|------|------|-----------------|-------------------------|---------------|--------------------|
| B7 | 130 | 31 | 0.09 | 2.53 | 18 | 5373 | 1.3 | 4.13 | 3.72 |
| B8 | 130 | 31 | 0.07 | 2.33 | 20 | 5373 | 1.3 | 4.13 | 2.89 |
| B9 | 130 | 30 | 0.19 | 4.99 | 22 | 5200 | 1.3 | 4.00 | 7.60 |
| B10 | 130 | 30 | 0.21 | 4.88 | 19.5 | 5200 | 1.3 | 4.00 | 8.40 |
| B11 | 160 | 39 | 0.21 | 6.04 | 25 | 8320 | 1.6 | 5.20 | 10.9 |
| B12 | 160 | 39 | 0.28 | 5.76 | 18 | 8320 | 1.6 | 5.20 | 14.6 |



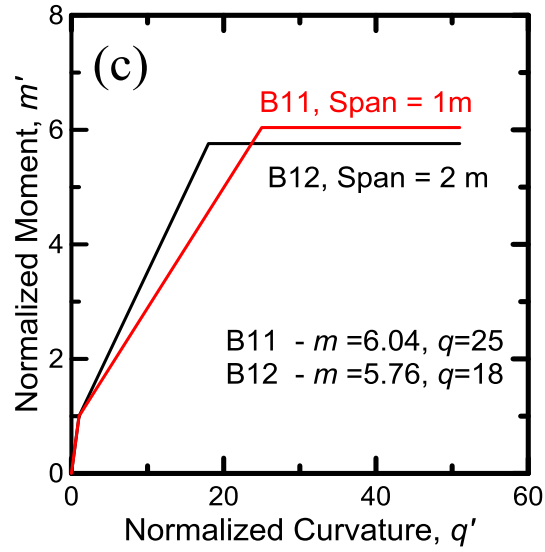
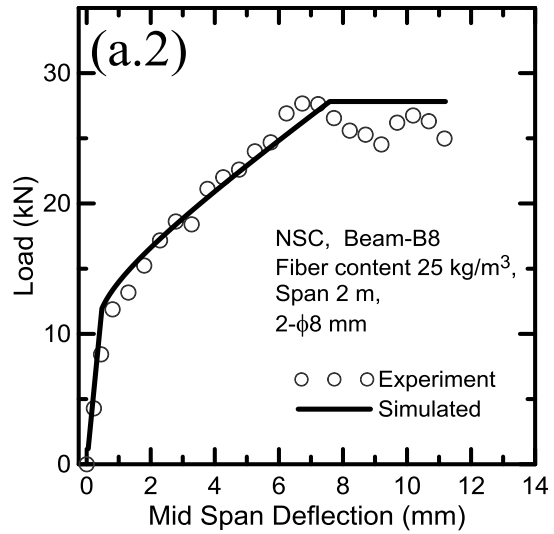
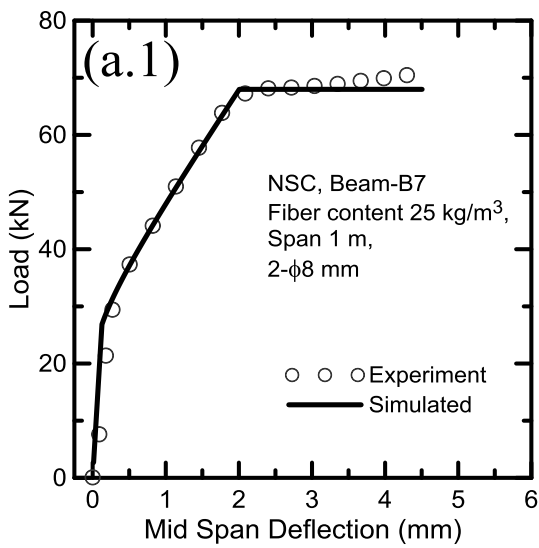


Figure 2.5.16 - Normalized Moment-Curvature Relationship of HRC Beams; (a) B7, B8; (b) B9, B10; (c) B11, B12



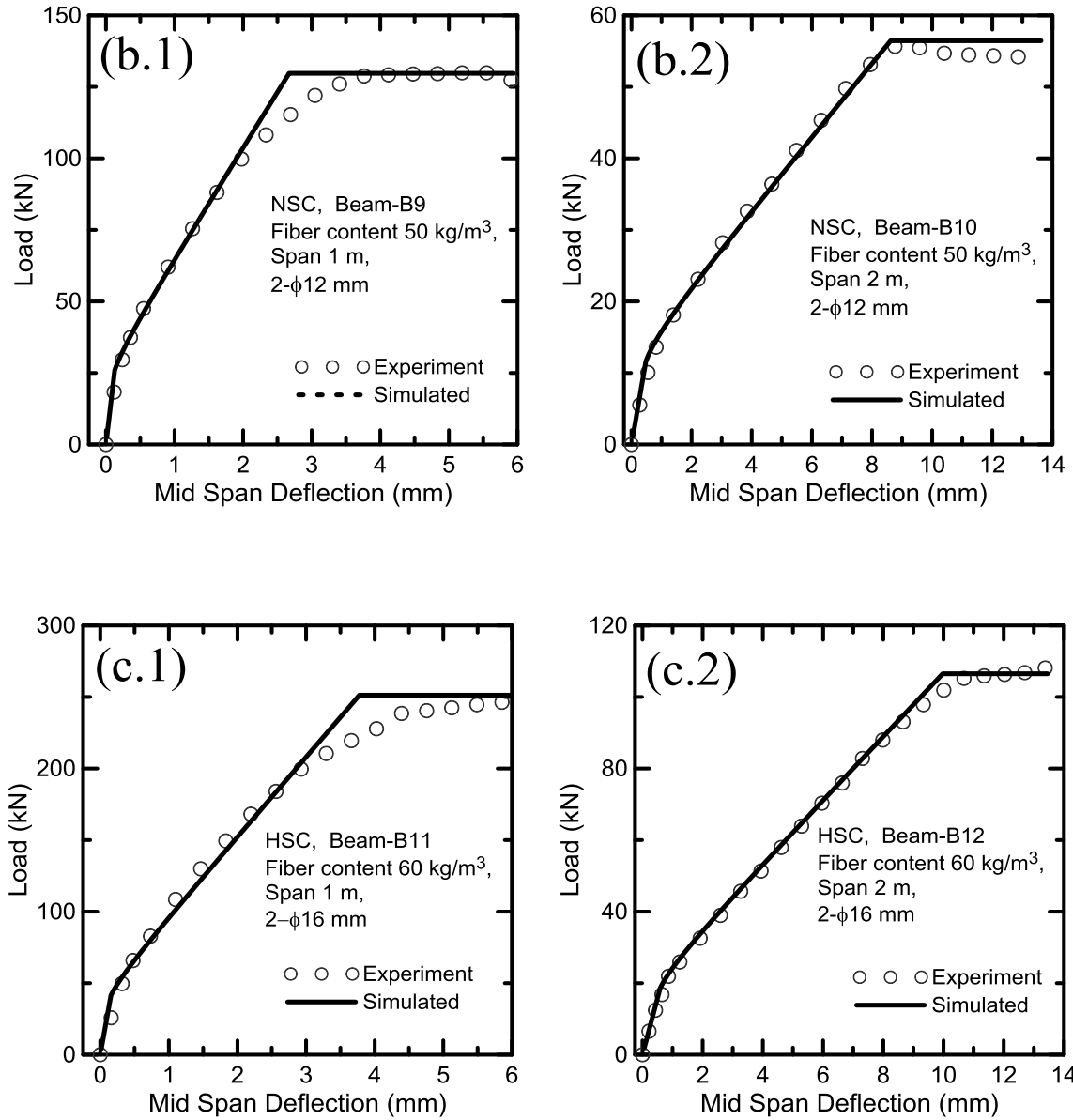


Figure 2.5.17 - Load-Deflection Response of HRC Beams at Three Levels of Fiber Contents; (a) 25 kg/m³; (b) 50 kg/ m³; (60) kg/ m³

Comparison of the predictions with previous model

Using the algorithm of strain-hardening material model which is discussed in Section 1.3, the predictions of load-deflection response and moment-curvature relationship were generated for this set of data and the simulated material parameters of previous model are shown in Table 2.5.13. Figure 2.5.17 to Figure 2.5.19 shows the comparisons of current

model with previous model with these six beams. Note that the parameter of first creaking strain ϵ_{cr} used in current model is 130 μstr for normal strength concrete (NSC) and 160 for the high strength concrete (HSC), which are very close to the ϵ_{cr} of previous model is in the range of 110 to 160. The Young's modulus of current model is slightly higher than that of existed model. It is obvious that the predictions of load-deflection and responses with the both models are similar. Figure 2.5.17 shows the normalized moment-curvature relationships generated from current model has lower yield normalized moment than that of previous model for beam B7 and B8, However the predictions of normalized moment-curvature relationships of beam B9, B10, B11 and B12 generated from this two models are similar as expected.

Table 2.5.13 - Parameters with Previous Model for Data Set 5

| Beam ID | Vf (kg/m ³) | Concrete | | | | | | | Steel | | |
|---------|-------------------------|----------|---------|-----------------------------------|--------------|----------|----------------|----------|------------|-------------|----------------|
| | | μ | E (GPa) | ϵ_{cr} ($\mu\epsilon$) | β_{tu} | ω | λ_{cu} | γ | ρ (%) | E_s (GPa) | f_{sy} (MPa) |
| B7 | 25 | 0.34 | 29 | 110 | 227 | 12 | 32 | 0.7 | 0.251 | 200 | 560 |
| B8 | 25 | | | | | | | | | | |
| B9 | 50 | 0.38 | 29 | 130 | 192 | 10 | 27 | 0.7 | 0.566 | 200 | 560 |
| B10 | 50 | | | | | | | | | | |
| B11 | 60 | 0.56 | 39 | 160 | 156 | 8 | 22 | 1.0 | 1.000 | 200 | 560 |
| B12 | 60 | | | | | | | | | | |

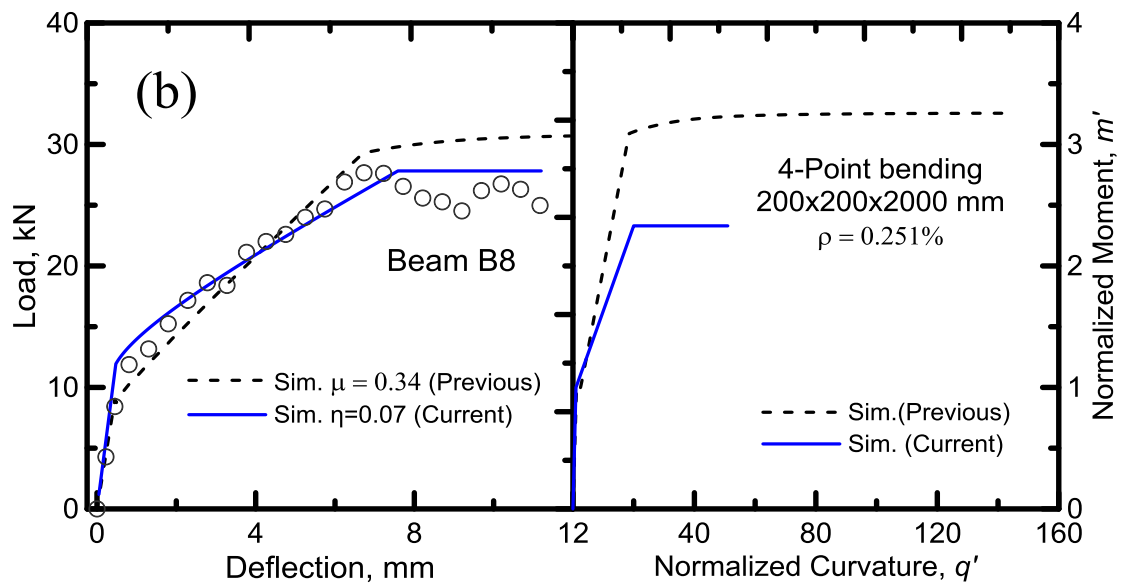
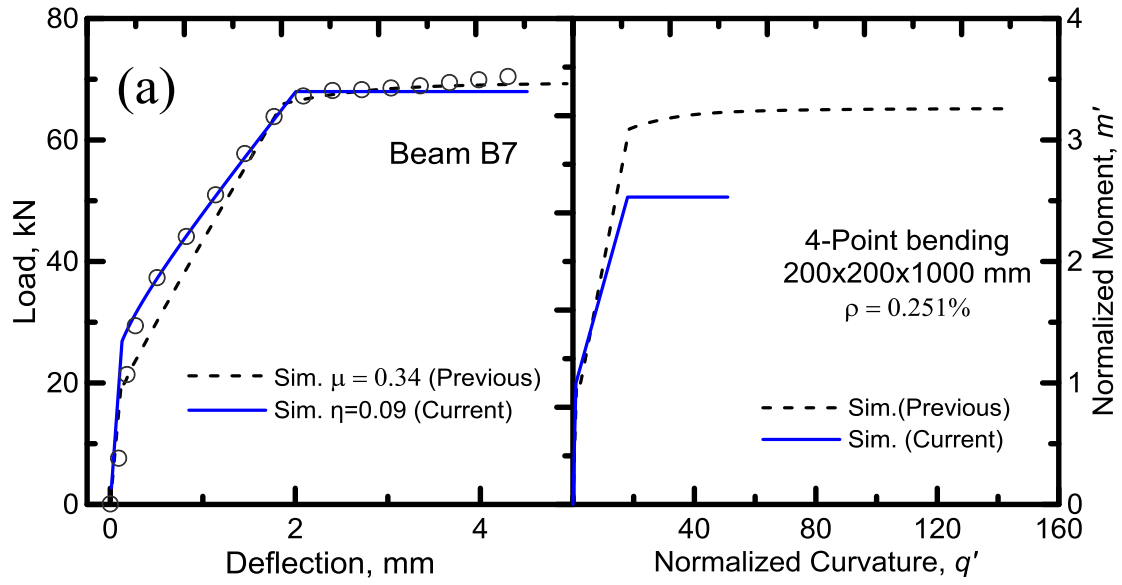


Figure 2.5.17 - Comparison of Current Model with Previous Model; (a) B7; (b) B8

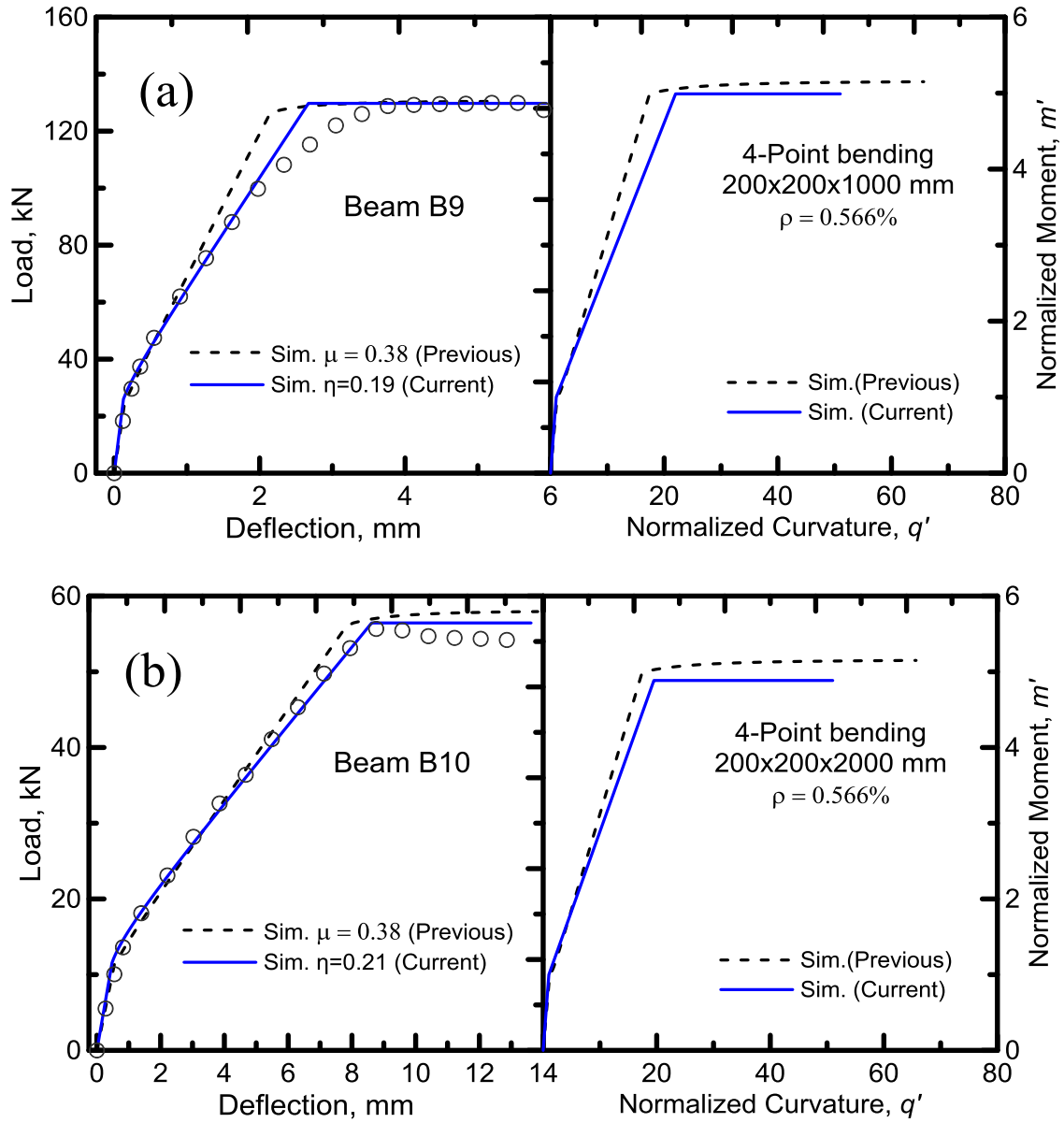


Figure 2.5.18 - Comparison of Current Model with Previous Model; (a) B9; (b) B10

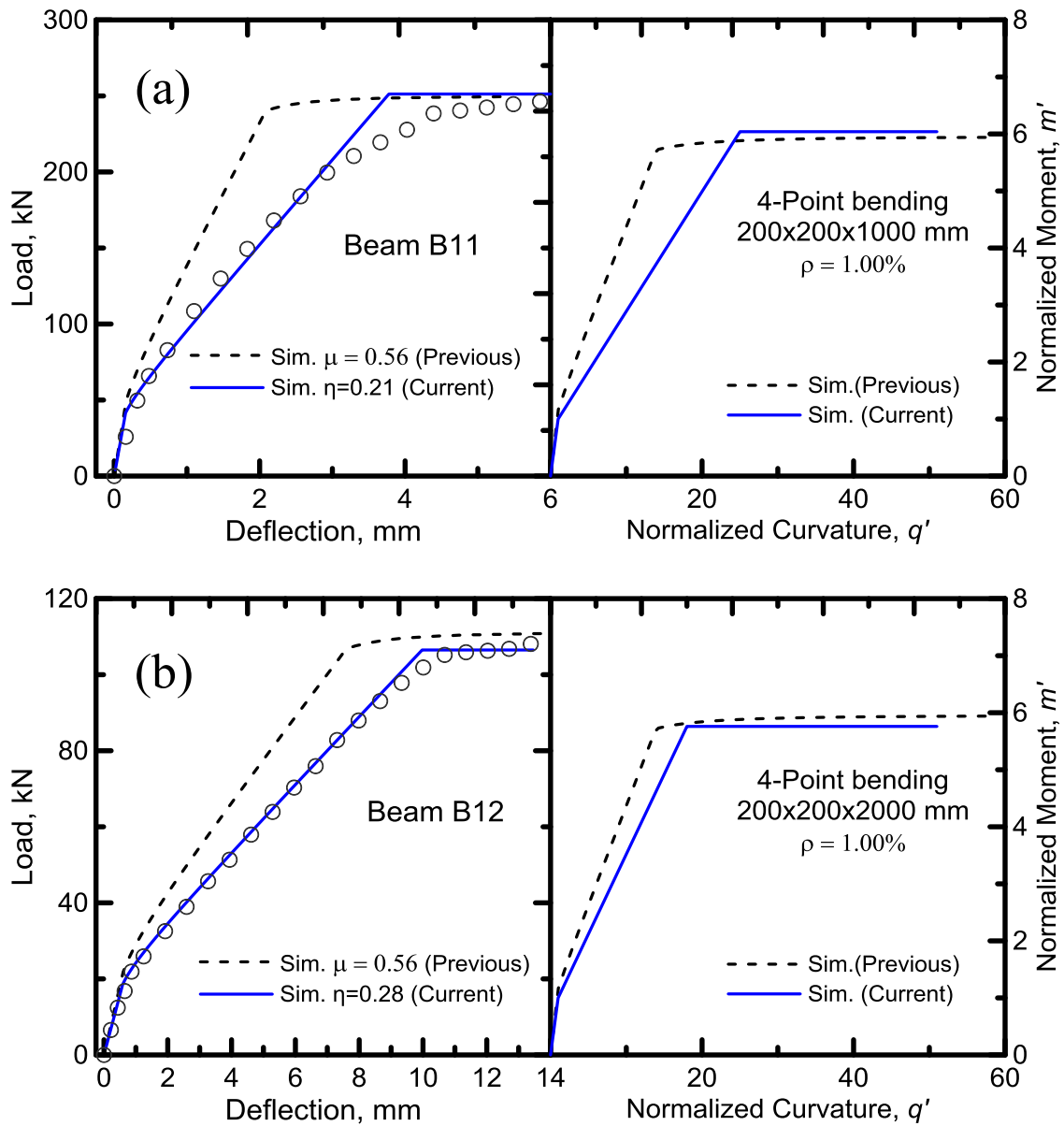


Figure 2.5.19 - Comparison of Current Model with Previous Model; (a) B11; (b) B12

3. - ELASTIC SOLUTIONS AND YIELD LINE THEORY FOR STRAIN-HARDENING STRUCTURAL PANNELS

3.1 Elastic Solution of Plates

3.1.1 Governing Equation for Deflection of Plates

The governing differential equation for the deflections for thin plate bending analysis based on Kirchhoff's assumptions as shown in Eq. (3.1.1). This equation was obtained by Lagrange in 1811.

$$\frac{\partial^4 w}{\partial x^4} + 2 \frac{\partial^4 w}{\partial x^2 y^2} + \frac{\partial^4 w}{\partial y^4} = \frac{p}{D} \quad (3.1.1)$$

Wherein, p is load and D is the flexural rigidity of plate, as shown in Eq. (3.1.2).

$$D = \frac{Et^3}{12(1-\nu^2)} \quad (3.1.2)$$

Equation (3.1.1) may be rewritten, as follows:

$$\nabla^2 (\nabla^2 w) = \nabla^4 w = \frac{p}{D} \quad (3.1.3)$$

Where

$$\nabla^4 () \equiv \frac{\partial^4}{\partial x^4} + 2 \frac{\partial^4}{\partial x^2 y^2} + \frac{\partial^4}{\partial y^4} \quad (3.1.4)$$

Once a deflection function $w(x, y)$ has been determined from Eq. (3.1.1), the stress resultants and the stresses can be calculated based on the elastic theory of plate. But we will not discuss these here.

3.1.2 Boundary Conditions

Boundary conditions are the known conditions on the surfaces of the plate which must be prescribed in advance in order to obtain the solution of Eq. (3.1.1) corresponding to a particular problem. Such conditions include the load $p(x, y)$ on the upper and lower faces of the plate; however, the load has been taken into account in the formulation of the general problem of bending of plates and it enters in the right-hand side of Eq. (3.1.1). It remains to clarify the conditions on the cylindrical surface, i.e., at the edges of the plate, depending on the fastening or supporting conditions. For a plate, the solution of Eq. (3.1.1) requires that two boundary conditions be satisfied at each edge. These may be a given deflection and slope, or force and moment, or some combination of these. For the sake of simplicity, let us list the satisfactions of the clamped, simply supported and free edges of a flat plate.

- 1) Clamped, or built-in, or fixed edge $y=0$

At the clamped edge, the deflection and slope are zero, i.e.,

$$w = 0 \Big|_{y=0} \quad \text{and} \quad \theta \equiv \frac{\partial w}{\partial y} = 0 \Big|_{y=0} \quad (3.1.5)$$

- 2) Simply supported edge $x=a$

At these edges the deflection and bending moment M_x are both zero, i.e.,

$$w = 0 \Big|_{x=a} \quad \text{and} \quad \frac{\partial^2 w}{\partial x^2} = 0 \Big|_{x=a} \quad (3.1.6)$$

- 3) Free edge $y=b$

Suppose that the edge $y = b$ is perfectly free. Since no stresses act over this edge, then it is reasonable to equate all the stress resultants and stress couples occurring at points of this edge to zero, i.e.,

$$M_y = 0 \Big|_{y=b}, Q_y = 0 \Big|_{y=b}, M_{yx} = 0 \Big|_{y=b} \quad (3.1.7)$$

3.2 Elastic Solutions of Various Types of Panels

3.2.1 Case 1 – Round Panel

When circular plates are analyzed, it is convenient to express the governing differential equation (3.1.1) in polar coordinates as:

$$\nabla^4 w = \left(\frac{\partial^2}{\partial r^2} + \frac{1}{r} \frac{\partial}{\partial r} + \frac{1}{r^2} \frac{\partial^2}{\partial \theta^2} \right) \left(\frac{\partial^2 w}{\partial r^2} + \frac{1}{r} \frac{\partial w}{\partial r} + \frac{1}{r^2} \frac{\partial^2 w}{\partial \theta^2} \right) = \frac{p}{D} \quad (3.2.1)$$

If only consider the axisymmetric case. Eq. (3.2.1) can be simplified as:

$$\nabla^4 w = \left(\frac{\partial^2}{\partial r^2} + \frac{1}{r} \frac{\partial}{\partial r} \right) \left(\frac{\partial^2 w}{\partial r^2} + \frac{1}{r} \frac{\partial w}{\partial r} \right) = \frac{p}{D} \quad (3.2.2)$$

The solution of Eq. (3.2.2) with the loading $p = p_0$ (constant) is:

$$w = C_1 \ln r + C_2 r^2 \ln r + C_3 r^2 + C_4 + \frac{p_0 r^4}{64D} \quad (3.2.3)$$

Where, C_1, C_2, C_3, C_4 are constants of integration and can be obtained from the boundary conditions.

A radius of R and the thickness of t are considered here with a round panel subjected with a concentrated center force P with two boundary conditions which are-

- i) Simply supported edge (Case 1.1)
- ii) Clamped edge (Case 1.2)

Case study 1.1 Round panel subjected with concentrated load at center and simply supported edge

The round panel subjected with the concentrated load at center is shown in Figure 3.2.1. The elastic solution of this case can be considered as two parts: a) solution of the round panel subjected with concentrated load at center and clamed edges; b) solution of the round panel subjected with the edges moment.

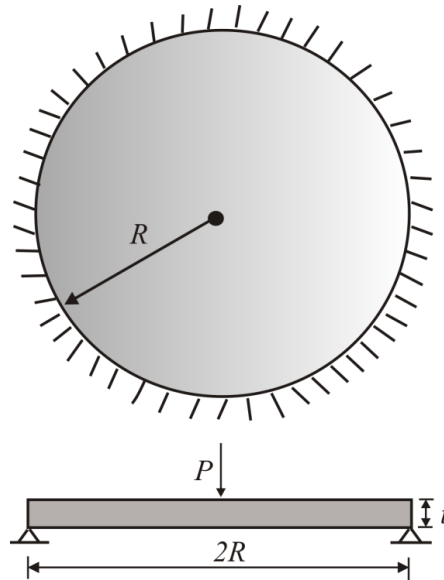


Figure 3.2.1 - Round Panel Subjected with Concentrated Load at Center and Simply Supported Edge

The procedure to get the deflection of round panel is to get the constants in the Eq. (3.2.3) by applying the boundary conditions. The solution for the solution of part a) can be obtained as:

$$w = \frac{P}{16\pi D} \left(2r^2 \ln \frac{r}{R} + R^2 - r^2 \right) \quad (3.2.4)$$

The solution of part b) can be obtained and shown in below:

$$w = -\frac{M_o r^2}{2(1+\nu)D} + \frac{M_o R^2}{2(1+\nu)D} \quad (3.2.5)$$

Wherein M_o is the applied moment in the edge of round panel and $M_o=P/4\pi$

The solution for the Case 1.1 is the summation of the Eq. (3.2.4) and Eq.(3.2.5), and the deflection as show in Eq. (3.2.6)

$$w = \frac{P}{16\pi D} \left(2r^2 \ln \frac{r}{R} + \frac{3+\nu}{1+\nu} (R^2 - r^2) \right) \quad (3.2.6)$$

The maximum deflection w_{\max} is calculated by substituting the $r=0$ and the expression of maximum deflection is presented in Eq (3.2.7).

$$w_{\max} = \frac{PR^2}{16\pi D} \left(\frac{3+\nu}{1+\nu} \right) \quad (3.2.7)$$

Case study 1.2 simply Clamped edge panel subjected with concentrated load at center

A radius of R and the thickness of t is considered here with a clamped edge round panel subjected with a concentrated center force P , as shown in Figure 3.2.2. The elastic solution of this case can be calculated by substituting the $p= -P/2\pi r$ into the Eq. (3.2.2) and solve the differential equation as:

$$w = \frac{P}{8\pi r} (r^2 \ln r - r^2) + \frac{C_1 r^2}{4} + C_2 \ln r + C_3 \quad (3.2.8)$$

Imposing the boundary conditions:

$$\text{At } r = 0, \quad w \neq 0, \text{ so we must have } C_2=0;$$

$$\text{At } r = R, \quad \frac{dw}{dr} = 0 \rightarrow C_1 = \frac{P}{4\pi D} (1 - 2 \ln R);$$

$$\text{At } r = R, \quad w = 0 \rightarrow C_3 = \frac{PR^2}{16\pi D};$$

Substituting the C_1 , C_2 and C_3 to the Eq. (3.2.8) the solution for the solution of part a) can be obtained as:

$$w = \frac{P}{16\pi D} \left(2r^2 \ln \frac{r}{R} + R^2 - r^2 \right) \quad (3.2.9)$$

The maximum deflection w_{\max} is calculated by substituting the $r=0$ and the expression of maximum deflection is presented in Eq. (3.2.10).

$$w_{\max} = \frac{PR^2}{16\pi D} \quad (3.2.10)$$

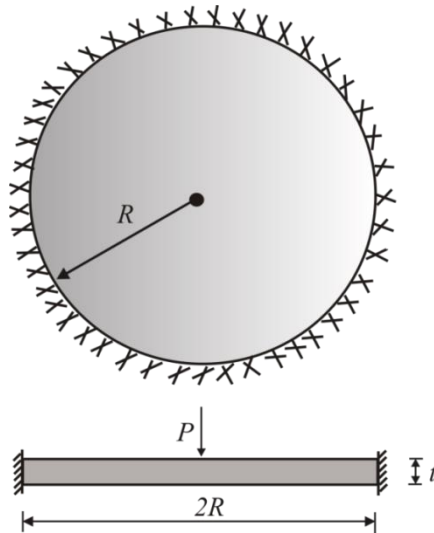


Figure 3.2.2 - Clamped Edge Round Panel Subjected with Concentrated Load at center

3.2.2 Case 2 – Rectangular Panel

Levy developed a method for solving rectangular plate bending problem with only one pair of edges (opposite edges) to be simply supported while the other pair can have any type of boundary conditions using single Fourier series [27]. It is obvious that the Levy solution should satisfy not only the governing differential equation as discussed in Section 1 but also the boundary conditions. The solution for governing differential

equation can be obtained in two parts as the homogeneous part (w_o) and the particular integral (w_I). The total solution will be the sum of these two solutions which can be written as:

$$w = w_0 + w_1 \quad (3.2.11)$$

The homogeneous solution should satisfy the differential equation

$$\nabla^2 (\nabla^2 w_0) = 0 \quad (3.2.12)$$

Let us consider a rectangular plate with sides $a \times b$ which is simply supported along the edges $x=0, a$. The simply supported boundary conditions can be written as Eq. (3.2.13) and the solution of the differential equation given in Eq. (3.2.14).

$$x = 0, a; \quad w = \frac{\partial^2 w}{\partial x^2} = 0 \quad (3.2.13)$$

$$w_0 = \sum_{m=1}^{\infty} f_m(y) \sin \alpha_m x \quad (3.2.14)$$

Wherein $f_m(y)$ is a function of y only, and $\alpha_m = m\pi/a$.

According the Levy's solution, the general solution for $f_m(y)$ can be written as

$$f_m(y) = \sum_{m=1}^{\infty} [A_m \cosh \alpha_m y + B_m \sinh \alpha_m y + C_m \alpha_m y \sinh \alpha_m y + D_m \alpha_m y \cosh \alpha_m y] \quad (3.2.15)$$

Where A_m, B_m, C_m, D_m are constants and the solution of the homogeneous differential equation (3.2.14) as:

$$w_0 = \sum_{m=1}^{\infty} [A_m \cosh \alpha_m y + B_m \sinh \alpha_m y + C_m \alpha_m y \sinh \alpha_m y + D_m \alpha_m y \cosh \alpha_m y] \sin \alpha_m x \quad (3.2.16)$$

Next, we will assume the particular integral (w_I) in the form

$$w_1 = \sum_{m=1}^{\infty} p_m(y) \sin \alpha_m x \quad (3.2.17)$$

In which $p_m(y)$ is an arbitrary function of y . It may be noted that the above assumed form for the particular integral also satisfies the simply supported boundary conditions along $x=0, a$ (Eq. 3.2.13). The lateral load $q(x,y)$ acting on the plate can be expressed in terms of Fourier series as:

$$q(x, y) = \sum_{m=1}^{\infty} q_m(y) \sin \alpha_m x \quad (3.2.18)$$

Where q_m is determined from $q_m = \frac{2}{a} \int_0^a q(x, y) \sin \alpha_m x dx$. Substituting Eqs. (3.2.17) and (3.2.18) in the governing differential equation given in Eq. (3.1.3), we get

$$w_1 = \frac{q_m}{\alpha_m^4 D} \quad (3.2.19)$$

Where q_m is the Fourier coefficient. For uniform loading, the q_m can be written as:

$$q_m = \frac{2}{a} \int_0^a q(x, y) \sin \alpha_m x dx = \frac{4q}{m\pi}, m = 1, 3, 5... \quad (3.2.20)$$

The rectangular panel with side $a \times b$ and thickness of t is considered here with uniform loading p_o and different boundary conditions which are-

- i) Four edges simply supported (Case 2.1)
- ii) Four edges clamped (Case 2.2)

Case Study 2.1 Rectangular panel with four edges simply supported

According to the Levy's solution, the homogeneous solution given in Eq. (3.2.16) is combined with the particular integral given in Eq. (3.2.19) with the Fourier coefficient q_m given in Eq. (3.2.20) for a uniformly distributed load. Hence the complete solution can be written as:

$$w = \sum_{m=1,3}^{\infty} \left[A_m \cosh \alpha_m y + B_m \sinh \alpha_m y + C_m \alpha_m y \sinh \alpha_m y + D_m \alpha_m y \cosh \alpha_m y + \frac{4qa^4}{m^5 \pi^5 D} \right] \sin \alpha_m x \quad (3.2.21)$$

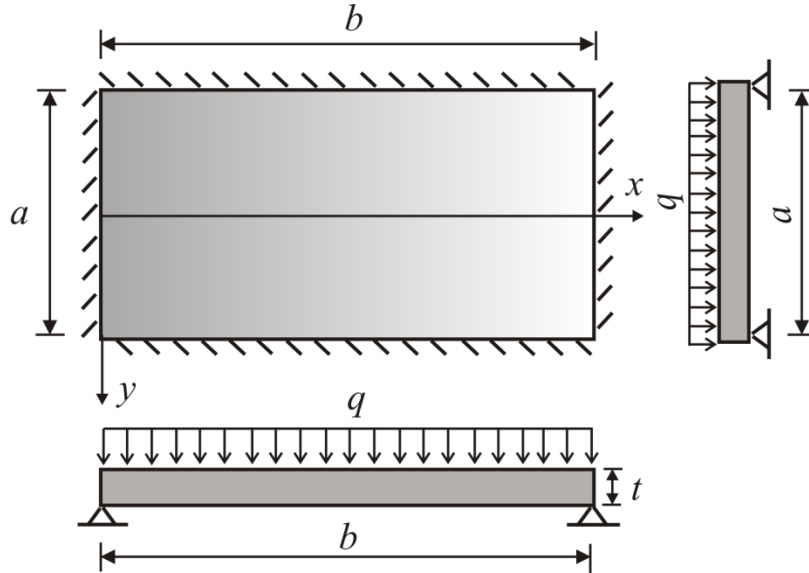


Figure 3.2.3 - Simply Supported Rectangular Panel Subjected with Uniform Load

The coordinate axes selected for this case are such that the boundary conditions and the loading are symmetrical about the x-axis, as shown in Figure 3.2.3. The terms $\cosh \alpha_m y$ and $\alpha_m y \sinh \alpha_m y$ are even functions and hence are symmetrical about x-axis, while terms $\sin \alpha_m y$ and $\alpha_m y \cosh \alpha_m y$ are odd functions and are antisymmetric about the x-axis. Since the boundary conditions and loading are symmetric about the x-axis, the lateral deflection also will be symmetric about x-axis. Hence only symmetric functions in y need to be considered in the homogeneous solution. This means that the constants B_m and D_m need not be considered for this problem. Hence the complete solution for the problem can be taken as:

$$w = \sum_{m=1,3}^{\infty} \left[A_m \cosh \alpha_m y + C_m \alpha_m y \sinh \alpha_m y + \frac{4qa^4}{m^5 \pi^5 D} \right] \sin \alpha_m x \quad (3.2.22)$$

The constants A_m and C_m are now determined by using the boundary conditions along the edges $y=b/2, -b/2$. Since these edges are simply supported, the boundary conditions can be written as

$$y = \frac{b}{2}, -\frac{b}{2}; \quad w=0, \quad w = \frac{\partial^2 w}{\partial x^2} = 0 \quad (3.2.23)$$

Substituting the Eq.(3.2.23) in the Eq. (3.2.22). The constant A_m and C_m can be solved and the solution of deflection can be obtained as:

$$w = \frac{qa^4}{\pi^5 D} \sum_{m=1,3}^{\infty} \left[\frac{1}{m^5 \cosh \frac{\alpha_m b}{2}} \left\{ - \left(4 + \alpha_m b \tanh \frac{\alpha_m b}{2} \right) \cosh \alpha_m y + 2\alpha_m y \sinh \alpha_m y \right\} + \frac{4}{m^5} \right] \sin \alpha_m x \quad (3.2.24)$$

The maximum deflection occurs at the center of the plate. Substituting the $x=a/2, y=0$ in Eq. (3.2.25). The expression for maximum deflection can be written as

$$w_{\max} = \frac{4qa^4}{\pi^5 D} \sum_{m=1,3}^{\infty} \frac{(-1)^{\frac{m-1}{2}}}{m^5} - \sum_{m=1,3}^{\infty} \frac{(-1)^{\frac{m-1}{2}}}{m^5} \left(\frac{\frac{\alpha_m b}{4} \tanh \frac{\alpha_m b}{2} + 1}{\cosh \frac{\alpha_m b}{2}} \right) \quad (3.2.25)$$

It can be shown that $\sum_{m=1,3}^{\infty} \frac{(-1)^{\frac{m-1}{2}}}{m^5} = \frac{5\pi^5}{1536}$, so we obtain the expression for maximum

deflection as

$$w_{\max} = \frac{5qa^4}{384D} - \frac{4qa^4}{\pi^5 D} \sum_{m=1,3}^{\infty} \frac{(-1)^{\frac{m-1}{2}}}{m^5} \left(\frac{\frac{\alpha_m b}{4} \tanh \frac{\alpha_m b}{2} + 1}{\cosh \frac{\alpha_m b}{2}} \right) \quad (3.2.26)$$

If assume the Poisson's ration as 0.3, for this case, the Eq. (3.2.26) can be simplified as a general expression as:

$$w_{\max} = \alpha \frac{qa^4}{D} \quad (3.2.27)$$

Where α is a numerical factor which is related to the ratio of b/a , as shown in Table 3.2.1 and a is refer to the length of the shorter side.

Table 3.2.1 - Numerical Factor for Maximum Deflection for Case 2.1

| b/a | α |
|----------|----------|
| 1 | 0.00406 |
| 1.5 | 0.00771 |
| 2 | 0.01013 |
| 4 | 0.01282 |
| ∞ | 0.01302 |

Hence it may be concluded that for all practical purposes, for rectangular plates having dimensions such that $b/a \geq 4$, the maximum deflection can be computed from beam equations.

Case Study 2.2 Rectangular panel with four edges clamped

The solution of this case can be obtained by referring the Westergaard approximate solution for rectangular panels [28].The maximum deflection equations can be written as:

$$w_{\max} = C(1-\nu^2) \left(\frac{qa^4}{Et^3} \right) \quad (3.2.28)$$

Wherein, a is the short span length and C is parameter which is related to the boundary condition. With the clamped edges, the C can be expressed as:

$$C = \frac{0.032}{1+\beta^4} \quad (3.2.29)$$

Wherein, $\beta = a/b$, b is the longer span length.

3.2.3 Case 3- Square Panel

The square panel with side a and thickness of t is considered here with uniform loading p_o and different boundary conditions which are-

- i) Four edges simply supported (Case 3.1)
- ii) Four edges clamped (Case 3.2)

Based on the solutions of rectangular panel discussed in Section 3.2, it is early to obtain the solution of square panel since the square panel is a special case comparing with rectangular panel.

For the square panel with four edges simply supported (Case 3.1), the maximum deflection can be calculated by substituting $b/a=1$ in the Eq. (3.2.17) and written as:

$$w_{\max} = 0.00406 \frac{qa^4}{D} \quad (3.2.30)$$

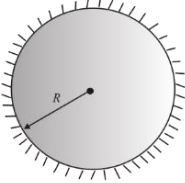
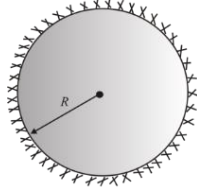
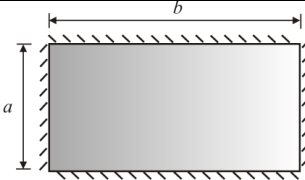
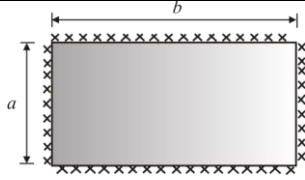
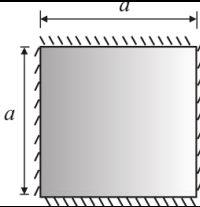
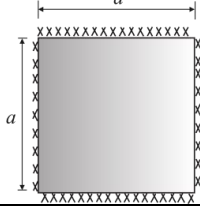
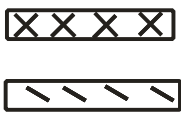
For the square panel with four edges clamped (Case 3.2), the maximum deflection can be calculated by substituting $\beta = a/b = 1$ in Eq. (3.2.29) to get the parameter C and calculate maximum deflection by using Eq. (3.2.28).

$$w_{\max} = \frac{0.032}{2} (1-\nu^2) \left(\frac{qa^4}{Et^3} \right) \quad (3.2.31)$$

The maximum deflection equations based on the elastic theory of plate for all cases are shown in Table 3.2.2. Where, ν is Poisson's ratio, $\nu=3$ for Case 2.1 and 3.1 $D = \frac{Et^3}{12(1-\nu^2)}$

Parameter α can be obtained from Table 3.2.1.

Table 3.2.2 – Elastic Maximum Deflection Equations for Case 1 to Case 3

| Shape | Case # | Boundary Conditions | Geometry | Maximum Deflection w_{max} | | | | | | | | | |
|---|--------|---------------------|---|---|--|--------|----------|-----------------|---|---|------------------|---|---|
| Round Panel | 1.1 | Simply supported |  | $\frac{PR^2}{16\pi D} \left(\frac{3+\nu}{1+\nu} \right)$ | | | | | | | | | |
| | 1.2 | Clamped |  | $\frac{PR^2}{16\pi D}$ | | | | | | | | | |
| Rectangular Panel | 2.1 | Simply supported |  | $\alpha \frac{qa^4}{D}$ | | | | | | | | | |
| | 2.2 | Clamped |  | $\frac{0.032(1-\nu^2)}{1+\beta^4} \left(\frac{qa^4}{Et^3} \right)$ | | | | | | | | | |
| Square Panel | 3.1 | Simply supported |  | $0.00406 \frac{qa^4}{D}$ | | | | | | | | | |
| | 3.2 | Clamped |  | $\frac{0.032}{2} (1-\nu^2) \left(\frac{qa^4}{Et^3} \right)$ | | | | | | | | | |
|  | | | | <table border="0"> <tr> <td></td> <td>Moment</td> <td>Rotation</td> </tr> <tr> <td>Clamped support</td> <td>✓</td> <td>✗</td> </tr> <tr> <td>Simply supported</td> <td>✗</td> <td>✓</td> </tr> </table> | | Moment | Rotation | Clamped support | ✓ | ✗ | Simply supported | ✗ | ✓ |
| | Moment | Rotation | | | | | | | | | | | |
| Clamped support | ✓ | ✗ | | | | | | | | | | | |
| Simply supported | ✗ | ✓ | | | | | | | | | | | |

3.3 Yield Line Analysis Approach

Yield line design is a well-founded method of designing reinforced concrete slabs, and similar types of elements. It uses yield line theory to investigate failure mechanisms at the ultimate limit state. The theory is based on the principle that work done in rotating yield lines is equal to work done in moving the loads [29][30], as shown in:

$$W_{\text{ext}} = W_{\text{int}} \quad (3.3.1)$$

$$\sum(N \delta) = \sum(m l \theta) \quad (3.3.2)$$

Wherein, W_{ext} is the external work; W_{int} is the internal work; N is the load acting within a particular region; δ is the vertical displacement of the load on each region; m is the unit moment in or moment of resistance of the slab ; l is the length of yield line or its projected length onto the axis of rotation for that region. θ is the rotation of the region about its axis of rotation.

When applying the Work Method for yield line analysis the calculations for the external work due to loads and the internal work due to dissipation of energy within the yield lines are carried out independently. The results are then made equal to each other and from the resulting equations the unknown, be it the ultimate moment 'm' generated in the yield lines or the ultimate failure distributed load 'q' of the slab is evaluated.

The slab is divided into rigid regions that rotate about their respective axes of rotation along the support lines. If the point of maximum deflection is given a value of unity then the vertical displacement of any point in the regions is thereby defined. The work done due to external loads is evaluated by taking all external loads on each region, finding the center of gravity of each resultant load and multiplying it by the distance it travels.

The work done due to dissipation of energy is quantified by projecting all the yield lines around a region onto, and at right angles to, that region's axis of rotation. These projected lengths are multiplied by the moment acting on each length and by the angle of rotation of the region. At the small angles considered, the angle of rotation is equated to the tangent of the angle produced by the deflection of the region.

3.4 Moment-Load Relationship of Panels

Work method has been used to calculate the moment-load relationship for all the basic configurations of slabs namely square, rectangle and circular with all possible support conditions by Aswani, K [31]. In this section, the derivation of moment-curvature relationship for round panel having a point load acting at center with a magnitude of P are presented here as an example to show the algorithm and the equations of other types of panels are obtained from [30] and listed in Table 3.4.1.

3.4.1 Case Study 1 – Applied Load vs. Yield Line Moment Relationship for Round Panels

Round panels of radius R is considered here with a point load of ' P ' acting at the center on it. Yield lines form a fan shaped design and it is considered that each point on the yield line is consistent and under tension. Hogging moment along the yields lines and sagging moment along the supports are also assumed to be equal in magnitude. Two end conditions can be considered which are –

- i) It is simply supported (Case 1.1)
- ii) It has clamped support (Case 1.2)

Derivation for round panel with simply supported is presented here. Cases 2.1 can be derived similarly.

Case 1.1 –Round Panel with Simply Supported Edges

In figure 3.4.1, if one defines number of cracks as n , then the central angle α can be calculated as $2\pi/n$. It has been assumed here that when number of cracks, n tends to infinity, the angle α becomes zero. In case of a simply supported three point ring specimens, n is taken as 3. Flexural capacity of round slab simply supported (Case 1.1) subjected to a center-point loading is shown in figure 3.4.1. Note that depending on the number of yield lines, the internal energy dissipation changes.

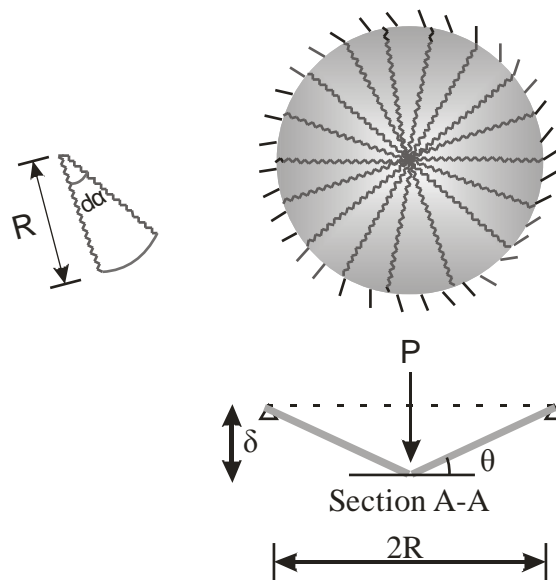


Figure 3.4.1 - Principle of Virtual Work of a Round Panel with Simply Supported in its Contour and Subjected to Center Point Load

It is however shown that in the case of simply supported round slab, the allowable applied load can be related to the bending moment capacity which is determined through laboratory tests on flexural samples.

$$W_{int} = W_{ext} \quad ; \theta = \frac{\delta}{R}$$

$$dW_{int} = MR\theta d\alpha = M\delta d\alpha$$

$$W_{ext} = P\delta$$

$$W_{int} = W_{ext} = \int_0^{2\pi} M\delta d\alpha = 2\pi M\delta = P\delta$$

$$M = \frac{P}{2\pi} \quad (3.4.1)$$

If the support is fixed (Case 1.2), the solution would yield:

$$W_{int} = W_{ext}$$

$$\int_0^{2\pi} M\delta d\alpha + 2\pi RM\theta = 4\pi M\delta = P\delta \quad (3.4.2)$$

$$M = \frac{P}{4\pi} \quad (3.4.3)$$

3.4.2 Case Study 2 – Applied Load vs. Yield Line Moment Relationship for Rectangular Panels

Rectangular slab of length ‘b’ and breadth ‘a’ has been considered here and a uniformly distributed load ‘q’ is acting on it. It is assumed that yield lines are at 45° to the sides and each point on the yield line is consistent and under tension. Hogging moment at yield line and sagging moment about the edges are also assumed to be equal in magnitude.

- i) All sides are simply supported (Case 2.1)
- ii) All sides have clamped supports (Case 2.2)

Derivation for Rectangular panel with simply supported is presented here. Cases 2.1 can be derived similarly.

Case 2.1 – Rectangular slab with simply supported

The slab is divided into rigid regions that rotate about their respective axes of rotation along the support lines. If the point of maximum deflection is given a value of unity then the vertical displacement of any point in the regions is thereby defined.

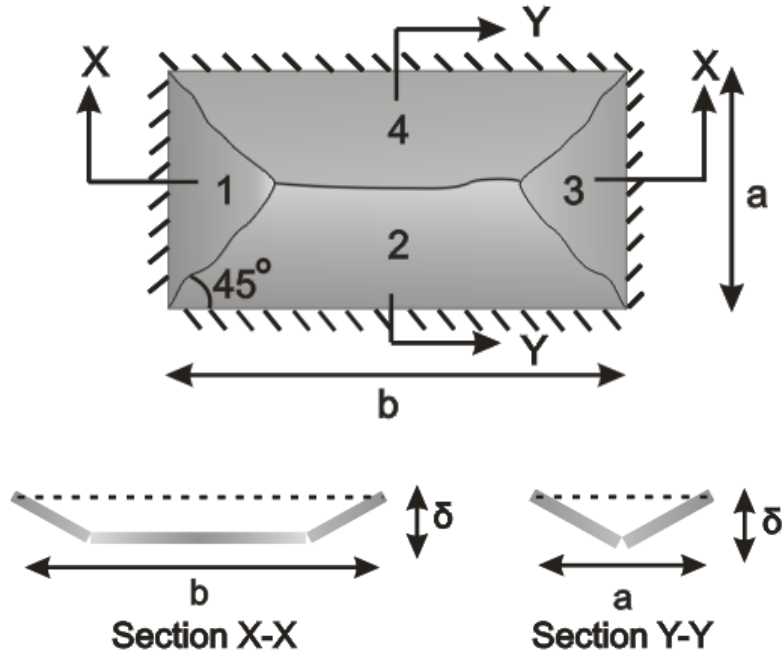


Figure 3.4.2 - Simply Supported Rectangular Slab

The expenditure of external loads is evaluated by taking all external loads on each region, finding the center of gravity of each resultant load and multiplying it by the distance it travels. Two groups are considered the triangles and the trapezoidal sections:

$$W_{ext} = \sum(N \delta) = \left(\frac{1}{3} q a^2 \right) + \left(\frac{1}{2} q (b-a) a \right) = \frac{qa}{6} (3b-a) \quad (3.4.4)$$

In the above expression, the first half of the expression consists of both the triangles (regions 1 and 3 completely and parts of region 2 and 4). Their area is a^2 and therefore equivalent point load is expressed as qa^2 and $1/3$ is the deflection of the centroid when

maximum deflection has been assumed as unity. Second half of the expression is composed of the rectangle at the center which consists of the remaining regions of two and four.

The internal work done due to dissipation of energy is quantified by projecting all the yield lines around a region onto, and at right angles to, that region's axis of rotation. These projected lengths are multiplied by the moment acting on each length and by the angle of rotation of the region. At the small angles considered, the angle of rotation is equated to the tangent of the angle produced by the deflection of the region. Assuming the moment caused due to the rotation of yield lines as m (positive/sagging) and moment caused due to the rotation about the clamped sides as m' (negative/hogging).

$$W_{\text{int}} = \sum (m l \theta) = \left(ma \frac{2}{a} \right) + \left(mb \frac{2}{a} \right) + \left(m a \frac{2}{a} \right) + \left(mb \frac{2}{a} \right) \quad (3.4.5)$$

Term 1 and 3 represent the triangular portion and terms 2 and 4 represent the Trapezoidal sections contributions. There are no negative moments since simply supported panel. one

gets - $W_{\text{int}} = 4m \left(1 + \frac{b}{a} \right)$

Energy equilibrium requires: $W_{\text{ext}} = W_{\text{int}}$, from which one gets-

$$m = \frac{qa^2(3b-a)}{24(b+a)} \quad (3.4.6)$$

3.4.3 Case Study 3 – Applied Load vs. Yield Line Moment Relationship for Square Panels

Square slab of edge length a is considered here with a distributed load of 'q' acting on it.

It is assumed that yield lines are at 45° to the sides and each point on the yield line is

consistent and under tension. Hogging moment about the yield lines and sagging moment about the clamped supports are also assumed to be equal in magnitude. Three end conditions can be considered which are –

- i) All sides are simply supported (Case 3.1)
- ii) All sides have clamped supports (Case 3.2)

Case 3.1 – Square panel with simply supported edges

Plastic analysis approach uses the principle of virtual work to equate the internal and external work to obtain the collapse load. Similarly the yield pattern is used to define the potential collapse mechanism of a plate supported along its two or four edges. If the panel has fixed edges, then the yielding along the edge is also needed to be included in the calculations.

From the relationship of equating the external work done by loads moving to the internal energy dissipated by rotations about yield line, one gets:

$$W_{\text{ext}} = W_{\text{int}} \quad (3.4.7)$$

$$\sum(N \delta) = \sum(ml \theta) \quad (3.4.8)$$

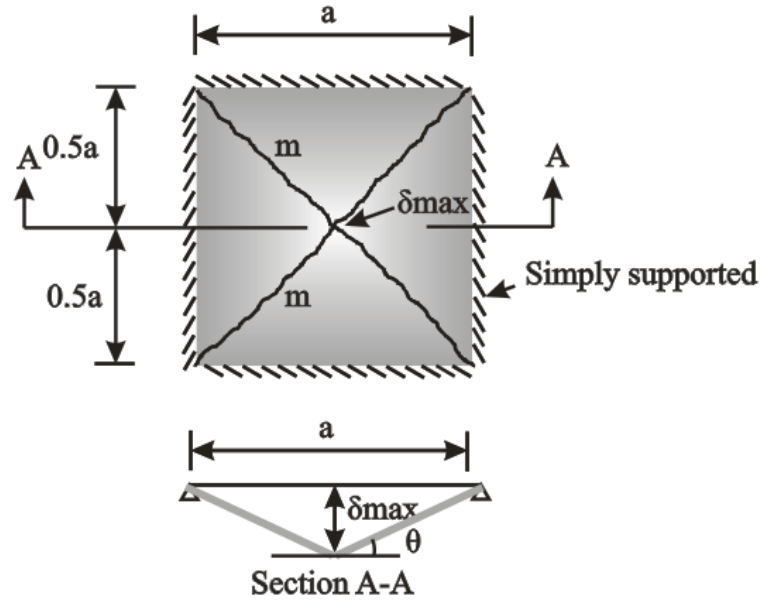


Figure 3.4.3 - Simply Supported Square Panel

In left hand side, q is the uniformly distributed load and $a^2/4$ is the area of each wedge (So the equivalent point load is $q \times a^2/4$) and $\delta_{\max}/3$ is the deflection of the centroid. On the right hand side, a is the length of the square as the rotations are projected onto the sides. Rotation angle, θ , can be calculated from geometry shown in Figure 3.4.3 as $\delta_{\max}/0.5L$.

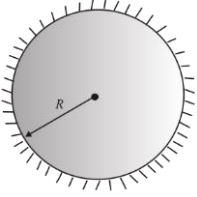
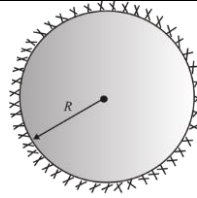
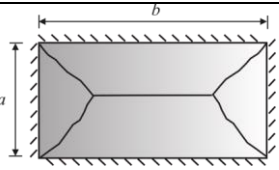
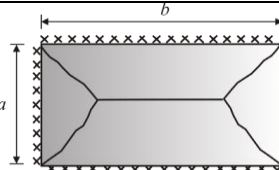
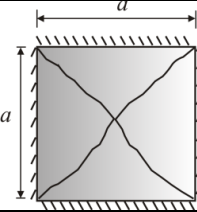
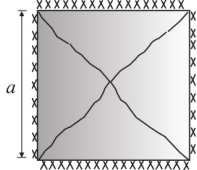






$$4 \left(q \frac{a^2}{4} \frac{\delta_{\max}}{3} \right) = 4 \left(m a \frac{\delta_{\max}}{0.5a} \right) \quad (3.4.9)$$

Simplifying equation 2-3 and solving for moment, one gets-

$$\frac{4a^2q}{12} = 8m \quad , \quad m = \frac{qa^2}{24} \quad (3.4.10)$$

Where m is the moment along the yield lines, q is the uniformly distributed load and a is the length of the square side.

Table 3.4.1 - The Relationships between Load and Moment for Various Panels

| Shape | Case # | Boundary Conditions | Failure Modes | Yield line Moment-Applied load |
|---|--------|---------------------|---|---|
| Round Panel | 1.1 | Simply supported |  | $m = \frac{P}{2\pi}$ |
| | 1.2 | Clamped |  | $m = \frac{P}{4\pi}$ |
| Rectangular Panel | 2.1 | Simply supported |  | $m = \frac{qb^2(3b-a)}{12(2b+2a)}$ |
| | 2.2 | Clamped |  | $m = \frac{qb^2(3b-a)}{12(4b+4a)}$ |
| Square Panel | 3.1 | Simply supported |  | $m = \frac{qa^2}{24}$ |
| | 3.2 | Clamped |  | $m = \frac{qa^2}{48}$ |
| | | | | Moment Rotation |
|  | | → Clamped support |  |  |
|  | | → Simply supported |  |  |

3.5 Curvature-Deflection Relationship of Panels

Aswani, K derived the rotation-deflection relationship and curvature-deflection relationship for various types of panels [30]. Rotations that a slab undergoes at supports for certain deflections were calculated using the concepts of kinematics and geometry of slab. The derivation of curvature-deflection relationship of round panel is presented in this section as an example.

New concept of hinge length is imposed in here and several empirical equations of hinge length are presented. A slab under bending can be considered to consist of two distinct regions: the small hinge region where concrete crushing is visible, where wide flexural cracks occur, and where most of the permanent rotation is concentrated around the wide flexural cracks so that the trend of the moment distribution has little effect; and the non-hinge region which applies to most of the length so that it is affected by the trend of the moment distribution, where there are much narrower cracks, where, in particular, concrete crushing does not occur and where standard procedures of equilibrium can be applied [32][33].

Hinge length has been derived to be a function of span, depth or reinforcement [34]. Curvature is a measure of sectional ductility and rotation is a measure of member ductility. Product of sectional ductility (curvature) and hinge length gives the member ductility (rotation).

Many researchers have concentrated mainly on quantifying the hinge length, L^* empirically. Some suggested approaches are as shown in table below [34]:

Table 3.5- Empirically Derived Hinge Lengths

| Researcher reference | Hinge length (L^*) | Hinge length variables |
|----------------------|-------------------------|-----------------------------|
| Baker [35] | $k(z/d)^{1.4}d$ | Span (z), depth (d) |
| Sawyer [36] | $0.25d+0.075z$ | Span, depth |
| Corley [37] | $0.5d+0.2(z/d)\sqrt{d}$ | Span, depth |
| Mattock [38] | $0.5d+0.05z$ | Span, depth |

3.5.1 Case Study 1 – Curvature – Deflection Relationship for a Round Panel

Assume a round slab with radius R for with yield lines are originating at the center and extending till the boundary of the slab as shown in the Figure 3.5.1 below and maximum deflection occurs at that center [Error! Bookmark not defined.].

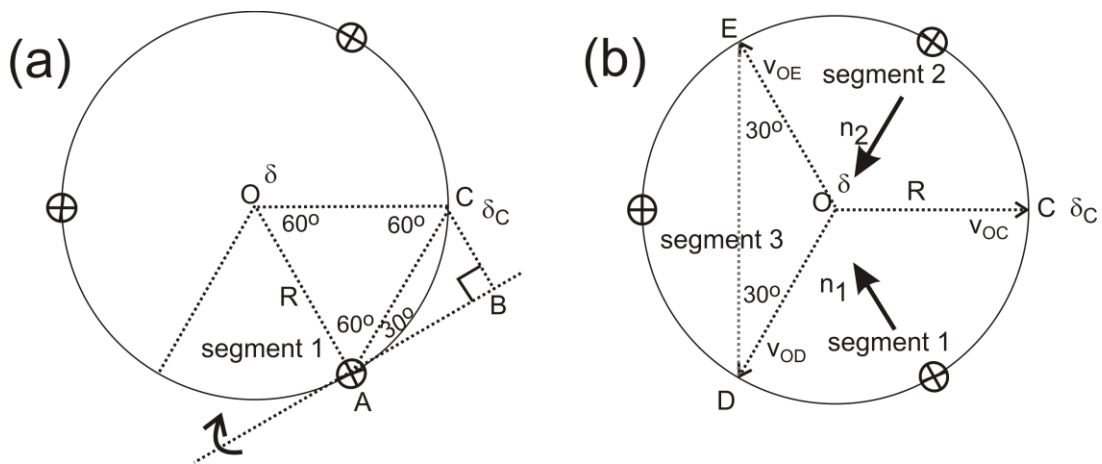


Figure 3.5.1 – Curvature-Deflection Relationship for Round Panel

From Figure 3.5.1 crack segment 1 rigidly rotate around the axis AB.

$$\frac{\delta_C}{\delta} = \frac{BC}{AO} = \frac{R \sin(30)}{R} = \frac{1}{2}$$

$$\delta_C = \frac{\delta}{2}$$

Thus, the deflection at the edge (point C) is half that of the center. Assume each crack segment is rigid and it rotates around the crack axis represented by vectors \overline{OC} , \overline{OD} and \overline{OE} as shown in Fig. 3.2.

$$\overline{OC} = (R, 0, 0.5\delta)$$

$$\overline{OD} = (-R\sin(30), -R\cos(30), 0.5\delta)$$

$$\overline{OE} = (-R\sin(30), R\cos(30), 0.5\delta)$$

The vectors normal to crack segment 1 and 2 can be found by cross product of the two adjacent vectors.

$$n_1 = \overline{OD} \times \overline{OC} = \left\{ -\frac{\sqrt{3}}{4} R\delta, \frac{3}{4} R\delta, \frac{\sqrt{3}}{2} R^2 \right\} \quad (3.5.1)$$

$$n_2 = \overline{OC} \times \overline{OE} = \left\{ -\frac{\sqrt{3}}{4} R\delta, -\frac{3}{4} R\delta, \frac{\sqrt{3}}{2} R^2 \right\} \quad (3.5.2)$$

The angle of curvature φ between segment 1 and 2 is the angle between these two normal vectors, determined by the dot product.

$$\varphi = \frac{1}{L^*} \cos^{-1} \left\{ \frac{n_1 \cdot n_2}{|n_1| |n_2|} \right\} = \frac{1}{L^*} \cos^{-1} \left\{ \frac{-\delta^2 + 2R^2}{2(\delta^2 + R^2)} \right\} \quad (3.5.3)$$

Deflection in terms of curvature can be simplified as:

$$\delta = \sqrt{\frac{2R^2(1 - \cos \varphi L^*)}{(1 + 2 \cos \varphi L^*)}} \quad (3.5.4)$$

3.5.2 Case Study 2 – Curvature – Deflection Relationship for a Rectangular Panel

Let us assume a rectangular slab with length a and breadth b for which yield lines are at 45° to the sides and meet at points as show in the Figure 3.5.2 below and maximum deflection occurs at that point.

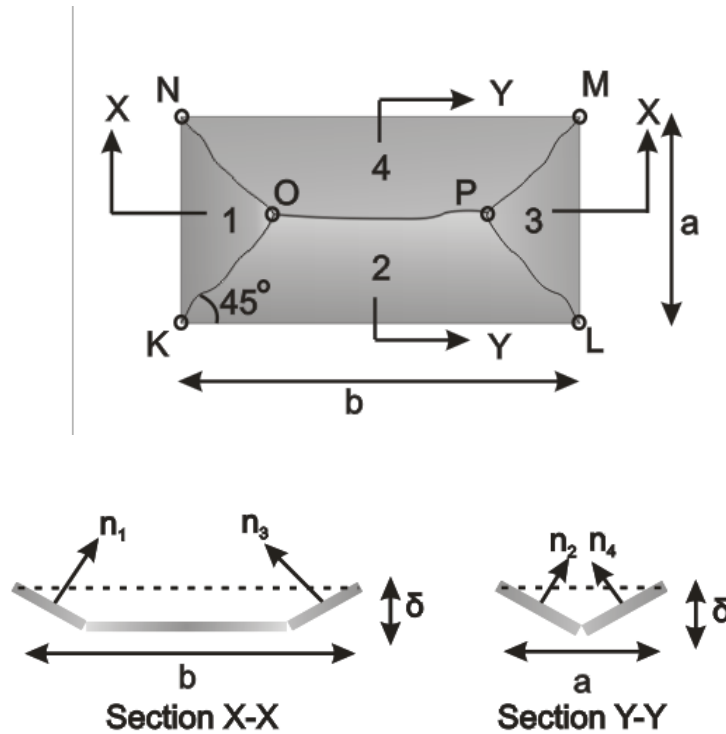


Figure 3.5.2 - Curvature-Deflection Relationship for Rectangular Panel

To find the angle of rotation, we first find the angle at center between two surfaces.

Curvature, ϕ and angle between the planes, 2θ can then be related as $\phi = \frac{1}{L^*} \left[\frac{\pi}{2} - \theta \right]$. For

finding the angles between both surfaces we find the angle that the normal to these surfaces make with each other.

First we find the angle between planes 1 and 3. This is similar to the case of square slab. As we obtain the results we see that deflection expression is same as that obtained for square slab of dimension b.

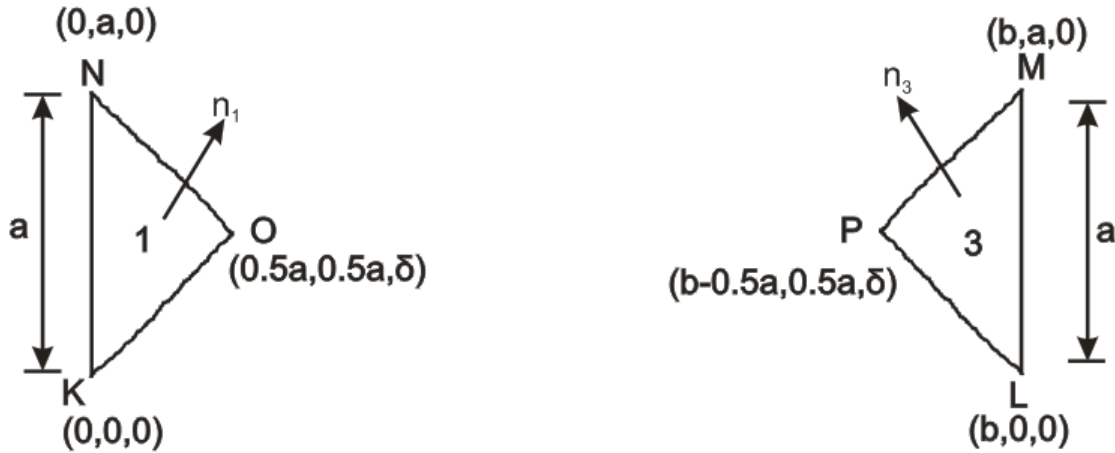


Figure 3.5.3 - Planes KON and PLM

For plane # 1 (KON), normal n_1 is obtained by the cross product of vectors \overline{KO} and \overline{KN} .

$$\overline{KO} = (0.5a, 0.5a, \delta)$$

$$\overline{KN} = (0, a, 0)$$

$$\vec{n}_1 = \overline{KO} \times \overline{KN} = \begin{vmatrix} \hat{i} & \hat{j} & \hat{k} \\ 0.5a & 0.5a & \delta \\ 0 & a & 0 \end{vmatrix} = -a\delta\hat{i} + 0.5a^2\hat{k}$$

Equation of the plane # 1 is given as-

$$\begin{aligned} -a\delta(x-0) + 0(y-0) + 0.5a^2(z-0) &= 0 \\ (a\delta)x - (0.5a^2)z &= 0 \end{aligned} \tag{3.5.5}$$

For plane # 3 (PLM), the normal n_3 is obtained by the cross product of vectors \overline{LP} & \overline{LM}

$$\overline{LP} = (-0.5a, 0.5a, \delta)$$

$$\overline{LM} = (0, a, 0)$$

$$\vec{n}_2 = \overline{LP} \times \overline{LM} = \begin{vmatrix} \hat{i} & \hat{j} & \hat{k} \\ -0.5a & 0.5a & \delta \\ 0 & a & 0 \end{vmatrix} = (-a\delta)\hat{i} + (-0.5a)a\hat{k}$$

Equation of the plane # 3 is given as

$$\begin{aligned} -a\delta(x-b) + 0(y-0) + (-0.5a)a(z-0) &= 0 \\ (a\delta)x + (0.5a^2)z - ab\delta &= 0 \end{aligned} \quad (3.5.6)$$

So the angle between two planes under yielding is given as-

$$\cos 2\theta_{13} = \cos(\pi - 2\varphi_{13}L^*) = \left(\frac{a^2\delta^2 - 0.25a^4}{\sqrt{(a^2\delta^2 + 0.25a^4)}\sqrt{(a^2\delta^2 + 0.25a^4)}} \right) = \frac{4\delta^2 - a^2}{4\delta^2 + a^2}$$

Deflection in terms of curvature can be simplified as:

$$\delta = \frac{a}{2} \sqrt{\frac{1 - \cos 2\varphi_{13}L^*}{1 + \cos 2\varphi_{13}L^*}} \quad (3.5.7)$$

It is known by symmetry that $\varphi_{13} = \varphi_{24}$

Similarly, we find the angle between planes 1 and 4 by the same procedure –

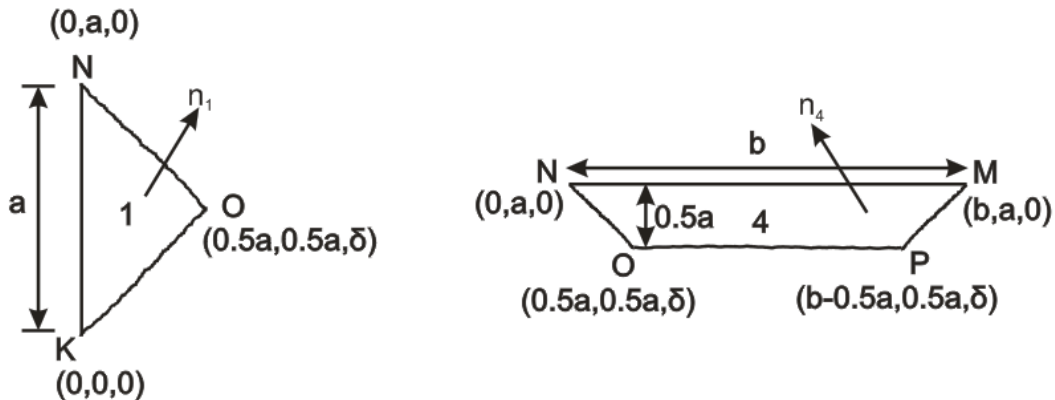


Figure 3.5.4 - Planes KON and NOPM

For plane # 1 (KON), the normal n_1 by the cross product between the vectors \overline{KO} & \overline{KN}

$$\overline{KO} = (0.5a, 0.5a, \delta)$$

$$\overline{KN} = (0, a, 0)$$

$$\vec{n}_1 = \overline{KO} \times \overline{KN} = \begin{vmatrix} \hat{i} & \hat{j} & \hat{k} \\ 0.5a & 0.5a & \delta \\ 0 & b & 0 \end{vmatrix} = (-a\delta)\hat{i} + \frac{a^2}{2}\hat{k}$$

Equation of the plane # 1 is given as

$$\begin{aligned} -a\delta(x-0) + 0(y-0) + 0.5a^2(z-0) &= 0 \\ (a\delta)x - 0.5a^2z &= 0 \end{aligned} \quad (3.5.8)$$

For plane # 4 (NOPM), the normal n_4 is the cross product of vectors \overline{NO} and \overline{NM}

$$\overline{NO} = (-0.5a, 0.5a, -\delta)$$

$$\overline{NM} = (-b, 0, 0)$$

$$\vec{n}_4 = \overline{NO} \times \overline{NM} = \begin{vmatrix} \hat{i} & \hat{j} & \hat{k} \\ -0.5a & 0.5a & -\delta \\ -b & 0 & 0 \end{vmatrix} = (b\delta)\hat{j} + (0.5ab)\hat{k}$$

Equation of the plane # 4 is given as

$$b\delta(y-a) + (-0.5b)a(z-0) = 0$$

$$(b\delta)y + (0.5ab)z - ab\delta = 0$$

So the angle between two planes under yielding is given as-

$$\begin{aligned} \cos 2\theta_{14} = \cos(\pi - 2\varphi_{14}L^*) &= \left(\frac{-0.25ba^3}{\sqrt{(a^2\delta^2 + 0.25a^4)}\sqrt{(b^2\delta^2 + 0.25b^2a^2)}} \right) = \frac{-a^2}{4\delta^2 + a^2} \\ \varphi_{14} &= \frac{1}{2L^*} \cos^{-1} \left[\frac{b^2}{4\delta^2 + b^2} \right] \end{aligned} \quad (3.5.9)$$

Deflection in terms of curvature can be simplified as:

$$\delta = \frac{a}{2} \sqrt{\frac{1 - \cos 2(\varphi_{14}L^*)}{\cos 2(\varphi_{14}L^*)}} \quad (3.5.10)$$

By the geometry of slab we know that $\varphi_{12} = \varphi_{14} = \varphi_{23} = \varphi_{34}$.

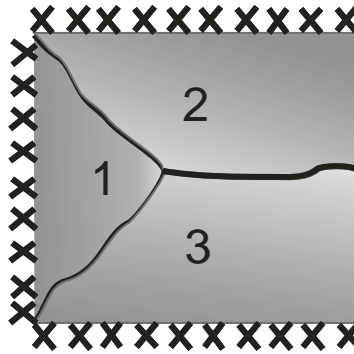


Figure 3.5.5 - Rectangular Slab Fixed from 3 Sides and Free from Fourth

For a two-way slab supported on 3 sides and free on fourth, the deflection-curvature relationship will remain unchanged and will be equal to equation 2-26.

3.5.3 Case Study 2 – Curvature – Deflection Relationship for a Rectangular Panel

Let us assume a square slab with side L for which yield lines are at 45° to the sides and meet at center and maximum deflection, δ also occurs at center.

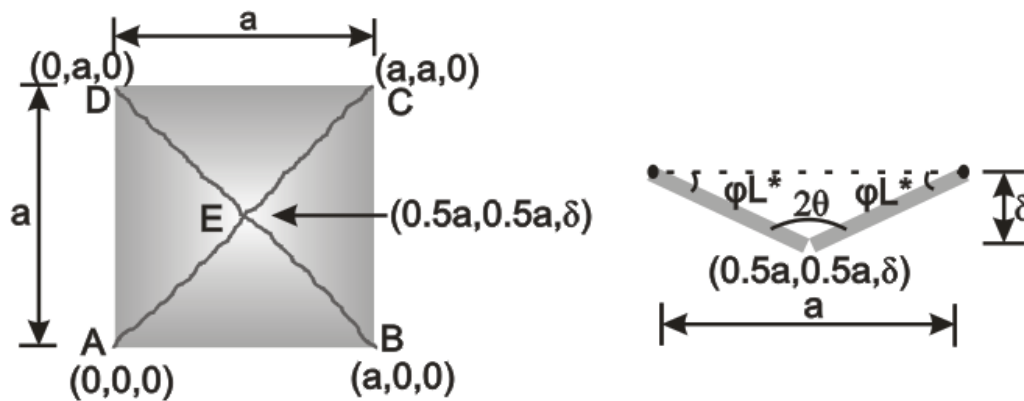


Figure 3.5.6 - Curvature-Deflection Relationship for Square Panel

To find the angle of rotation, we first find the angle at center between two surfaces.

Curvature, ϕ and angle between the planes, 2θ can then be related as $\phi = \frac{1}{L^*} \left[\frac{\pi}{2} - \theta \right]$

where L^* is the hinge length and ϕL^* is the rotation. For finding the angles between both surfaces we find the angle that the normal to these surfaces make with each other.

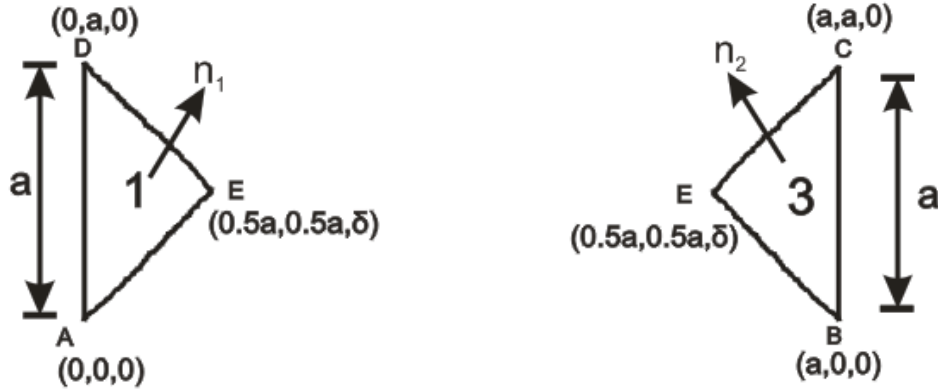


Figure 3.5.7 Planes AED and EBC

For plane # 1 (AED), the normal n_1 is the cross product of vectors \overline{AE} and \overline{AD} .

$$\overline{AE} = (0.5a, 0.5a, \delta)$$

$$\overline{AD} = (0, a, 0)$$

$$\vec{n}_1 = \overline{AE} \times \overline{AD} = \begin{vmatrix} \hat{i} & \hat{j} & \hat{k} \\ 0.5a & 0.5a & \delta \\ 0 & a & 0 \end{vmatrix} = (-a\delta)\hat{i} + 0.5a^2\hat{k}$$

Equation of the plane # 1 is given as

$$\begin{aligned} -a\delta(x-0) + 0(y-0) + 0.5a^2(z-0) &= 0 \\ (a\delta)x - 0.5a^2z &= 0 \end{aligned} \tag{3.5.11}$$

For plane # 3 (BCE), the normal n_2 is the cross product of vectors \overline{BE} and \overline{BC} .

$$\overline{BE} = (-0.5a, 0.5a, \delta)$$

$$\overline{BC} = (0, -a, 0)$$

$$\vec{n}_2 = \overline{BE} \times \overline{BC} = \begin{vmatrix} \hat{i} & \hat{j} & \hat{k} \\ -0.5a & 0.5a & \delta \\ 0 & a & 0 \end{vmatrix} = (-a\delta)\hat{i} - 0.5a^2\hat{k}$$

Equation of the plane # 3 is given as

$$\begin{aligned} -a\delta(x-a) + 0(y-0) - 0.5a^2(z-0) &= 0 \\ (a\delta)x + 0.5a^2z - a^2\delta &= 0 \end{aligned} \quad (3.5.12)$$

The angle between planes is the angle between their normal vectors. If $A_1x + B_1y + C_1z + D_1 = 0$ and $A_2x + B_2y + C_2z + D_2 = 0$ are plane equations, then angle between planes can be found using the following formula:

$$\alpha = \cos^{-1} \left(\frac{|A_1.A_2 + B_1.B_2 + C_1.C_2|}{(A_1^2 + B_1^2 + C_1^2)^{1/2} (A_2^2 + B_2^2 + C_2^2)^{1/2}} \right)$$

So the angle between two planes under yielding is given as:

$$\begin{aligned} \cos 2\theta = \cos(\pi - 2\varphi L^*) &= \frac{a^2\delta^2 - 0.25a^4}{\sqrt{(a^2\delta^2 + 0.25a^4)}\sqrt{(a^2\delta^2 + 0.25a^4)}} = \frac{4\delta^2 - a^2}{4\delta^2 + a^2} \\ \varphi &= \frac{1}{2L^*} \cos^{-1} \left(\frac{-4\delta^2 + a^2}{4\delta^2 + a^2} \right) \end{aligned} \quad (3.5.13)$$

Deflection- curvature relationship is given as:

$$\delta = \frac{a}{2} \sqrt{\frac{1 - \cos 2\varphi L^*}{1 + \cos 2\varphi L^*}} \quad (3.5.14)$$

Where δ is the deflection, φ is the curvature, L^* is the hinge length and L is the dimension of the slab.

Table 3.5.1 Summary of Relationship between Curvature and Deflection for Panels

| Type of Panel | Curvature- Deflection |
|--|---|
| Round | $\delta = \sqrt{\frac{2R^2(1 - \cos \varphi L^*)}{(1 + 2 \cos \varphi L^*)}}$ |
| Rectangle (yield lines are at 45°, two-way) | $\delta = \frac{a}{2} \sqrt{\frac{1 - \cos 2(\varphi L^*)}{\cos 2(\varphi L^*)}}$ |
| Square (yield lines are at 45°) | $\delta = \frac{a}{2} \sqrt{\frac{1 - \cos 2\varphi L^*}{1 + \cos 2\varphi L^*}}$ |

3.6 Bilinear Moment-Curvature Relationship for Panel

A simplified parametric moment curvature response is represented by a bilinear function in elastic pre-cracked and post-cracked stages as shown in Figure 3.6.1 and Figure 3.6.2. The elastic stage extends to the onset of first flexural crack. The second stage follows until the ultimate flexural capacity which corresponds to the ultimate state. The difference between this model with the moment-curvature diagram discussed in Section 2.1 is the flexural behavior after the cracking point. There are two type of behavior, one is the strain-hardening behavior with the stiffness ratio η as a positive number (dash line in Figure 3.6.1 and 3.6.2) , another one is the strain-softening behavior when the η is negative number (solid line in Figure 3.6.1 and 3.6.2) The bilinear elastic post-cracking moment-curvature response is fully defined by two control points (M_{cr}, φ_{cr}) and (M_u, φ_u) and expressed as:

$$\begin{aligned}
 M(\varphi) &= EI_g \varphi & 0 < M \leq M_{cr} & & 0 < \varphi \leq \varphi_{cr} \\
 M(\varphi) &= \frac{M_u - M_{cr}}{\varphi_u - \varphi_{cr}} (\varphi - \varphi_{cr}) + M_{cr} & 1 \leq \varphi \leq \varphi_u & &
 \end{aligned} \tag{3.6.1}$$

First cracking moment and first cracking curvature defined as:

$$M_{cr} = \frac{1}{6}bd^2E\varepsilon_{cr} \quad \varphi_{cr} = \frac{2\varepsilon_{cr}}{d} \quad (3.6.2)$$

Equation (3.1) can be presented in normalized form by introducing two normalizing constants as

$$\begin{aligned} m'(q') &= q' & 0 < m' \leq 1 \quad 0 < q' \leq 1 \\ m'(q') &= \frac{m-1}{q-1}(q'-1)+1 & q' \geq 1 \end{aligned} \quad (3.6.3)$$

The parameter based moment curvature relationships are therefore:

$$m'(q') = \frac{M'(\varphi)}{M_{cr}}; \quad q' = \frac{\varphi_i}{\varphi_{cr}} \quad m = \frac{M_u}{M_{cr}}; \quad q = \frac{\varphi_u}{\varphi_{cr}}, \quad \eta = \frac{EI_{cr}}{EI_g} \quad (3.6.4)$$

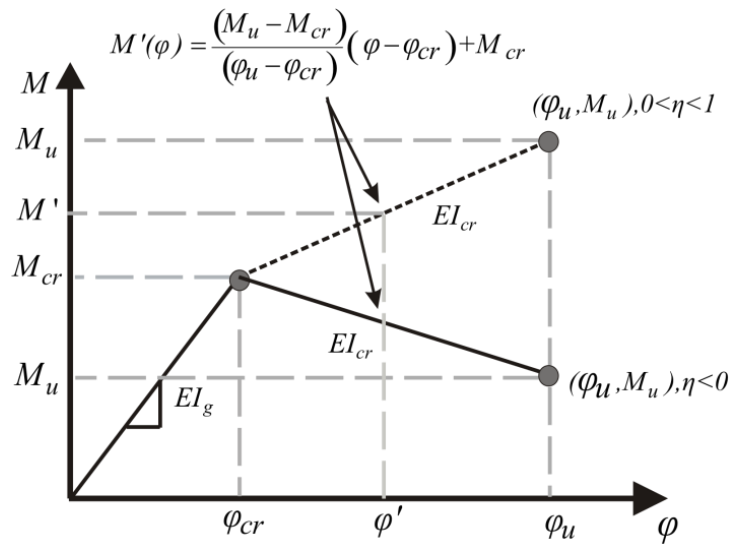


Figure 3.6.1 - Bilinear Moment-Curvature Relationship for Panels

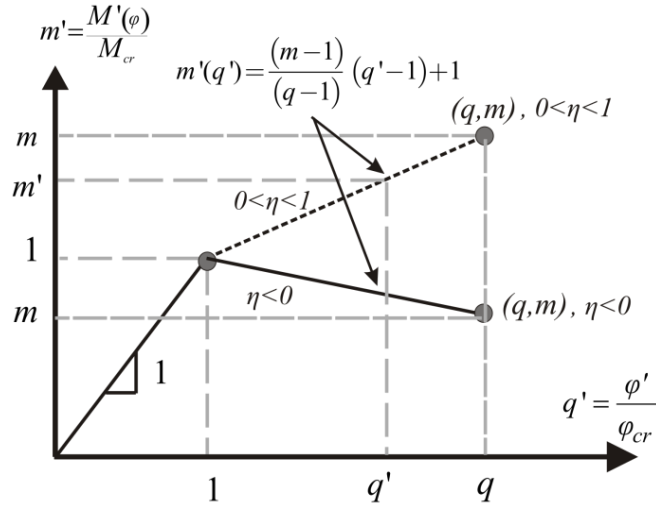


Figure 3.6.2 - Normalized Moment-Curvature Curve Represented as (q', m')

3.7 Experimental Verification

3.7.1 Algorithm to Predict Load-Deflection Response

Algorithm to predict the load deflection response of panel based on the simplified bilinear moment-curvature model is divided into two stages, which are pre-cracking stage and post-cracked stage. The elastic solutions present in Section 1 are implemented in the pre-cracking stage and the solution of yield line presented in Section 3.2 is used in the post-cracked stage. Using the simplified moment-curvature model (Section 3) one can approach the problem in the following manner:

- i. For a given cross section and material properties and calculated the cracking moment and cracking curvature using the Eq (3.6.2)
- ii. Assume the maximum normalized curvature q' , which is corresponding to ultimate stage. Select the discrete points of q' from the zero to the q'_{\max} and calculate the corresponding curvature ϕ' is calculated from Eq (3.6.4) and relative moment M' can be obtained from the relationship of moment-curvature for each q' .

- iii. Applying the yield line theory to find the magnitude of load with the transition point from pre-cracked stage to the post-cracked stage ($q'=1$).
- iv. Using the elastic solution to get the load-deflection response when the $q'<1$. In terms of the $q'>1$, a load vector is generated using the relationship between moment and load for the panel configurations as derived by the yield line methodology in section 2.2. The slab is segmented into finite sections and maximum deflection is calculated using the relationship between curvature and deflection as derived in section 2.3.

This procedure is applied at each step until a complete load deflection response is obtained for the corresponding moment curvature relationship.

3.7.2 Data Set 1

Four round plates were investigated according to the ASTM standard [39] by Kim, Jihwan, et al [40]. The dimensions of the plates are 420 mm in diameter and 48 mm in thickness (which are smaller than the dimensions recommended by the standard). The plates are supported by three symmetrically arranged hinged supports at 120° . The volume fraction of steel fiber is 1.5%. The responses of point load – deflection of center were simulated by the proposed algorithm of predicting the experimental data of panels. The simulated parameters used in the model are listed in the Table 3.7.1 and hinge length was assumed as 20 mm for all samples.

Table 3.7.1 - Simulated Parameters of Current Model for Data Set 1

| Sample# | ϵ_{cr} , 10^{-6} | E, GPa | η | m | q | M_{cr} , KN-mm | Φ_{cr} , $10^{-6}/mm$ | EI , 10^{11} | EI_{cr} , 10^8 |
|---------|--------------------------------|-----------|--------|------|-----|---------------------|-------------------------------|------------------|--------------------|
| 1 | 130 | 32 | 0.0033 | 1.95 | 290 | 639 | 5.42 | 1.18 | 3.89 |
| 2 | 130 | 32 | 0.004 | 2.00 | 250 | 639 | 5.42 | 1.18 | 4.72 |
| 3 | 135 | 32 | 0.004 | 2.04 | 260 | 663.6 | 5.62 | 1.18 | 4.72 |
| 4 | 135 | 32 | 0.005 | 2.34 | 270 | 663.6 | 5.62 | 1.18 | 5.90 |

Figure 3.7.1 shows the normalized moment-curvature relationships of the samples and Figure 3.7.2 shows the load-deflection responses. The blue solid line represents the simulated pre-cracked behavior which is generated by using the elastic equation of round panel (Section 3.2), however, the red dash line represents the post-cracked behavior generated by the yield line approach (Section 3.4 and 3.5). The transition point between these two stages is decided by the input moment-curvature relationship. Note that the stiffness ratio η is positive due to the deflection-hardening response after the first cracking point. It is obvious that the algorithm proposed can predict the pre-cracked load-deflection response perfectly and the prediction of the post-cracked response is underestimated. Trend of the post-cracked behaviors can also be obtained and the approximated post stiffness of both moment-curvature relationship and load-deflection response can be predicted.

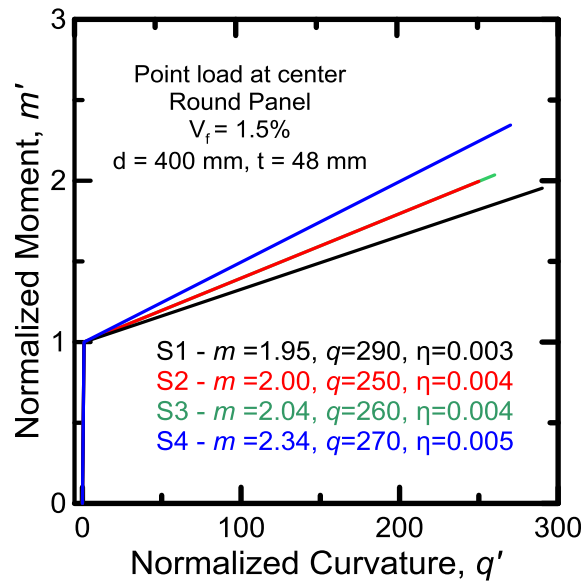


Figure 3.7.1- Normalized Moment-Curvature Relationship

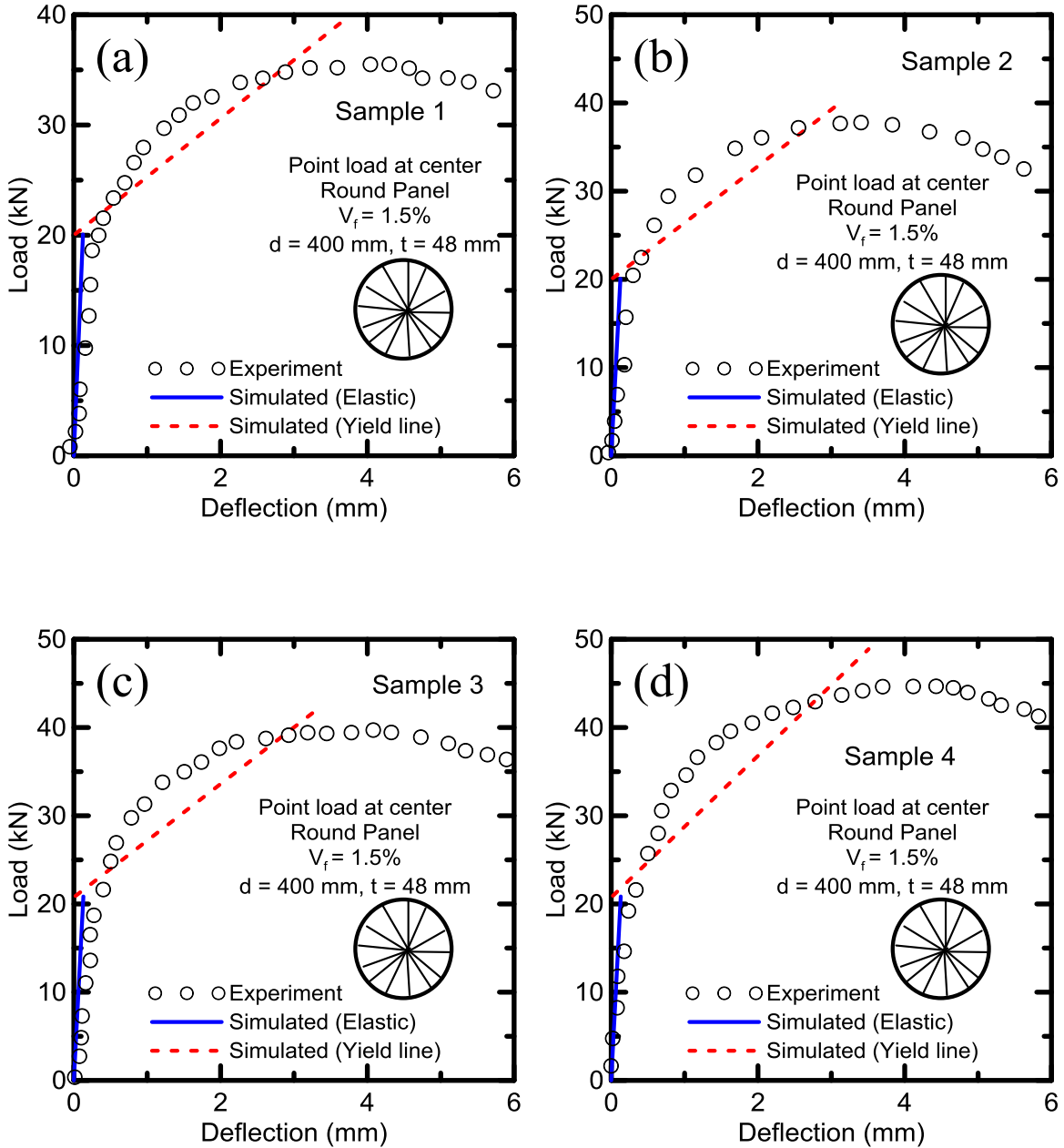


Figure 3.7.2 - Load-Deflection Responses of the Round Panel Samples

Figure 3.7.3 shows the effect of hinge length, L^* on the load-deflection response. From figure 3.7.3 it can be seen that the pre-cracked response does not effected by the assumed hinge length and the post cracked stiffness decreases with increasing the hinge length.

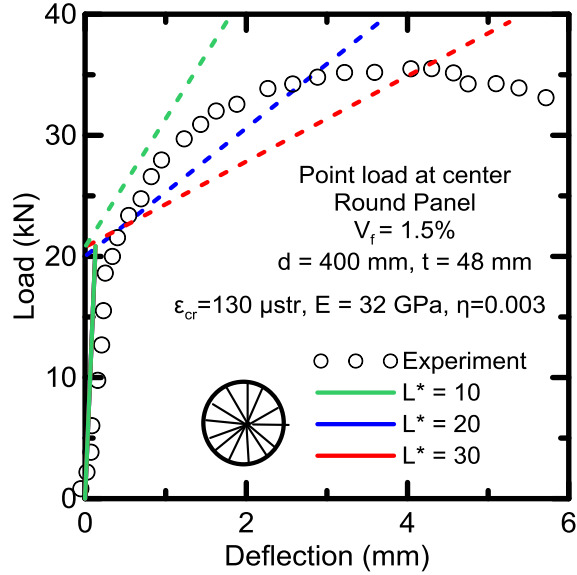


Figure 3.7.3 - Effect of Hinge Length on Simulated Results

3.7.3 Data Set 2

Two series of round plate were casted and tested according to the ASTM standard [39] by Xu, Hanfeng, et al [41]. One series of them were casted using steel fiber reinforced high strength concrete (HSC) with two different fiber volume fraction; 0.5% (SFRC05) and 1.0% (SFRC10). Another series specimen was casted using synthetic fiber HSC with fiber volume fraction of 0.5% (SYNFRC05) and 1.0% (SYNFRC10). The dimensions of the plates are 635 mm in diameter and 60 mm in thickness. The plates are supported by three symmetrically arranged hinged supports at 120° . The details of specimens are shown in Table 3.7.2. The average responses of load – deflection of center for each series were simulated by the proposed algorithm and the simulated parameters used in the model are listed in the Table 3.7.3 and hinge length was assumed as 32 mm for all samples.

Table 3.7.2- Details of Round Panel Specimens for Data Set 2

| ID | Diameter, mm | Thickness, mm | Fiber Type | V_f , % |
|--------|--------------|---------------|------------|-----------|
| SFRC05 | 635 | 60 | Steel | 0.5 |
| SFRC10 | 635 | 60 | Steel | 1.0 |
| SYNF10 | 635 | 60 | Synthetic | 0.5 |
| SYNF10 | 635 | 60 | Synthetic | 1.0 |

Table 3.7.3- Simulated Parameters of Current Model for Data Set 3

| ID | ϵ_{cr} , 10^{-6} | E, GPa | η | m | q | M_{cr} , KN-mm | Φ_{cr} , $10^{-6}/mm$ | EI , 10^{11} | EI_{cr} , 10^8 |
|--------|--------------------------------|-----------|---------|-------|------|---------------------|-------------------------------|---------------------|-----------------------|
| SFRC05 | 125 | 13 | -0.0008 | 0.026 | 1300 | 619 | 4.2 | 1.49 | 1.1 |
| SFRC10 | 135 | 18 | -0.0006 | 0.053 | 1580 | 926 | 4.5 | 2.06 | 1.2 |
| SYNF05 | 120 | 11 | -0.0005 | 0.10 | 1800 | 503 | 4.0 | 1.26 | 0.63 |
| SYNF10 | 130 | 16 | -0.0004 | 0.24 | 1800 | 768 | 4.3 | 1.77 | 0.74 |

Figure 3.7.3 shows the normalized moment-curvature relationship of the specimens and Figure 3.7.4 shows the load-deflection responses and the simulated curve generated by the current model. The solid line represents the simulated pre-cracked behavior which is generated by using the elastic equation of round panel; however, the dash line represents the post-cracked behavior generated by the yield line approach. The transition point between these two stages is decided by the assumed moment-curvature relationship. Note that the proposed model could not accurately predict the first cracking point and the prediction of the post-cracked responses slightly overestimated the experimental data, but the trend can be fitted perfectly. The stiffness ratio η is negative due to the deflection-softening response after the first cracking point. Figure 3.7.3(a) shows the normalized moment-curvature relationship of SFRC round panels and it is obvious that the elastic behaviors of the specimens with different volume fraction of fiber are similar. The post cracked stiffness and cracking moment of the panels with higher fiber content ($V_f=1\%$) is

slightly high than that of panels with lower fiber content ($V_f=0.5\%$) and resulted in the higher energy absorption with higher fiber content. The same conclusion can be derived from the Figure 2(b) which is shows the normalized moment-curvature relationship of synthetic fiber reinforced round panels. It is obvious that the post cracked stiffness in terms of load-deflection response is slightly different with different fiber types. The panels with steel fiber reinforced have higher post-cracked stiffness, as shown in Table 3.7.3 and Figure 3.7.4.

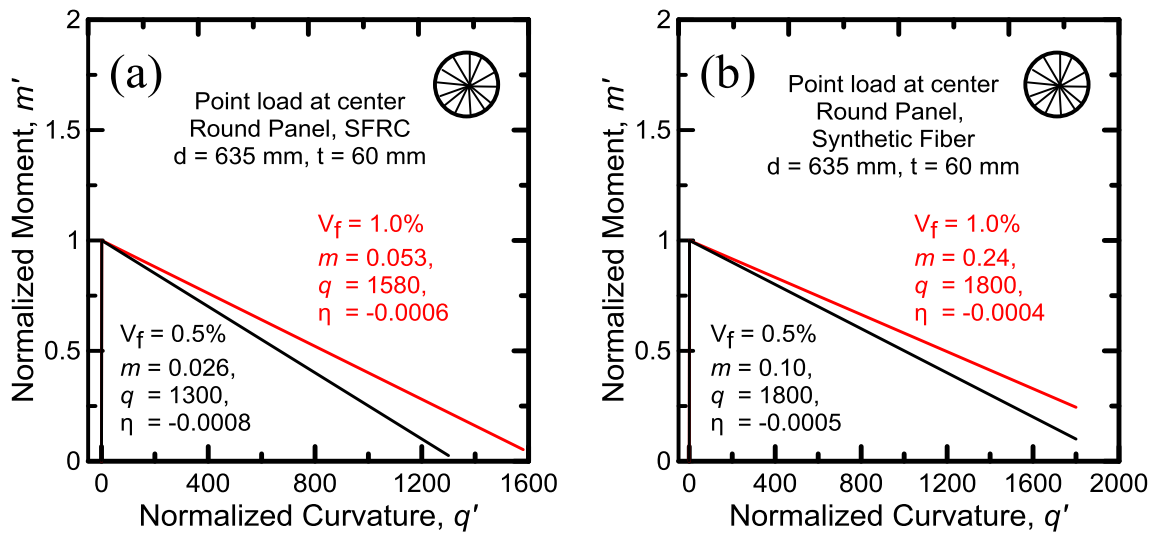


Figure 3.7.3 - Normalized Moment –Curvature Relationships of Round Panels; (a) SFRC;(b) Synthetic FRC

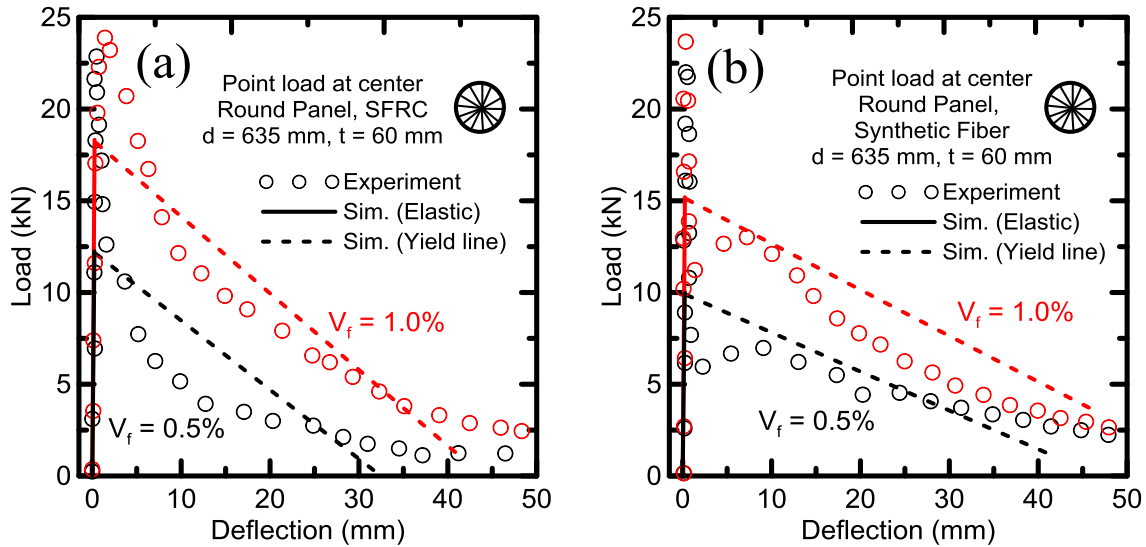


Figure 3.7.4 - Load-Deflection Responses of Round Panels; (a) SFRC;(b) Synthetic FRC

3.7.4 Data Set 3

Experimental results for fiber reinforced concrete square slabs are considered in a study published by Khaloo and Afshari here [42].two series of them were studied here for verifying the current model. The span of slabs is 680 mm x 680 mm with 80 mm thickness and subjected with the point load at center. The fiber used in this experiment is steel fiber but with two different shapes and named as fiber S25 and S35, separately; the shape properties are presented as Table 3.7.4. The variable investigated is fiber volumetric percentage with 1% and 1.5%. The details of the square slabs are shown in Table 3.7.5. The responses of point load – deflection of center for each series were simulated by the proposed algorithm. The simulated parameters used in the current model are listed in the Table3.7.5 and hinge length was assumed as 68 mm for all samples.

Table 3.7.4- Shape Properties of Steel Fibers for Data Set 3

| Fiber ID | Length, mm | Width, mm | Thickness, mm | Equivalent diameter, mm |
|----------|------------|-----------|---------------|-------------------------|
| S25 | 25 | 0.8 | 0.35 | 0.597 |
| S35 | 35 | 1 | 0.35 | 0.668 |

Table 3.7.5- Details of Round Panel Specimens for Data Set 3

| Specimen ID | Length of side, mm | Thickness, mm | Fiber ID | V_f , % |
|-------------|--------------------|---------------|----------|-----------|
| S25-1 | 680 | 80 | S25 | 1.0 |
| S25-2 | 635 | 80 | S25 | 1.5 |
| S35-1 | 635 | 80 | S35 | 1.0 |
| S35-2 | 635 | 80 | S35 | 1.5 |

Figure 3.7.5 shows the normalized moment-curvature relationship of the specimens and it is obvious that the elastic behaviors of the specimens with different volume fraction of fiber are similar. Figure 3.7.6 shows the load-deflection responses and the simulated curve generated by the algorithm. The solid line represents the simulated pre-cracked behavior which is generated by using the elastic equation of square panel. The dash line represents the post-cracked behavior generated by the yield line approach. The transition point between these two stages is decided by the input assumed moment-curvature relationship. Note that the proposed model could not accurately catch the first cracking point in terms of load-deflection response and the predictions of post-cracked responses slightly overestimates the experimental data.

Table 3.7.6- Simulated Parameters of Current Model for Data Set 3

| Sample# | ϵ_{cr} , 10^{-6} | E, GPa | η | m | q | M_{cr} , KN-mm | Φ_{cr} , $10^{-6}/mm$ | EI , 10^{11} | EI_{cr} , 10^8 |
|---------|--------------------------------|-----------|---------|-------|-----|---------------------|-------------------------------|------------------|--------------------|
| 1 | 100 | 7.5 | -0.003 | 0.043 | 320 | 544 | 2.5 | 2.18 | 6.5 |
| 2 | 110 | 9 | -0.0025 | 0.040 | 385 | 718 | 2.75 | 2.61 | 6.5 |
| 3 | 110 | 7 | -0.0035 | 0.024 | 280 | 558500 | 2.75 | 2.03 | 7.1 |
| 4 | 110 | 9.5 | -0.0024 | 0.043 | 400 | 758000 | 2.75 | 2.76 | 6.6 |

The toughness of the panels with higher fiber content ($V_f=1.5\%$) is higher than that of panels with lower fiber content ($V_f=1\%$) since the higher cracking moment and equal post stiffness of specimen with higher fiber content. The stiffness ratio η is negative due to the deflection-softening response after the first cracking point. It is obvious that there has little difference of post-cracked stiffness in terms of load-deflection responses between the two series of specimen since both fibers are steel even the shapes of fiber are slightly different.

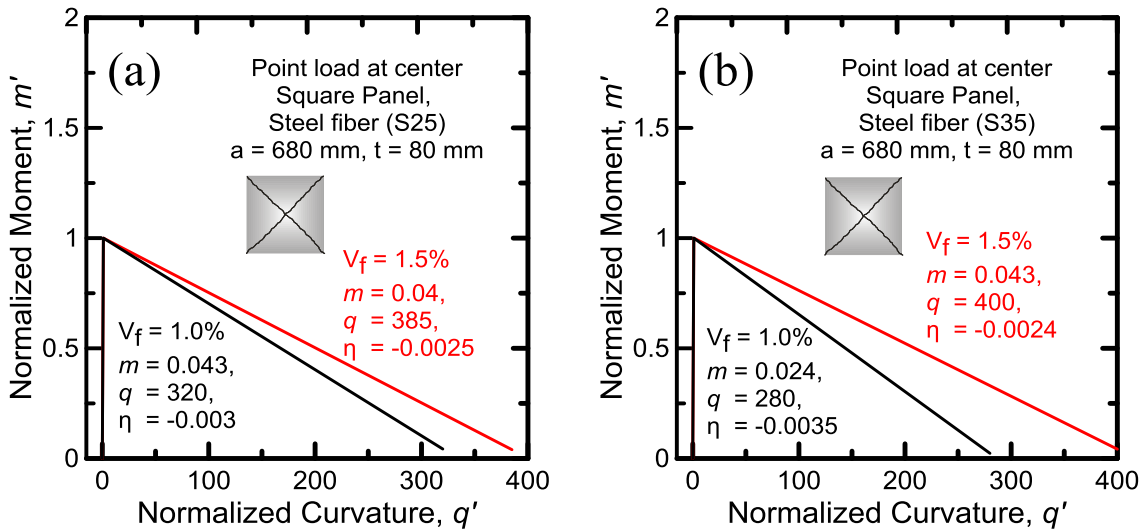


Figure 3.7.5 - Normalized Moment –Curvature Relationships of Square Panels; (a) Steel Fiber with Length of 25 mm;(b) Steel Fiber with Length of 35 mm

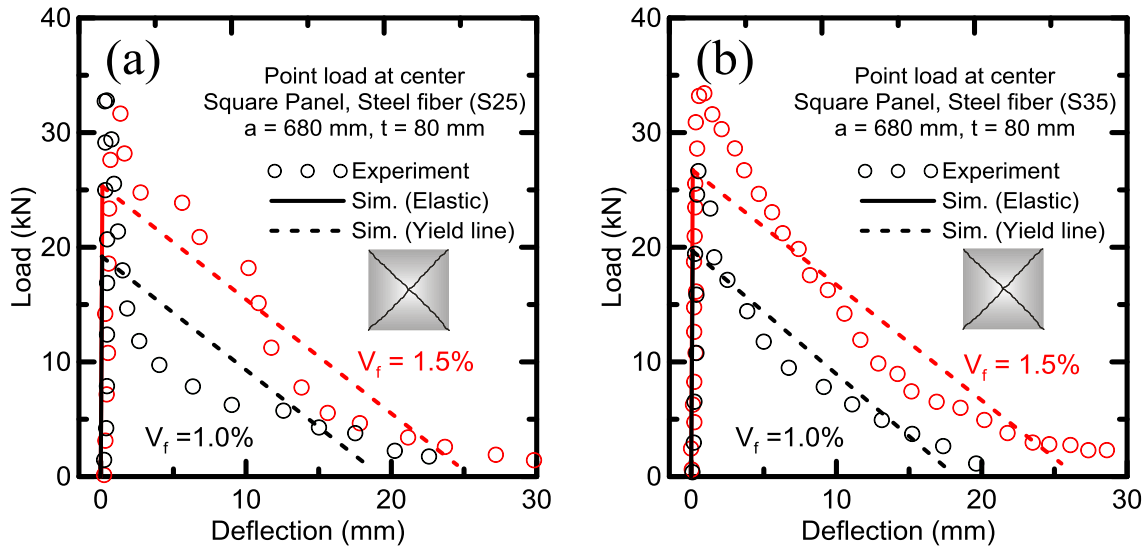


Figure 3.7.6 - Load-Deflection Responses of Square Panels; (a) Steel Fiber with Length of 25 mm;(b) Steel Fiber with Length of 35 mm

3.7.5 Data Set 4

Two series of round plate specimens were casted and tested according to the ASTM standard by de Montaignac, Renaud, et al [43]. Two types of hooked-end fibers: the RC80/60 fibers (60 x 0.75 mm) and the RC65/35 fibres (35 x 0.55 mm). Three fibre dosages were selected: 0.75, 1.0 and 1.25% in volume. The dimensions of the plates are 750 mm in diameter and 80 mm in thickness. The plates are supported by three symmetrically arranged hinged supports at 120° and the point load subjected at the center of the panels. The details of beam are shown in Table 3.7.7. The responses of point load – deflection of center for each specimen were simulated by the proposed and the simulated parameters used in the model are listed in the Table 3.7.8 and hinge length was assumed as 38 mm for all samples.

Table 3.7.7- Details of Round Panel Specimens for Data Set 4

| ID | Diameter, mm | Thickness, mm | Fiber Type | V_f , % |
|-------|--------------|---------------|------------|-----------|
| F60-1 | 750 | 80 | RC80/60 | 0.75 |
| F60-2 | 750 | 80 | RC80/60 | 1.0 |
| F35-1 | 750 | 80 | RC65/35 | 1.0 |
| F35-2 | 750 | 80 | RC65/35 | 1.25 |

Table 3.7.8- Simulated Parameters of Current Model for Data Set 4

| Sample# | ϵ_{cr} , 10^{-6} | E, GPa | η | m | q | M_{cr} , KN-mm | Φ_{cr} , $10^{-6}/mm$ | EI , 10^{11} | EI_{cr} , 10^8 |
|---------|-----------------------------|--------|---------|------|-----|------------------|----------------------------|------------------|--------------------|
| F60-1 | 135 | 20 | -0.0008 | 0.32 | 900 | 2160 | 3.38 | 6.4 | 4.80 |
| F60-2 | 135 | 22 | -0.0006 | 0.46 | 900 | 2376 | 3.38 | 7.0 | 4.22 |
| F35-1 | 130 | 20 | -0.0007 | 0.34 | 950 | 2080 | 3.25 | 6.4 | 4.48 |
| F35-2 | 135 | 21 | -0.0008 | 0.24 | 950 | 2268 | 3.38 | 6.7 | 5.38 |

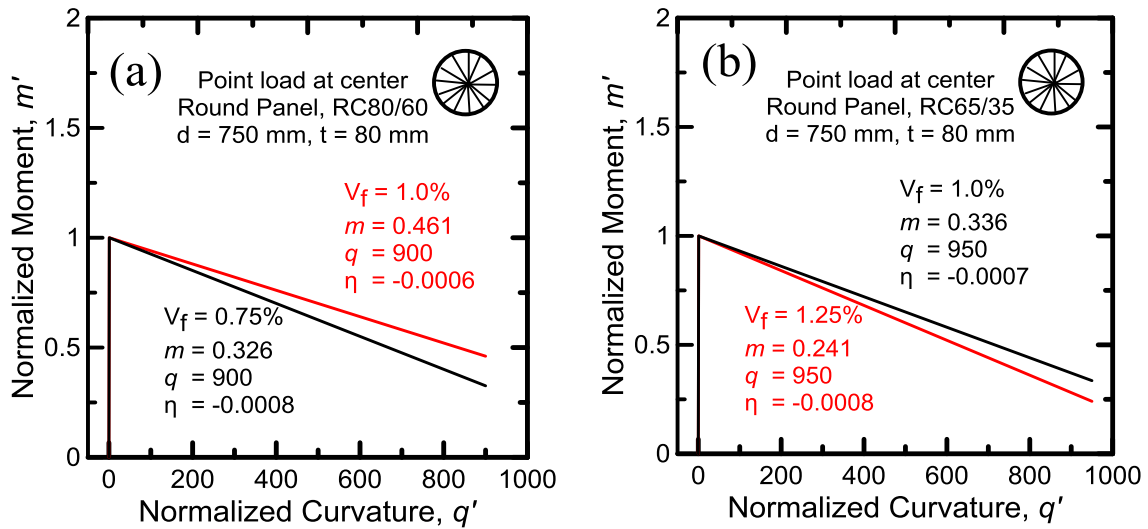


Figure 3.7.7 - Normalized Moment –Curvature Relationships of Round Panels; (a) RC80/60 with Two Levels of Fiber Content; (b) RC65/35 with Two Levels of Fiber Content

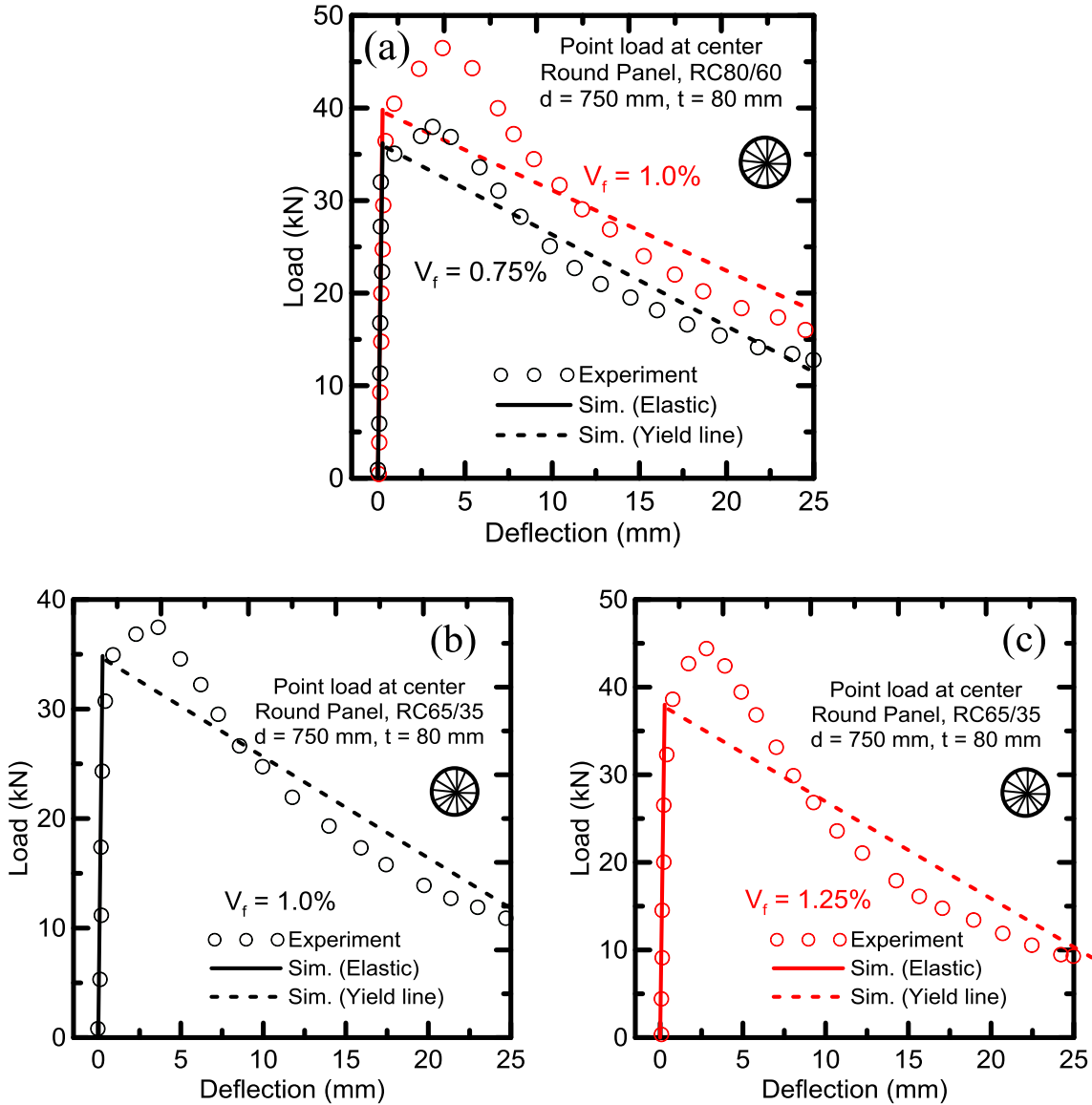


Figure 3.7.8 - Load-Deflection Response of Round Panels; (a) RC80/60 with Two Levels of Fiber Content;(b) RC65/35, $V_f=1.0\%$; (c) RC65/35, $V_f=1.25\%$

Figure 3.7.7 shows the normalized moment-curvature relationship of the specimens and Figure 3.7.8 shows the load-deflection responses and the simulated curve generated by the current model. The solid line represents the simulated pre-cracked behavior and the dash line represents the post-cracked behavior generated by the yield line approach. Note that the proposed model could not accurately predict the first cracking point and the prediction the post-cracked responses generally underestimates the experimental data. Figure 3.7.8 shows the toughness of the panels with higher fiber content is slightly high

than that of panels with lower fiber content, which means the more energy can be absorbed with higher fiber content.

4. REFERENCES

1. Ombres, Luciano. "Structural performances of reinforced concrete beams strengthened in shear with a cement based fiber composite material." *Composite Structures* 122 (2015): 316-329.
2. Brückner, A., R. Ortlepp, and M. Curbach. "Textile reinforced concrete for strengthening in bending and shear." *Materials and structures* 39.8 (2006): 741-748.
3. Triantafillou, Thanasis C., and Catherine G. Papanicolaou. "Shear strengthening of reinforced concrete members with textile reinforced mortar (TRM) jackets." *Materials and structures* 39.1 (2006): 93-103.
4. Blanksvärd, Thomas, and Björn Täljsten. "Strengthening of concrete structures with cement based bonded composites." *Journal of Nordic Concrete Research* 38.2 (2008): 133-153.
5. Banthia, Nemkumar, and Jean-Francois Trottier. "Test Methods for Flexural Toughness Characterization of Fiber Reinforced Concrete: Some Concerns and a Proposition." *ACI Materials Journal* 92.1 (1995).
6. Alhozaimy, A. M., P. Soroushian, and F. Mirza. "Mechanical properties of polypropylene fiber reinforced concrete and the effects of pozzolanic materials." *Cement and Concrete Composites* 18.2 (1996): 85-92.
7. Song, P. S., and S. Hwang. "Mechanical properties of high-strength steel fiber-reinforced concrete." *Construction and Building Materials* 18.9 (2004): 669-673.
8. Sahoo, Dipti Ranjan, and Abhimanyu Sharma. "Effect of steel fiber content on behavior of concrete beams with and without stirrups." *ACI Structural Journal* 111.5 (2014).
9. Harris, Harry G., Win Somboonsong, and Frank K. Ko. "New ductile hybrid FRP reinforcing bar for concrete structures." *Journal of Composites for Construction* 2.1 (1998): 28-37.
10. Mechtcherine, Viktor. "Novel cement-based composites for the strengthening and repair of concrete structures." *Construction and Building Materials* 41 (2013): 365-373.
11. Larbi, Amir Si, Amen Agbossou, and Patrice Hamelin. "Experimental and numerical investigations about textile-reinforced concrete and hybrid solutions for

- repairing and/or strengthening reinforced concrete beams." *Composite Structures* 99 (2013): 152-162.
12. Brückner, A., R. Ortlepp, and M. Curbach. "Textile reinforced concrete for strengthening in bending and shear." *Materials and structures* 39.8 (2006): 741-748.
 13. Naaman, A. E., and H. W. Reinhardt. "Proposed classification of HPFRC composites based on their tensile response." *Materials and structures* 39.5 (2006): 547-555.
 14. Soranakom C, Mobasher B. Correlation of tensile and flexural response of strain softening and strain hardening cement composites. *Cem Concr Compos*, 2008;30:465-477.
 15. Mobasher, *Mechanics of Textile and Fiber reinforced cement composites*, CRC press, 470 p, 2011.
 16. Soranakom C, Mobasher B. Correlation of tensile and flexural response of strain softening and strain hardening cement composites. *Cem Concr Compos*;30:465-477, 2008.
 17. Sueki, S., Soranakom, C., Peled, A., and Mobasher, B. (2007), "Pullout–slip response of fabrics embedded in a cement paste matrix," *ASCE Journal of Materials in Civil Engineering*, 19, 9.
 18. Barros, Joaquim AO, et al. "Flexural behavior of reinforced masonry panels." *American Concrete Institute*, 2006. (12_Yiming's paper)
 19. Kwak, Hyo-Gyoung, and Sun-Pil Kim. "Nonlinear analysis of RC beams based on moment–curvature relation." *Computers & structures* 80.7 (2002): 615-628.
 20. Lim, T. Y., P. Paramisivam, and S. L. Lee. "Bending behavior of steel-fiber concrete beams." *ACI Structural Journal* 84.6 (1987).
 21. Soranakom C., Mobasher B., "Correlation of tensile and flexural responses of strain softening and strain hardening cement composites", *Cement & Concrete Composites* 30 465–477, 2008
 22. Soranakom C., Mobasher B. , "Closed-Form Solutions for Flexural Response of Fiber-Reinforced Concrete Beams" *ASCE* 0733-9399/2007/133:8933.
 23. Mobasher, Barzin, et al. "Correlation of constitutive response of hybrid textile reinforced concrete from tensile and flexural tests." *Cement and Concrete Composites* 53 (2014): 148-161.

24. Minelli F., Conforti A., Cuenca E., Plizzari G., “Are steel fibres able to mitigate or eliminate size effect in shear?”, *Materials and Structures* , 47:459–473, 2014
25. Qu, W.; Zhang, X.; and Haiqun Huang, H., “Flexural Behavior of Concrete Beams Reinforced with Hybrid GFRP and Steel Bars, *Journal of Composites for Construction*, Vol. 13, No. 5, October 1, 2009. 13:350-359.
26. Dupont D. “Modelling and experimental validation of the constitutive law (σ - ϵ) and cracking behavior of steel fiber reinforced concrete” Ph.D. Dissertation, Catholic University of Leuven, Belgium, 2003.
27. Levy, M., “Memoire sur la theorie des plaques elastiques planes”, *J Math Pures Appl*, vol.1899.
28. Boresi, Arthur Peter, Richard Joseph Schmidt, and Omar M. Sidebottom. *Advanced mechanics of materials*. Vol. 6. New York: Wiley, 1993.
29. Quintas V., “Two main methods for yield line analysis of slabs”, *Journal of engineering mech*, 2003
30. Kennedy G., Goodchild C., “Practical yield line design”, *Reinforced concrete council*, 2003.
31. Aswani, Karan. *Design procedures for Strain Hardening Cement Composites (SHCC) and measurement of their shear properties by mechanical and 2-D Digital Image Correlation (DIC) method*. Diss. Arizona State University, 2014.
32. Scott M.H., Fenves G.L., “Plastic Hinge Integration Methods for Force-Based Beam–Column Elements”, *Structural engineering*, Volume 132, Issue 2, pg. 244-252, 2006.
33. Kheyroddin A., Naderpour H., “Plastic hinge rotation capacity of reinforced concrete beams”, *International Journal of Civil Engineerng*. Vol. 5, No. 1, 2007.
34. Haskett M., Oehlers D.J., “Rigid body moment–rotation mechanism for reinforced concrete beam hinges”, *Engineering structures*, Vol. 31, issue 5 pg 1032-1041, May 2009.
35. Baker A., “Ultimate load theory applied to the design of reinforced and prestressed concrete frames”, London: Concrete Publications Ltd., . p. 91, 1956.
36. Sawyer H., “Design of concrete frames for two failure states”, *Proceedings of the international symposium on the flexural mechanics of reinforced concrete*, ASCE-ACI, p. 405-31, 1964.

37. Corley G., "Rotation capacity of reinforced concrete beams", J Struct Eng, ASCE, 92(ST10), 121-146, 1966.
38. Mattock A., "Discussion of rotational capacity of reinforced concrete beams", J Struct Div ASCE , 93(2) 519-522, 1967.
39. ASTM. ASTM C1550-12 Standard test method for flexural toughness of fiber reinforced concrete (using centrally loaded round panel). 2012.
40. Kim, Jihwan, et al. "Investigating the flexural resistance of fiber reinforced cementitious composites under biaxial condition." Composite Structures 122 (2015): 198-208.
41. Xu, Hanfeng, Sidney Mindess, and Ivan Joseph Duca. "Performance of plain and fiber reinforced concrete panels subjected to low velocity impact loading." Proceedings of RILEM conference on fiber reinforced concrete, BEFIB, Varenna, Italy. 2004.
42. Khaloo A.R., Afshari M., "Flexural behavior of small steel fiber reinforced concrete slabs", Cement and concrete composites 27, pg 141-149, 2005.
43. de Montaignac, Renaud, et al. "Design of SFRC structural elements: post-cracking tensile strength measurement." Materials and structures 45.4 (2012): 609-622.